Inelastic Transport In Molecular Junctions From First Principles

by

Sejoong Kim

B.S. Physics

Pohang University of Science and Technology (2006)

Submitted to the Department of Physics
in partial fulfillment of the requirements for the degree of

Doctor of Philosophy in Physics

at the

MASSACHUSETTS INSTITUTE OF TECHNOLOGY

November 2011

Author .....
Department of Physics
November 28, 2011

Certified by .....
Nicola Marzari
Professor of Theory and Simulation of Materials
École Polytechnique Fédérale de Lausanne, Switzerland
Thesis Supervisor

Certified by .....
John D. Joannopoulos
Francis Wright Davis Professor of Physics
Thesis Supervisor

Accepted by .....
Krishna Rajagopal
Professor of Physics
Associate Department Head for Education

Inelastic Transport In Molecular Junctions From First Principles

by

Sejoong Kim

Submitted to the Department of Physics
on November 28, 2011, in partial fulfillment of the
requirements for the degree of
Doctor of Philosophy in Physics

Abstract

This work is dedicated to development of a first-principle approach to study electron-vibration interactions on quantum transport properties. In the first part we discuss a general implementation for inelastic transport calculations based on maximally localized Wannier functions and non-equilibrium Green's functions. Our approach is designed to determine inelastic transport properties such as differential conductances, inelastic tunneling spectroscopies and nonequilibrium vibrational populations. Our approach is first applied to benzene molecular junctions connected to cumulene and carbon nanotube electrodes. In these examples, we discuss the role of the multi-channel effect and of parity selectrion rules on the polarity of conductance steps, and the appearance of a non-monotonic behavior in the vibrational population. In the second part, we extend our formalism to study the effect of the electron-vibration interactions on the local current distribution. Using non-equilibrium Green's functions, we derive an expression for the local distribution of the inelastic current. Applying this to the benzene-cumulene junction, we show that the electron-vibration interaction can lead to a locally inverted current direction and the formation of loop currents. In the third part, we present a comprehensive study of the elastic and inelastic transport properties of carbon nanotube-zigzag graphene nanoribbon junctions, as realized in recent experiments, focusing on the local current distribution over the junctions. We calculate the local distribution of the elastic current to visualize the current injection pattern from the CNT electrodes to the ZGNRs and the current path inside the ZGNRs. For inelastic transport properties, we find a similarity in the IETS peaks and the corresponding vibrational configurations for the CNT/ZGNR/CNT junctions with different widths. As observed in the benzene-cumulene junction, we find that the inelastic current emerges from a complex network that includes loop currents. Our method and implementation can be generalized to other types of interactions, and is not limited to the electron-vibration interactions. Thus our work will be a starting point to understand the role of different and diverse interaction effects on quantum transport, using realistic predictive first-principle calculations.

Thesis Supervisor: Nicola Marzari
Title: Professor of Theory and Simulation of Materials
École Polytechnique Fédérale de Lausanne, Switzerland

Thesis Supervisor: John D. Joannopoulos
Title: Francis Wright Davis Professor of Physics

Acknowledgments

I would like to express my gratitude to my advisor, Nicola Marzari, for giving me a chance to study an exciting research topic with which I could keep studying quantum transport theory and learn first-principle calculations. I am deeply thankful to him for keeping patience with my progress, cheering up me, and giving me a lot of confidence all the time.

I am privileged to invite Prof. John Joannopoulos, Prof. Patrick Lee and Prof. Pablo Jarillo-Herrero to my thesis committee. First, I would like to thank Prof. John Joannopoulos for being my co-advisor and giving his valuable suggestions. Whenever I met him, I was always impressed with his intuition and insight. I am also indebted to Prof. Patrick Lee for his excellent lectures on condensed matter physics. Most of my understanding and knowledge in the condensed matter physics has been acquired through his lectures. In particular, his lecture on quantum coherent phenomena, such as strong and weak localizations, stimulated my interest in mesoscopic physics and quantum transport theory. I am deeply grateful to Prof. Pablo Jarillo-Herrero for informing me of recent experimental results relevant to my research.

I would like to thank all of my group members. In particular, Dr. Nicola Bonini, Dr. Davide Ceresoli, and Dr. Cheol-Hwan Park have shared their invaluable time to discuss first-principle calculations and electron-phonon interactions. I am also grateful to Dr. Nicolas Poilvert, Dr. Young-Su Lee, and Dr. Elise Li for helping me do first-principle quantum transport calculations. I have enjoyed great time with very good officemates, Dr. Nicéphore Bonnet and Dr. Dmitri Volja. I would also like to thank Dr. Xiaofeng Qian, Dr. Jivtesh Garg, Dr. Boris Kozinsky, Dr. Nicholas Singh-Miller, Dr. Oliviero Andreussi, and Kathryn Simons for their support.

I would like to express my gratitude to all Korean Physics graduate students including Dr. Taehyun Kim, Dr. Seungeun Oh, Dr. Gyo-Boong Jo, Yeryoung Lee (with Kyeong-Jae Lee), Dong-Hyun Kim, Daniel S. Park, Sungho Yoon, Yongsun Kim, Seung-Ki Kwak, Jae-Hoon Lee, Jeewoo Park, Changmin Lee, and Paul Junghyun Lee. I always enjoyed spending time with them, talking about various topics of

physics and many other interesting issues. In particular, I would like to express my special thanks to Dr. Taehyun Kim and Seung-Ki Kwak for their warm cares in my hard time.

I am indebted to POSTECH alumni in MIT/Harvard including, but not limited to, Prof. Sunghwan Jung, Dr. Kwonmoo Lee, Dr. Eunseong Lee, Dr. Jeon-Woong Kang, Dr. Byungsub Kim, Dr. Hyunjung Yi, Dr. Kyung-Sun Son, Sue-Kyung Suh, Seung-Yong Park, Dong-Hoon Lee, Dong-Hoon Kim, and Grace Han. It is a privilege to organize POSTECH alumni gatherings for four years, which gave me many chances to become close to them. They always supported me and did not hesitate to share their time to help and advise me in my hard time.

I am also thankful to all of my Korean friends in Korea and the United States: Dr. Jong-Hoon Ahn, Seokchang Ryu, Dr. Choongik Kim, Joon-Hyuk Imm, Yongho Lee, Dong-Hyun Kim, Seong-Wook Choi, Jae-Woo Chung, Seung-Min Han, Jungho Jo, Haksun Kim, Jongmin Kim, Byung-Keun Na, and many other friends that I do not mention here. They are always willing to listen to me and help me go through my hardship.

I would like to show my gratitude to all of my former group members in POSTECH. First of all, I am deeply indebted to Prof. Hyun-Woo Lee. He is one of the greatest physicists that I respect most, and my role model of a physicist. He first introduced mesoscopic physics, which is still my academic interest, to me. It is a honor of my life to work with him on fantastic topics. I will never forget an ecstatic moment that we worked on correlation-induced resonances. Without his heartful help and advice, I would not complete my Ph.D. in MIT. I also thank the other members including Dr. Soon-Wook Jung, Dr. Jae-Seung Jeong, Dr. Hyowon Park, Jae-Ho Han, Soo-Yong Lee and Myung-Joong Hwang.

Last, but most importantly, I am very deeply thankful to my family. With their endless love and supports, I have studied here and finished my Ph.D. without having any worry. It is sad that I cannot personally tell to my maternal grandfather that I finally get MIT Ph.D. degree, but I am so sure that he is also happy with me in Heaven.

Contents

List of Figures

List of Tables

Chapter 1

Introduction

1.1 Molecular Electronics

Semiconductor-based electronics manufacturers have been competing in order to produce smaller and faster devices, especially increasing the number of transistors on integrated circuits. Gordon Moore, the co-founder of Intel predicted that the number of transistors placed on an integrated circuit would double approximately every two years. This *Moore's law* has well described the history of computing electronic devices for the past forty years. However, optical lithography used in manufacturing is approaching its physical limits.

Molecular electronics, which is truly rooted at the nanometer scale, is one of the candidates that can possibly replace current silicon-based electronics. The idea that a single molecule could be used as an electronic device was theoretically proposed by Aviram and Ratner in 1974 [3]. They suggested the concept of a molecular rectifier that can act as a diode. However, their pioneering idea was not readily realized in experiments due to the limitations at this time in fabrication and measurement.

In the late twentieth century the first conductance measurement on a single molecule appeared, and it stimulated scientists and device engineers to study molecular electronics. In 1997 Reed *et al.* measured conductance through a molecular junction of gold-sulfur-aryl-sulfur-gold using a mechanically controllable break junction (MCBJ) technique [80]. They also found a molecular junction that showed neg-

ative differential resistance (NDR) [14]. For the last decade experimental techniques have been advanced and many groups have been conducting experiments on single molecular junctions intensively. Together with experimental achievements, physicists, chemists, and device engineers have studied physical and chemical properties of single molecular devices, and have designed new devices based on novel effects of quantum mechanics. However, there are still many issues to be solved for the real molecular devices from the organization and interconnection of single molecular transistors, to room-temperature functionality, to long-term stability.

1.2 Inelastic Transport in Molecular Junctions

Electron-vibration interaction in molecular junctions is one of the most important issues that should be investigated, since conduction electrons can transfer part of their energy into local molecular vibrations. Due to this *inelastic* effect, the configuration of the molecular junctions may change, and it can lead to malfunctions. In the worst case the molecular junctions can even break down. In general, since the current can be changed due to inelastic scattering with local vibrations, the operation and performance of the molecular electronic device can be significantly affected.

The main feature of an inelastic effect appears as a change in current, or equivalently a differential conductance at a threshold bias voltage which corresponds to the molecular vibrational energy. In order to understand this feature qualitatively let us consider a two-terminal geometry where the chemical potential of the left electrode μ_L is larger than that of the right electrode μ_R. When the electron is injected from the left electrode with energy ε, the electron may lose its energy ,or not, depending on this scattering that it experiences in the molecular junction. While elastically scattered electrons will maintain their original energy ε, electrons emitting (absorbing) molecular vibrations $\hbar\omega$ will have a final energy $\varepsilon - \hbar\omega$ ($\varepsilon + \hbar\omega$). In order that the injected electrons can reach the right electrode, the right lead should have empty states whose energy is the same as the final energy of these conducting electrons. This is due to the *Pauli exclusion principle*: Let us focus on a vibrational emission

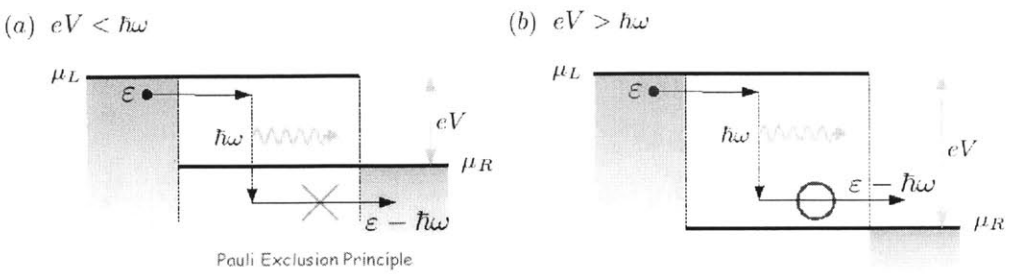

Figure 1-1: Schematic explanation for the opening of inelastic conducting channels. (a) When the applied bias eV is smaller than the vibrational energy $\hbar\omega$, the Pauli blocking effect prevents incident electrons from moving to the right electrode by emitting vibrational quanta. (b) When $eV \geq \hbar\omega$, the inelastic transport channel starts to open.

process, which is dominant at a low temperature which is the case of typical experimental condition. When the bias voltage $eV = \mu_L - \mu_R$ is smaller than a molecular vibrational energy $\hbar\omega$, there is no incoming electron that can find an empty state in the right electrde to be occupied after emitting a vibrational quantum. Thus for $eV < \hbar\omega$, the current is purely elastic. In contrast, when the bias exceeds the vibrational energy, the inelastically scattered electrons start to contribute to current. This opening of *inelastic* conducting channels leads to a change in differential conductance. The threshold bias voltage for opening the inelastic transport channels is equal to the molecular vibrational quantum energy $\hbar\omega$.

1.2.1 Experiments on inelastic transport

The inelastic transport signal explained above was first measured using a scanning tunneling microscope (STM) in 1998. Stipe *et al.* measured the current through an isolated acetylene absorbed on a copper (100) surface by changing the bias voltage [91]. They observed a small increase in the differential conductance at a bias voltage of 358 mV. They identified this threshold as that of the C-H stretching mode of the acetylene molecule. In order to verify that this conductance increase came truly from inelastic scattering with the C-H stretching mode, they substituted the hydrogen atom with a deuterium. The isotope substitution led to a shift in the threshold bias

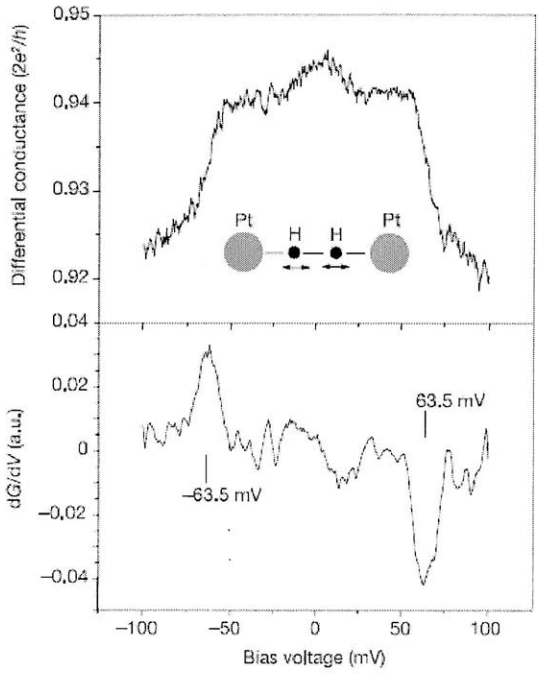

Figure 1-2: Conductance measurement of a single hydrogen molecule between platinum electrodes. (From Ref.[87]) A differential conductance drop symmetric with respect to bias polarity is observed.

voltage at which the inelastic transport signal was observed.

Vibration-induced conductance change was also observed in a two terminal geometry where a single molecule is directly connected to a source and a drain. In 2002 Smit *et al.* attached a single hydrogen molecule between platinum electrodes formed by mechanically controllable break junctions (MCBJ) [87]. They found a single pronounced resonance at 63.5 mV in the differential conductance and its derivative, symmetrically for both plus and minus bias voltages. They also repeated the same measurement using the isotopes HD and D_2. The resonance peaks observed in the experiments were scaled by the square root of the mass ratio between the hydrogen molecule and its isotopes. They argued that the longitudinal center of mass motion led to the drop in the differential conductance. Later, in combination with density-functional theory calculations, they re-interpreted the conductance drop as the transverse motion of the hydrogen molecule [25].

Inelastic transport signals were also reported for more complex organic molecules such as alkanedithiol, benzenedithiol, phenylene ethynylene and phenylene vinylene [54, 99, 35, 89, 36]. These experimental results show that one can use inelastic conductance measurement as vibrational spectroscopies. As discussed above, since the threshold bias voltages for differential conductance changes correspond to molecular vibrational energies, one can obtain a molecular vibrational spectrum by performing inelastic current measurements. Specific molecular vibrations or typical chemical bonding vibrations are known from other types of spectroscopies; for example, IR, Raman, and high resolution electron energy loss (HREEL) spectroscopies. Comparing with these data, one can assign molecular vibration configurations to the observed vibrational spectrum. Inelastic conductance measurement also provides a chance to identify molecular vibrations that are not detected in other spectroscopies.Spectroscopy based on electron-vibration interactions is called the inelastic electron tunneling spectroscopy (IETS).

1.2.2 Inelastic transport theory

In order to understand and analyze these experimental results a development in atomistic and quantitative theories is needed. Vibration-induced inelastic transport has been investigated theoretically following two main directions. The first one is to use a simple model Hamiltonian, e.g. a single electronic level coupled to a single phonon mode, which is known as the Anderson-Holstein model. Including a charging effect called Coulomb-blockade, this led to many novel and interesting transport properties that have been predicted and investigated extensively [50, 49, 51, 19, 28]. However, the model used in this approach is too simplified to give us a detailed and accurate theoretic picture that can be used to verify experimental data. Only a quantitative computational approach, e.g. based on density-functional theory (DFT), can offer a chance to describe a real system accurately without any adjustable parameters. For example, one can calculate vibrational spectra by changing molecular configurations, especially attachment geometries to electrodes, and one could infer the configuration appearing in the real experiment.

However DFT itself cannot be used straightforwardly to determine inelastic transport properties, although it can be used to provide accurate system parameters, such as electronic Hamiltonians, vibrational spectra, and normal mode configurations to transport theories. For this purpose several theoretical approaches have been proposed. For example Chen *et al.* studied inelastic effects in atomic wires and simple organic molecules based on a Fermi-golden-rule expression basedon DFT scattering states [15, 16, 17]. Similarly Jiang *et al.* proposed a golden-rule-type method based on a quantum chemical approach [40]. The non-equilibrium Green's Function (NEGF) method in combination with DFT, which is commonly called DFT-NEGF, has been the most widely used in *ab-initio* quantum transport problems. This approach is more powerful than other methods in that it can be applied not just to electron-vibration interactions, but also to other types of interactions. DFT-NEGF has been successfully applied to elastic quantum transport for both zero-bias and finite-bias cases [93, 8], and recently it has been extended to include interaction effects like electron-vibration interactions [72, 27].

DFT-NEGF requires to use an atomic-like localized basis because in the method a system should be spatially divided into two electrodes and a molecular conductor. For this reason most of DFT-NEGF packages have been implemented using a localized basis set. However, from a computational viewpoint, it is known that a planewave-based DFT calculation can provide more accurate descriptions in comparison with a localized basis. Furthermore, while basis functions used in the localized-basis calculation are determined depending on types of atoms and their configurations of the system, a planewave basis can describe a given system without making any further assumption. This is particularly relevant in low dimensional systems, where states can be spatially extended in vacuum where there is no localized basis set to describe them.

However, a planewave basis, which is uniform over space, is not suitable to DFT-NEGF calculations. *Maximally localized Wannier functions*(MLWF), first proposed by Marzari and Vanderbilt [64], provide a mathematical and numerical formulation for a unitary transformaton between an delocalized Bloch states and localized states.

Since the Wannier transformation is an exact unitary mapping, one can construct a minimal set of atomic-like localized functions within an energy window of interest without losing the accuray of the full planewave-based DFT calculation. The MLWF approach to quantum transport has been very successfully applied to zero-bias quantum conductance calculations [57, 56, 2]. The next step to develop the MLWF approach to quantum transport is to include interaction effects on transport properties. In this thesis we focus on extending the MLWF-based *ab initio* quantum transport approach in order to investigate electron-vibration interaction effects on molecular junctions.

1.3 Outline

This thesis is organized as follows. In Chapter 2 we first review the basic theory on first-principles calculations that covers density-functional theory, density-functional perturbation theory, and maximaly localized Wannier functions. In Chapter 3 non-equilibrium statistical field theory, which is called the Keldysh formalism, is introduced. Starting from the definition of the non-equilibrium Green's functions (NEGF), the perturbative expansion of NEGFs and quantum kinetic equations to determine NEGFs are discussed. In Chapter 4 we apply the Keldysh formalism to our main problem, the electron-vibration interaction on molecular junctions. In particular we discuss how to calculate two types of self-energies by using Feynman diagram rules: the electrode self-energy and the electron-vibration self-energy. In Chapter 5 the Meir-Wingreen transport formalism, a general transport theory that can include interaction effects, is first explained. We also discuss how to calculate non-equilibrium vibration populations excited by conducting electrons. Chapter 6 contains a practical implementation based on the theories reviewed in the previous chapters. In Chapter 7 we demonstrate our implementation and benchmark calculation results. In Chapter 8 we extend the non-equilibrium Green's function method to derive a local current distribution with the electron-vibration interaction inside a molecular conductor. By revisiting examples in Chapter 7, we discuss how the electron-vibration interaction

can change local-current patterns. The method developed is comprehensively used in Chapter 9 to study transport properties of carbon nanotube - zigzag graphene nanorribon junctions, which have been recently made [42, 41].

Chapter 2

Electronic Structure Methods

A condensed matter system consisting of interacting electrons and nuclei is governed by the Schrödinger equation

$$\mathcal{H}\Psi = (\mathcal{H}_e + \mathcal{H}_n + \mathcal{H}_{ne})\,\Psi = \mathcal{E}\Psi, \tag{2.1}$$

where $\mathcal{H}_e$, $\mathcal{H}_n$, and $\mathcal{H}_{ne}$ are the electron, nucleus, electron-nucleus Hamiltonians, respectively. They are defined as

$$\mathcal{H}_e = T_e + V_e = -\sum_{i=1}^{N_e} \frac{\hbar^2}{2m_e}\nabla^2 + \sum_{i<j}^{N_e} \frac{e^2}{|\mathbf{r}_i - \mathbf{r}_j|} \tag{2.2}$$

$$\mathcal{H}_n = T_n + V_n = -\sum_{I=1}^{N_n} \frac{\hbar^2}{2M_I}\nabla^2 + \sum_{I<J}^{N_n} \frac{Z_I Z_J e^2}{|\mathbf{R}_I - \mathbf{R}_J|} \tag{2.3}$$

$$\mathcal{H}_{ne} = V_{ne} = -\sum_{i}^{N_e}\sum_{I}^{N_n} \frac{Z_I e^2}{|\mathbf{R}_I - \mathbf{r}_i|}, \tag{2.4}$$

where m_e, M_I, and Z_I are the electron mass, the nucleus mass, and the nucleus charge respectively. The equation, which is written in a few lines, seems to be simple. However, solving the Schrödinger equation for the many-body system turns out to be an extremely difficult task as the number of electrons and nuclei increase. Thus one needs to use clever approximations to solve Eq.(2.1) efficiently and accurately.

2.1 Born-Oppenheimer Approximation

The first approximation is based on the fact that the nuclear motion is much slower than the electronic one due to their large mass difference. Regarding the nuclei to be fixed at $\{\mathbf{R}\}$ in the time scale of the fast electronic motion, the instantaneous Hamiltonian that the electrons *feel* is

$$\mathcal{H}_{BO}(\mathbf{R}) = T_e + V_e + V_n + V_{ne} \tag{2.5}$$

$$= -\sum_{i=1}^{N_e} \frac{\hbar^2}{2m_e}\nabla^2 + \sum_{i<j}^{N_e} \frac{e^2}{|\mathbf{r}_i - \mathbf{r}_j|} + \sum_{I<J}^{N_n} \frac{Z_I Z_J e^2}{|\mathbf{R}_I - \mathbf{R}_J|} - \sum_{i}^{N_e}\sum_{I}^{N_n} \frac{Z_I e^2}{|\mathbf{R}_I - \mathbf{r}_i|}, \tag{2.6}$$

where the nuclear configuration $\{\mathbf{R}\}$ comes in as a parametric form. By solving the time-independent Schrödinger equation,

$$\mathcal{H}_{BO}(\mathbf{R})\psi_i(\mathbf{r};\mathbf{R}) = \varepsilon_i(\mathbf{R})\psi_i(\mathbf{r};\mathbf{R}), \tag{2.7}$$

one can have a complete set of eigenstates $\{\psi_i(\mathbf{r};\mathbf{R})\}$ that depends parametrically on the nuclear configuration $\mathbf{R}$. The corresponding eigenvalues $\{\varepsilon_i(\mathbf{R})\}$ are called *adiabatic energy surfaces*. The wavefunction for the coupled system $\mathcal{H}$ can be expanded as a linear combination of $\{\psi_i(\mathbf{r};\mathbf{R})\}$,

$$\Psi(\mathbf{r},\mathbf{R}) = \sum_i \chi_i(\mathbf{R})\psi_i(\mathbf{r};\mathbf{R}). \tag{2.8}$$

Let us insert this expansion into Eq.(2.1), multiply by $\psi_j^*(\mathbf{r};\mathbf{R})$ on the left, and integrate out the electronic states. Then one finds that

$$\left[T_n + \varepsilon_i(\mathbf{R}) - \mathcal{E}\right]\chi_i(\mathbf{R}) = -\sum_j C_{ij}(\mathbf{R})\chi_j(\mathbf{R}), \tag{2.9}$$

where

$$C_{ij}(\mathbf{R}) = \sum_I \frac{1}{M_I}\langle\psi_i(\mathbf{r};\mathbf{R})|\nabla_I|\psi_j(\mathbf{r};\mathbf{R})\rangle\nabla_I + \sum_I \frac{1}{2M_I}\langle\psi_i(\mathbf{r};\mathbf{R})|\nabla_I^2|\psi_j(\mathbf{r};\mathbf{R})\rangle. \quad (2.10)$$

When the off-diagonal term $c_{i\neq j}(\mathbf{R})$ is ignored, Eq.(2.9) becomes a set of uncoupled equations,

$$[T_n + \varepsilon_i(\mathbf{R}) + C_{ii} - \mathcal{E}]\,\chi_i(\mathbf{R}) = 0. \quad (2.11)$$

Physically this approximation implies that the electrons in the electronic state $\psi_i(\mathbf{r};\mathbf{R})$ adiabatically evolve and remain in the same state $\psi_i(\mathbf{r};\mathbf{R})$ as the nuclei slowly move. Thus the total wavefunction is given by

$$\Psi(\mathbf{r},\mathbf{R}) = \chi_i(\mathbf{R})\psi_i(\mathbf{r};\mathbf{R}). \quad (2.12)$$

This is called the *Born-Oppenheimer* approximation [6]. The Born-Oppenheimer approximation is valid when the adiabatic energy surfaces are well separated.

Using the adiabatic principle, one can decouple the equations for electronic states and nuclear states. However this approximation still requires to solve the many-body electronic system. since one still has Eq.(2.5), which includes the Coulomb interaction between electrons.

2.2 Density-Functional Theory

2.2.1 Hohenberg-Kohn Theorems

A key alternative idea to address the many-body equation was suggested by Hohenberg and Kohn in 1964 [37]. Their simple but powerful theorem shows that charge density alone can be a crucial quantity to address the many-body problem.

The first Hohenberg-Kohn theorem shows that there is a one-to-one correspondence between an external potential $V_{ext}(\mathbf{r})$ and the ground state charge density $n(\mathbf{r})$. One can immediately understand that the external potential $V_{ext}(\mathbf{r})$ determines the

ground state charge density $n(\mathbf{r})$. That is simply because one can calculate the ground state charge density by solving the Hamiltonian fixed by $V_{ext}(\mathbf{r})$. Hohenberg and Kohn proved that the inverse statement also holds true, i.e. the ground state charge density $n(\mathbf{r})$ uniquely determines the external potential $V_{ext}(\mathbf{r})$. In other words, the external potential $V_{ext}(\mathbf{r})$ is a unique functional of the ground state charge density $n(\mathbf{r})$. Furthermore, once the external potential is determined, then the ground state wave function Ψ is also in principle obtained. Hence one can conclude that the ground state wavefunction Ψ is also a unique functional of $n(\mathbf{r})$.

The second Hohenberg-Kohn theorem enables to define the total energy functional $E[n(\mathbf{r})]$ and use the variational principle to determine the total energy and the corresponding charge density $n(\mathbf{r})$. Based on the fact that the ground state wavefunction Ψ is a unique functional of $n(\mathbf{r})$, as discussed in the first theorem, one can define a universal functional $F[n]$ of $n(\mathbf{r})$,

$$F[n] \equiv \langle \Psi[n] | T_e + V_e | \Psi[n] \rangle, \tag{2.13}$$

where T_e and V_e are kinetic energy and the electron-electron interaction energy operators respectively. It is obvious that $F[n]$ is independent of the external potential $V_{ext}(\mathbf{r})$. For a given external potential $V_{ext}(\mathbf{r})$, the total energy functional is written as

$$E[n] = F[n] + \int n(\mathbf{r}) V_{ext}(\mathbf{r}) d\mathbf{r}. \tag{2.14}$$

This total energy functional has a minimum E_0 for the ground charge density $n(\mathbf{r})$. For any other charge density $n'(\mathbf{r})$,

$$E_0 = E[n] \leq E[n']. \tag{2.15}$$

Therefore ground state properties such as the ground state energy E_0 and the ground state charge density $n(\mathbf{r})$ can be obtained by applying the variational principle to the total energy functional $E[n]$. The Hohenberg-Kohn theorem provides a conceptual foundation to simplify the problem of solving the many-body Schrödinger equation

to one of searching the 3-dimensional charge density to minimize the total energy functional. However since the explicit form of the univerisal functional $F[n]$ for the interacting system is unknown, the Hohenberg-Kohn theorem cannot give us a practical way to solve the many-body system.

2.2.2 Kohn-Sham Equations

For a practical solution, Kohn and Sham proposed to use an auxiliary non-interacting electron system with an effective potential, instead of dealing with the true interacting electron system, where the universal functional $F[n]$ is not known [52]. Their mapping assumes that the ground state charge density of the original interacting system can be represented by the auxiliary non-interacting system. The auxiliary non-interacting system is described by a single-particle Schrödinger-like equation known as the Kohn-Sham equation,

$$\mathcal{H}_{KS}\psi_i = \left[-\frac{\hbar^2}{2m}\nabla^2 + v_{KS}\right]\psi_i = \varepsilon_i\psi_i, \tag{2.16}$$

where v_{KS} is an effective Kohn-Sham potential. The ground state wavefunction Ψ for this non-interacting system is expressed by the Slater determinant,

$$\Psi = \frac{1}{\sqrt{N!}}\det\left[\psi_1, \ldots, \psi_N\right] \tag{2.17}$$

and its ground state charge density is

$$n(\mathbf{r}) = \sum_{i=1}^{N} |\psi_i(\mathbf{r})|^2. \tag{2.18}$$

Here $\{\psi_i\}$ are the N lowest eigenstates of the Kohn-Sham equations.

In this single particle picture, the universal functional $F[n]$ is decomposed as

$$F[n] = T_0[n] + E_H[n] + E_{xc}[n], \tag{2.19}$$

where $T_0[n]$ is the kinetic energy for the non-interacting system,

$$T_0[n] = T_0\left[\{\psi_i\}\right] = -\sum_i \frac{\hbar^2}{2m}\langle\psi_i|\nabla^2|\psi_i\rangle, \tag{2.20}$$

and $E_H[n]$ is the Hartree interaction energy,

$$E_H[n] = \frac{e^2}{2}\int \frac{n(\mathbf{r})n(\mathbf{r}')}{|\mathbf{r}-\mathbf{r}'|}d\mathbf{r}d\mathbf{r}'. \tag{2.21}$$

$E_{xc}[n]$, which is called an*exchange-correlation* functional, contains the remaining unknown contributions. From the original definition of the universal function $F[n]$, the exchange-correlation functional can be re-written as

$$E_{xc}[n] = \left(\langle\Psi|T_e|\Psi\rangle - T_0[n]\right) + \left(\langle\Psi|V_e|\Psi\rangle - E_H[n]\right). \tag{2.22}$$

As seen above, the exchange-correlation functional contains the difference between the true kinetic energy and the auxiliary non-interacting kinetic energy, and the difference between the original full many-body interaction energy and the classical Hartree interaction energy.

Applying the variational principle to the total energy functional, the effective Kohn-Sham potential $v_{KS}(\mathbf{r})$ can be obtained

$$v_{KS} \equiv V_{ext}(\mathbf{r}) + v_H(\mathbf{r}) + v_{xc}(\mathbf{r}) = V_{ext}(\mathbf{r}) + \int \frac{n(\mathbf{r}')}{|\mathbf{r}-\mathbf{r}'|}d\mathbf{r}' + \frac{\delta E_{xc}[n]}{\delta n}. \tag{2.23}$$

Note that the Kohn-Sham potential depends on the charge density $n(\mathbf{r})$. It implies that the Kohn-Sham equation should be solved self-consistently.

The exact exchange-correlation functional is still unknown. However, once one can make a reasonably good approximation on the exchange-correlation functional that is much smaller than the entire density-functional, the Kohn-sham approach provides us with a practical and often accurate way to solve the many-body Schrödinger equation.

2.2.3 Exchange-Correlation Functionals

The crucial part for any practical DFT calculation is to find a physically reasonable and accurate approximation of the exchange-correlation functional. A simple but widely used exchange-correlation functional is the *local-density approximation* (LDA) [52]. In LDA, it is assumed that the exchange-correlation energy in a small volume $d\mathbf{r}$ located at $\mathbf{r}$ can be replaced by that of the homogeneous electron gas with the same charge density $n(\mathbf{r})$:

$$E_{xc}^{LDA}[n] = \int n(\mathbf{r})\varepsilon_{xc}[n(\mathbf{r})]d\mathbf{r}, \tag{2.24}$$

where $\varepsilon_{xc}[n(\mathbf{r})]$ is the exchange-correlation energy density per electron of the homogeneous electron gas at the charge density $n(\mathbf{r})$, a scalar quantity that was determined by Ceperley and Alder using accurate quantum Monte Carlo calculations [13]. Thus the LDA exchange-correlation potential is readily given by

$$v_{xc}^{LDA} = \frac{\delta E_{xc}^{LDA}[n]}{\delta n} = \varepsilon_{xc}[n(\mathbf{r})] + n(\mathbf{r})\frac{d\varepsilon_{xc}[n(\mathbf{r})]}{dn}. \tag{2.25}$$

The LDA functional, which is accurate for a slowly varying charge density, has been successfully applied to a variety of materials, especially weakly correlated materials. It accurately describes structural and vibrational properties, even if it overestimates the crystal cohesive and molecular binding energies, due to a comparatively poorer description of atomic energies [4].

The LDA exchange-correlation functional can be improved by including the gradient of the charge density $\nabla n(\mathbf{r})$,

$$E_{xc}^{GGA} = \int n(\mathbf{r})\varepsilon_{xc}[n(\mathbf{r}), \nabla n(\mathbf{r})]d\mathbf{r}, \tag{2.26}$$

This approximation is called the *genearlized gradient approximation* (GGA) [74]. The GGA functional can generally provide a better description than LDA.

2.2.4 Planewave Basis Calculation

For periodic bulk solids which contain an infinite number of electrons and ions, it seems that it would be intractable to solve the Schrödinger or Kohn-Sham equation. However it turns out that using the translational symmetry of periodic systems makes the problem simpler. According to Bloch theorem, when a system has a periodic potential

$$\mathcal{H}\psi(\mathbf{r}) = \left[-\frac{\hbar^2}{2m}\nabla^2 + v(\mathbf{r})\right]\psi(\mathbf{r}), \tag{2.27}$$

where

$$v(\mathbf{r}) = v(\mathbf{r}+\mathbf{R}) \quad \text{(for all } \mathbf{R} \text{ in a Bravais lattice)}, \tag{2.28}$$

the eigenfunction ψ can be chosen to have the following form:

$$\psi_{n\mathbf{k}}(\mathbf{r}) = e^{i\mathbf{k}\cdot\mathbf{r}}u_{n\mathbf{k}}(\mathbf{r}) \tag{2.29}$$

$$u_{n\mathbf{k}}(\mathbf{r}) = u_{n\mathbf{k}}(\mathbf{r}+\mathbf{R}). \tag{2.30}$$

which is expressed as a lattice-periodic function modulated by a plane-wave envolope $e^{i\mathbf{k}\cdot\mathbf{r}}$ [73]. The crystal momentum vector $\mathbf{k}$ runs over the first Brillouin zone (BZ). Translational symmetry gives a set of decoupled Schrödinger equations for all $\mathbf{k}$ vectors in the BZ:

$$\left[-\frac{\hbar^2}{2m}(\nabla + i\mathbf{k})^2 + v(\mathbf{r})\right]u_{n\mathbf{k}}(\mathbf{r}) = \varepsilon_{n\mathbf{k}}u_{n\mathbf{k}}(\mathbf{r}), \tag{2.31}$$

where $\{\psi_{n\mathbf{k}}\}$ satisfy the orthonormality conditions $\langle\psi_{n\mathbf{k}}|\psi_{n'\mathbf{k}'}\rangle = \delta_{n,n'}\delta_{\mathbf{k},\mathbf{k}'}$. The problem of solving the Schrödinger equation for the entire system is replaced by that of solving a set of decoupled equations, which can then be solved within the primitive unit cell. When Eq.(2.31) is solved for any $\mathbf{k}$ in the BZ, the energy eigenvalues $\{\varepsilon_{n\mathbf{k}}\}$ provide the energy bands for the periodic system. Note that in this Kohn-Sham formulation these correspond to the fictitious Kohn-Sham energies, rather than the physically correct quasiparticle energies. The electron charge density, which is the

most important physical quantity in DFT, can be computed as

$$n(\mathbf{r}) = \sum_{k}^{1BZ} \sum_{n}^{occ} |u_{n\mathbf{k}}|^2, \tag{2.32}$$

where the n index is summed over the occupied bands. In principle one has to solve Eq.(2.31) for the infinite number of $\mathbf{k}$ points in BZ. However, in a practical calculation, a finite number of $\mathbf{k}$-points is used. The number of $\mathbf{k}$-points sampled in the calculation should be determined such that any physical quantity is well converged within the desired accuracy.

Practically Eq.(2.31) can be solved by expanding wavefunctions with a chosen set of basis functions. A planewave basis can be a natural choice because it is consistent with the periodic boundary conditions used in the calculations and is suitable to studying the crystalline structure of solids. The wavefunction expanded in planewaves can be written as

$$\psi_{n\mathbf{k}}(\mathbf{r}) = \sum_{\mathbf{G}}^{N_{pw}} c_{n\mathbf{k}}(\mathbf{G}) e^{i(\mathbf{k}+\mathbf{G})\cdot\mathbf{r}}, \tag{2.33}$$

where $\{\mathbf{G}\}$ are the reciprocal lattice vectors. In principle, the *exact* wavefunction is expanded in terms of an infinite number of planewaves. However, any practical calculation cannot deal with the total Hilbert space spanned by an infinite planewave basis. Instead, the expansion is taken over a finite number of $\mathbf{G}$ vectors that satisfy $\frac{\hbar^2}{2m}|\mathbf{k}+\mathbf{G}|^2 < E_{cut}$, where E_{cut} is a planewave energy *cutoff*. This truncation is reasonable since contribution from larger kinetic-energy $\mathbf{G}$ vectors becomes less and less important in expansion. The error caused by truncation of a planewave basis can be reduced by increasing the energy cutoff E_{cut}. In a planewave basis, the Kohn-Sham equations become algebraic equations in reciprocal space:

$$\sum_{\mathbf{G}'} \left[\frac{\hbar^2}{2m} |\mathbf{k}+\mathbf{G}|^2 \delta_{\mathbf{G},\mathbf{G}'} + v_{KS}(\mathbf{G}-\mathbf{G}') \right] c_n(\mathbf{k}+\mathbf{G}') = \varepsilon_{n\mathbf{k}} c_n(\mathbf{k}+\mathbf{G}). \tag{2.34}$$

A planewave basis has several advantages, especially in comparison with a localized orbital basis. The accuracy of a calculation can be improved continuously

and finely by tuning the single parameter E_{cut}. Furthermore, a planewave basis does not depend on atomic positions or system structure. Therefore it can deal with all parts of a inhomogeneous system and different atomic configurations on an equal footing, without making any further assumption. From a computational viewpoint, a planewave basis allows to use efficient algorithms like Fast Fourier Transformation between real and reciprocal space. As a minus, the number of planewaves is larger than that of localized orbitals, and so it requires larger computational resources and time that are the prices to pay for accuracy and transferability.

2.2.5 Pseudopotentials

Another major part of a practical DFT calculation is a pseduopotential that effectively replaces the true potential of the nucleus and the core electrons. If one tries to solve the eigenfunctions for all the electrons in the presence of the nuclear potential, one has to use a significant number of planewaves to describe the wavefunction near the nuclei, considering the nature of the Coulomb potential. Fortunately one does not have to solve all-electron wavefuctions because the core electrons are tightly bound to the nuclei and they do not contribute to the physical and chemical properties. The core electrons just play the role of a screening potential to the nuclei. Thus, in combination of the nuclear potential and the screening potential of the core electrons, one can construct a much *smoother* effective potential for valence electrons. This is called a *pseudopotential*. From a computational viewpoint, the pseudopotential gives us the following advantages: First, since the core electrons are treated as a screening potential and one solves the many-body Schrödinger equation only for the valence electrons, one can reduce the number of electrons for the many-body system. Second, because of its smoothness near the nuclei, the calculation requires a smaller number of planewaves. As a result a computational speed can be boosted up and a computational cost can be significantly saved.

One of the widely used approaches in pseudopotential theory is that of *norm-conserving* pseudopotentials, where valence pseudopotentials $\{|\psi_i^{PS}\rangle\}$ satisfy the orthonormal condition $\langle\psi_i^{PS}|\psi_j^{PS}\rangle = \delta_{ij}$. A norm-conserving pseudopotential is gener-

ated by following the following conditions [31]:

1. All-electron and pseudo eigenvalues agree for the chosen atomic reference configuration.

2. All-electron and pseudo atomic wavefunctions match outside a chosen cut-off core radius r_c.

3. The integrals of the charge density for each wavefunction inside r_c agree (norm-conservation).

4. The logarithmic derivatives of the all-electron and pseudo wavefunctions and their first energy derivatives agree at $r = r_c$.

However, the norm-conserving pseudopotential scheme does not reduce the cut-off of the planewaves for valence states at the beginning of an atomic shell, such as $2p$, $3d$, and $4f$ because there are no core states of the same angular momentum to screen. To solve this issue, D. Vanderbilt introduced *ultrasoft pseudopotential* by relaxing the norm-conserving condition [96]. While the all-electron and pseudo wavefunctions match outside the cut-off core radius r_c, the pseudo-wavefunction is made to be smoother by introducing an augmented charge in the core region, which is defined as

$$\Delta Q_{ij} = \int_0^{r_c} \left(d\mathbf{r}\psi_i^{AE*}(\mathbf{r})\psi_j^{AE}(\mathbf{r}) - \psi_i^{US*}(\mathbf{r})\psi_j^{US}(\mathbf{r}) \right), \tag{2.35}$$

where $\psi_i^{AE}(\mathbf{r})$ and $\psi_i^{US}(\mathbf{r})$ represent the all-electron and pseudo wavefunctions. Then the Schrödinger equation for the ultrasoft wavefunction $|\psi_n^{US}\rangle$ is formulated as a generalized eigenvalue equation,

$$\hat{H}|\psi_n^{US}\rangle = \varepsilon_n \hat{S}|\psi_n^{US}\rangle \tag{2.36}$$

with a generalized orthonormal constraint $\langle\psi_i^{US}|\hat{S}|\psi_j^{US}\rangle = \delta_{ij}$. Here $\hat{S}$ is an overlap operator defined as

$$\hat{S} = \hat{I} + \sum_{i,j,I} \Delta Q_{ij}^I |\beta_i^I\rangle\langle\beta_j^I|, \tag{2.37}$$

where I denotes the ions, i, j are angular momentum quantum numbers, and $|\beta_i^I\rangle$ is a projection function of the ion I and ith angular momentum channel.

2.3 Linear Response Theory

When the ground-state charge density is obtained from a DFT calculation, linear response properties of the system can also be calculated. This procedure is called *density-functional perturbation theory* (DFPT). The key quantity to calculate linear-response properties is the Kohn-Sham orbital variation, or equivalently the charge density variation with respect to the external perturbation, and DFPT provides a self-consistent calculation scheme to calculate the charge density variation. Here we briefly discuss the basic formalism of DFPT and of electron-phonon interactions in DFPT. For a complete discussion on DFPT see Ref. [4].

2.3.1 Density Functional Perturbation Theory

When the external potential is a differentiable function of a set of parameters $\lambda \equiv \{\lambda_i\}$, the first and second derivatives of the ground state energy can be calculated by using the Hellmann-Feynman theorem:

$$\frac{\partial E}{\partial \lambda_i} = \int \frac{\partial V_\lambda(\mathbf{r})}{\partial \lambda_i} n_\lambda(\mathbf{r}) d\mathbf{r} \tag{2.38}$$

$$\frac{\partial^2 E}{\partial \lambda_i \partial \lambda_j} = \int \frac{\partial^2 V_\lambda(\mathbf{r})}{\partial \lambda_i \partial \lambda_j} n_\lambda(\mathbf{r}) d\mathbf{r} + \int \frac{\partial V_\lambda(\mathbf{r})}{\partial \lambda_i} \frac{n_\lambda(\mathbf{r})}{\partial \lambda_j} d\mathbf{r} \tag{2.39}$$

The second derivative of the total energy with respect to the perturbation parameters $\{\lambda_i\}$ can be computed with the first order response of the charge density. The charge density variation can be linearized in terms of the Kohn-Sham orbital variation:

$$\Delta n(\mathbf{r}) = 2\mathrm{Re} \sum_{n=1}^{N} \psi_n^*(\mathbf{r}) \Delta\psi_n(\mathbf{r}). \tag{2.40}$$

Here the finite-difference operation Δ is defined as

$$\Delta f(\mathbf{r}) \equiv \sum_i \frac{\partial f}{\partial \lambda_i} \Delta\lambda_i. \tag{2.41}$$

Applying standard first-oder perturbation theory, the Kohn-Sham orbital variation $\Delta\psi_n(\mathbf{r})$ can be determined by the solution of the following equation:

$$(\mathcal{H}_{KS} - \varepsilon_n) |\Delta\psi_n\rangle = -(\Delta v_{KS} - \Delta\varepsilon_n) |\psi_n\rangle, \tag{2.42}$$

where $\mathcal{H}_{KS}$ is the unperturbed Kohn-Sham Hamiltonian (Eq.(2.16)),

$$\Delta v_{KS}(\mathbf{r}) = \Delta V(\mathbf{r}) + e^2 \int \frac{\Delta n(\mathbf{r}')}{|\mathbf{r} - \mathbf{r}'|} d\mathbf{r}' + \left.\frac{dv_{xc}(n)}{dn}\right|_{n=n(\mathbf{r})} \Delta n(\mathbf{r}) \tag{2.43}$$

is the first-order correction to the self-consistent potential and $\Delta\varepsilon_n = \langle\psi_n|\Delta V_{KS}|\psi_n\rangle$ is the first-order energy correction to the Kohn-Sham energy eigenvalue ε_n. Because the derivative of the self-consistent potential ΔV_{KS} includes the charge density variation $\Delta n(\mathbf{r})$, Eq.(2.40), (2.42), and (2.43) should be solved self-consistently.

In particular, for lattice dynamics, interatomic force constants can be computed by calculating the second-order derivative of the Born-Oppenheimer energy surface $E(\mathbf{R})$ with respect to the nuclear configuration $\mathbf{R} = \{\mathbf{R}_I\}$:

$$\frac{\partial^2 E(\mathbf{R})}{\partial \mathbf{R}_I \partial \mathbf{R}_J} = \int \frac{\partial n_{\mathbf{R}}(\mathbf{r})}{\partial \mathbf{R}_J} \frac{\partial V_{ne}(\mathbf{R}, \mathbf{r})}{\partial \mathbf{R}_I} d\mathbf{r} + \int n_{\mathbf{R}}(\mathbf{r}) \frac{\partial^2 V_{ne}(\mathbf{R}, \mathbf{r})}{\partial \mathbf{R}_I \partial \mathbf{R}_J} + \frac{\partial^2 V_n(\mathbf{R})}{\partial \mathbf{R}_I \partial \mathbf{R}_J}, \tag{2.44}$$

where

$$V_n = \sum_{I<J}^{N_n} \frac{Z_I Z_J e^2}{|\mathbf{R}_I - \mathbf{R}_J|} \tag{2.45}$$

is the electrostatic interaction energy between nuclei, and

$$V_{ne} = -\sum_i^{N_e} \sum_I^{N_n} \frac{Z_I e^2}{|\mathbf{R}_I - \mathbf{r}_i|} \tag{2.46}$$

is the electron-nucleus interaction. The vibrational frequencies ω of the nuclear system

can be calculated by solving the following eigenvalue equation:

$$\det \left| \frac{1}{\sqrt{M_I M_J}} \frac{\partial^2 E(\mathbf{R})}{\partial \mathbf{R}_I \partial \mathbf{R}_J} - \omega^2 \right| = 0, \tag{2.47}$$

where the interatomic force constant is scaled by nuclear masses.

2.3.2 Electron-Vibration Interaction

The electron-vibration interaction Hamiltonian can be written in a second-quantized form as

$$\mathcal{H}_{el-ph} = \sum_{\mathbf{k}\mathbf{q}\nu} \sum_{mn} g^{\mathbf{q}\nu,mn}_{\mathbf{k}+\mathbf{q},\mathbf{k}} c^{\dagger m}_{\mathbf{k}+\mathbf{q}} c^{n}_{\mathbf{k}} \left(b^{\dagger}_{-\mathbf{q}\nu} + b_{\mathbf{q}\nu} \right), \tag{2.48}$$

where $c^{\dagger n}_{\mathbf{k}}$ ($c^{n}_{\mathbf{k}}$) is the creation (annhilation) operator for an electron with energy $\varepsilon_{n\mathbf{k}}$. Similarly $b^{\dagger}_{\mathbf{q}\nu}$ ($b_{\mathbf{q}\nu}$) is the creation (annhilation) operator for a phonon in the vibrational mode ν with energy $\omega_{\mathbf{q}\nu}$ at wave vector $\mathbf{q}$. $g^{\mathbf{q}\nu,mn}_{\mathbf{k}+\mathbf{q},\mathbf{k}}$ is the electron-phonon coupling matrix element. Once the linear response of the charge density is computed from DFPT, the electron-phonon coupling matrix can be calculated from the derivative of the self-consistent Kohn-Sham potential Δv_{KS} as follows:

$$g^{\mathbf{q}\nu,mn}_{\mathbf{k}+\mathbf{q},\mathbf{k}} = \left(\frac{\hbar}{2\omega_{\mathbf{q}\nu}} \right)^{1/2} \langle \psi_{\mathbf{k}+\mathbf{q},m} | \Delta v^{\mathbf{q}\nu}_{KS} | \psi_{\mathbf{k},n} \rangle, \tag{2.49}$$

where $\psi_{\mathbf{k},n}$ is the nth Kohn-Sham orbital wavefunction at wavevector $\mathbf{k}$. The self-consistent Kohn-Sham potential is perturbed with respect to the phonon mode ν at wavevector $\mathbf{q}$:

$$\Delta v^{\mathbf{q}\nu}_{KS} = \sum_{I} \sum_{\alpha} \frac{\partial v_{KS}}{\partial u_{I\alpha}} X_{\mathbf{q}\nu}(I\alpha), \tag{2.50}$$

where $X_{\mathbf{q}\nu}$ is the eigenvector of the phonon normal mode ν at wavevector $\mathbf{q}$, and $u_{I\alpha}$ is the atomic displacement of the nucleus I in the α direction.

As it will be discussed in detail later, a large supercell geometry containing two electrodes and a conducting molecule is used in our quantum transport calculation. For this large supercell geometry Γ-point sampling can be safely used. In addition local vibrations of the conducting molecule are only considered. Therefore by dropping

the wavevector indices for electrons and vibrations, the electron-phonon interaction can be written in a simpler form:

$$\mathcal{H}_{el-ph} = \sum_{\nu} \sum_{mn} g_{\nu}^{mn} c_m^{\dagger} c_n \left(b_{\nu}^{\dagger} + b_{\nu} \right), \tag{2.51}$$

where

$$g_{\nu}^{mn} = \left(\frac{\hbar}{2\omega_{\nu}} \right)^{1/2} \langle \psi_m | \Delta v_{KS}^{\nu} | \psi_n \rangle. \tag{2.52}$$

2.4 Wannier Functions

As discussed before, a planewave-based DFT calculation has many advantages from technical and practical viewpoints. However, due to the spatially extended nature of a planewave basis it is not suitable to the quantum transport formalism based on Green's functions, which will be discussed later. This is because the Hamiltonian should be written in terms of a localized *atomic*-like basis in order to spatially separate the system into three parts: a left electrode, a right electrode, and a conductor. For this reason one needs a mathematical formulation to transform to a localized representation. In fact, this transformation was originally suggested by Wannier in 1937 [100]. The localized function in real-space, which is called the *Wannier* function, is generated by taking the Fourier transform of the extended Bloch functions:

$$|\omega_{n\mathbf{R}}\rangle = \frac{V}{(2\pi)^3} \int_{BZ} |\psi_{n\mathbf{k}}\rangle e^{-i\mathbf{k}\cdot\mathbf{R}} d\mathbf{k}, \tag{2.53}$$

where V is a volume of a real-space primitive cell and $\mathbf{R}$ is a Bravais lattice vector. Since this is an exact unitary transformation, Wannier functions span the same Hilbert space of Bloch functions. One of the great advantages of Wannier functions is that Wannier functions are orthonormal, i.e. $\langle \omega_{n\mathbf{R}} | \omega_{n'\mathbf{R}'} \rangle = \delta_{nn'} \delta_{\mathbf{R}\mathbf{R}'}$. A basis of localized orbitals can be directly used for the quantum transport calculation, but because of its non-orthogonality one should include an overlapping matrix between localized orbitals in the quantum transport formulation. In contrast, Wannier functions, which are orthonormal by construction, can make calculation and formulation much easier.

However Wannier functions are not uniquely defined because Bloch function can have an arbitrary phase,

$$|\psi_{n\mathbf{k}}\rangle \rightarrow e^{i\phi_{n\mathbf{k}}}|\psi_{n\mathbf{k}}\rangle, \tag{2.54}$$

without changing all physical properties. Thus in order to construct well-defined Wannier functions, some additional criterion is needed. In this work we adopt the Wannier function construction proposed by Marzari and Vanderbilt first and known as *Maximally-Localized Wannier function* (MLWF) [64]. The Wannier transformation needs to be generalized by mixing Bloch functions within an isolated group of N bands:

$$|\omega_{n\mathbf{R}}\rangle = \frac{V}{(2\pi)^3}\int_{BZ}\sum_{m}^{N} U_{mn}^{(\mathbf{k})}|\psi_{m\mathbf{k}}\rangle e^{-i\mathbf{k}\cdot\mathbf{R}}d\mathbf{k}, \tag{2.55}$$

The construction criterion of MLWF needed to determine the arbitrary $U_{mn}^{(\mathbf{k})}$ is to minimize the mean square spread of all Wannier functions, which is defined as

$$\Omega = \sum_{n}^{N}\left[\langle r^2\rangle_n - \langle\mathbf{r}\rangle_n^2\right] = \sum_{n}^{N}\left[\langle\omega_{n\mathbf{0}}|r^2|\omega_{n\mathbf{0}}\rangle - \langle\omega_{n\mathbf{0}}|\mathbf{r}|\omega_{n\mathbf{0}}\rangle^2\right]. \tag{2.56}$$

A difficulty arises in case of metallic systems where occupied and unoccupied bands are connected together. In this entangled case a simple unitary transformation between occupied bands would fail to localize meaningfully wavefunctions in real-space. Souza *et al.* proposed a method to select out a *maximally-connected* subspace that is composed of orbitals of a similar character out of the whole entangled manifold [90]. Extracting the maximally-connected subspace is achieved by minimizing the gauge-invariant part Ω_I of the spread functional Ω:

$$\Omega = \Omega_I + \tilde{\Omega}, \tag{2.57}$$

where

$$\Omega_I = \sum_{n}\left[\langle r^2\rangle_n - \sum_{\mathbf{R}m}|\langle\mathbf{R}m|\mathbf{r}|\mathbf{0}n\rangle|^2\right], \tag{2.58}$$

and

$$\tilde{\Omega} = \sum_{n} \sum_{\mathbf{R}m \neq \mathbf{0}n} |\langle \mathbf{R}m|\mathbf{r}|\mathbf{0}n\rangle|^2 . \tag{2.59}$$

The gauge-invariant part Ω_I can be written on a regular mesh of $\mathbf{k}$-points:

$$\Omega = \frac{1}{N_{kp}} \sum_{\mathbf{k},\mathbf{b}} W_b \mathrm{Tr}\left[\hat{P}_{\mathbf{k}} \hat{Q}_{\mathbf{k}+\mathbf{b}}\right], \tag{2.60}$$

where $\{\mathbf{b}\}$ is a set of vectors pointing to the neighbors of a point $\mathbf{k}$, W_b is a weighting factor for the corresponding vector $\mathbf{b}$, N_{kp} is the total number of $\mathbf{k}$-points, $\hat{P}_{\mathbf{k}} = \sum_n |u_{n\mathbf{k}}\rangle\langle u_{n\mathbf{k}}|$ and $\hat{Q}_{\mathbf{k}+\mathbf{b}} = 1 - \hat{P}_{\mathbf{k}}$. The gauge-invariant part Ω_I represents a measure of the *change of character* across the BZ, and so one can obtain a subspace composed of orbitals of similar character by minimizing it.

For the $N_{\mathbf{k}}$-dimensional original Bloch space $\{|u_{n\mathbf{k}}\rangle\}$ at a given $\mathbf{k}$ point, the procedure of minimizing Ω_I determines the N-dimensional optimally connected subspace $\{|u^{opt}_{n\mathbf{r}}\rangle\}$:

$$|u^{opt}_{n\mathbf{r}}\rangle = \sum_{m \in N_{\mathbf{k}}} U^{opt(\mathbf{k})}_{mn} |u_{n\mathbf{k}}\rangle, \tag{2.61}$$

where $U^{opt(\mathbf{k})}_{mn}$ is a rectangular $N \times N_{\mathbf{k}}$ matrix. Once the maximally connected subspace is built, then MLWF can be constructed by minimizing $\tilde{\Omega}$.

MLWFs, which are suitable to our quantum transport calculation, are nowadays widely used for many reasons:

1. MLWFs provide a clear picture of chemical bonding.

2. The centers of MLWFs, and their displacement under polarizing field have a close, formal connection to the macroscopic and microscopic polarization of an insulating system.

3. The maximal localization can be exploited by diverse methods that rely on real-space localized basis sets, such as $\mathcal{O}(N)$ methods.

For a detailed review of MLWF on implementatation and its application see Ref. [64] and [90].

Chapter 3

Keldysh Formalism

In this chapter we review a diagrammatic perturbation theory based on nonequilibrium Green's Functions (NEGFs), which is known as the Keldysh formalism. The Keldysh formalism provides a general theoretical method to describe physics under nonequilibrium. This theory is essential to our interests, in which a finite bias large enough to excite local vibrations is applied to molecular conductors. This nonequilibrium statistical field theory was originally formulated by Martin and Schwinger [62], Kadanoff and Baym [44], and Keldysh [46]. For a detailed presentation and derivation see Ref. [77] and [78], which we follow here.

3.1 Contour-ordered Green's Functions

Non-Equilibrium Green's functions are usually called contour-order Green's functions, in which two time variables are defined on a contour in a complex plane. The need to introduce the time contour can be understood by comparing a time-ordered Green's function in equilibrium theory [76]. The time-ordered Green's function $G(t,t')$ at zero temperature is

$$G(t,t') = \frac{1}{i\hbar}\left\langle \Phi \left| \mathcal{T}\psi_{\mathcal{H}}(t)\psi^{\dagger}_{\mathcal{H}}(t') \right| \Phi \right\rangle \tag{3.1}$$

where $|\Phi\rangle$ is a ground state of the system and $\mathcal{T}$ represents a time-ordering operation. The field operator $\psi_{\mathcal{H}}(t)$ is written in the Heisenberg picture with respect to the sys-

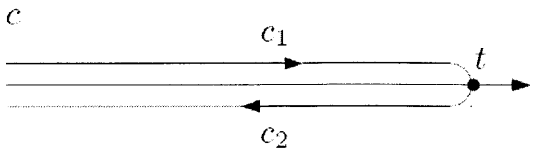

Figure 3-1: Closed time contour c on which the contour-ordered Green's function is defined. It consists of two branches: the forward time branch c_1 and the backward time branch c_2.

tem Hamiltonian $\mathcal{H} = H_0 + V$, where H_0 is the free particle (quadratic) Hamiltonian and V is the interaction Hamiltonian. Due to the interaction V we do not generally know what the ground state $|\Phi\rangle$ is. The idea to solve for $G(t, t')$ is to use what we know very well, that is, information of the noninteracting system in which $V = 0$. When the interaction V is adiabatically turned on and off, one can use the fact that the full interacting ground state $|\Phi\rangle$ can be smoothly connected to the free ground state $|\Phi_0\rangle$ at $t = \pm\infty$ via the time-evolution operator. In the interaction picture, the time-ordered Green's function $G(t, t')$ becomes

$$G(t,t') = \frac{1}{i\hbar} \frac{\left\langle \Phi_0 \left| \mathcal{T} U(\infty, -\infty)\, \psi_{H_0}(t) \psi^\dagger_{H_0}(t) \right| \Phi_0 \right\rangle}{\langle \Phi_0 | U(\infty, -\infty) | \Phi_0 \rangle}, \tag{3.2}$$

where ψ_{H_0} evolves with respect to H_0 [76]. According to the Gell-Mann-Low theorem [76], $|\Phi_0\rangle$ at $t \to -\infty$ is different from $|\Phi_0\rangle$ at $t \to \infty$ by a phase factor, which appears as the denominator $\langle \Phi_0 | U(\infty, -\infty) | \Phi_0 \rangle$. The time-evolution operator $U(\infty, -\infty)$ in the interaction picture, which is called the S-matrix, is $U(\infty, -\infty) = \mathcal{T} e^{-i\hbar \int_{-\infty}^{\infty} d\bar{t} V_{H_0}(\bar{t})}$.

However, this idea cannot be applied to a nonequilibrium situation, where a perturbation driving the system out of equilibrium should be kept turned on. A clever trick to resolve this situation is to introduce a closed time contour, which starts from $-\infty$, reaches a certain time t, and then goes back to $-\infty$. The time contour c has two branches: a forward branch c_1 from $-\infty$ to t, and a backward branch c_2 from t to $-\infty$, as shown in Fig. 3-1. Along this closed time contour we can define the

contour-ordered Green's function

$$G(\tau,\tau') = \frac{1}{i\hbar}\left\langle \mathcal{T}_c \psi_{\mathcal{H}}(\tau)\psi^{\dagger}_{\mathcal{H}}(\tau')\right\rangle . \tag{3.3}$$

Here $\mathcal{T}_c$ is the contour ordering operation, which means that the operator appearing on the contour c earlier is placed to the right,

$$G(\tau,\tau') = \begin{cases} G^{>}(\tau,\tau') = \frac{1}{i\hbar}\left\langle \psi_{\mathcal{H}}(\tau)\,\psi^{\dagger}_{\mathcal{H}}(\tau')\right\rangle & \tau >_c \tau' \\ G^{<}(\tau,\tau') = \pm\frac{1}{i\hbar}\left\langle \psi^{\dagger}_{\mathcal{H}}(\tau')\,\psi_{\mathcal{H}}(\tau)\right\rangle & \tau' >_c \tau \end{cases} \tag{3.4}$$

where the upper (lower) sign is for fermions (bosons). $G^{>}$ and $G^{<}$ are named *greater* and *lesser* Green's functions respectively. Depending on positions of τ and τ' on the contour, $G(\tau,\tau')$ can become four different Green's functions. When τ and τ' are located on the forward (backward) branch c_1, the contour ordering is the same as the time (anti-time) ordering. If τ is on $c_1(c_2)$ and τ' is on $c_2(c_1)$, τ always appears *earlier*(*later*) than τ' on the contour. Thus, for these four cases the contour-ordered Green's function $G(\tau,\tau')$ becomes

$$G(\tau,\tau') = \begin{cases} G^{t}(\tau,\tau') & \tau,\tau' \in c_1 \\ G^{<}(\tau,\tau') & \tau \in c_1, \tau' \in c_2 \\ G^{>}(\tau,\tau') & \tau \in c_2, \tau' \in c_1 \\ G^{\bar{t}}(\tau,\tau') & \tau,\tau' \in c_2 \end{cases} \tag{3.5}$$

where

$$G^{t}(\tau,\tau') = \theta(\tau-\tau')G^{>}(\tau,\tau') + \theta(\tau'-\tau)G^{<}(\tau,\tau') \tag{3.6}$$

$$G^{\bar{t}}(\tau,\tau') = \theta(\tau-\tau')G^{<}(\tau,\tau') + \theta(\tau'-\tau)G^{>}(\tau,\tau'). \tag{3.7}$$

One of the advantages of using contour-ordered Green's functions is that it can provide information on the particle density in the non-equilibrium situation. This can be obtained by taking $t' \to t$ in $G^{<}(t,t')$,

$$\langle n(t)\rangle = \langle \psi^{\dagger}_{\mathcal{H}}(t)\psi_{\mathcal{H}(t)}\rangle = -i\hbar \lim_{t'\to t} G^{<}(t,t') \tag{3.8}$$

In equilibrium the energy-resolved electron density can be obtained from the Fermi-Dirac equilibrium distribution $n_F(\varepsilon) = (e^{\beta(\varepsilon-\mu)}+1)^{-1}$ and the spectral density $A(\varepsilon)$.

$$G^<(\varepsilon) = in_F(\varepsilon)A(\varepsilon) \tag{3.9}$$

Because the spectral density can be obtained from the retarded Green's functions,

$$A(\varepsilon) = i\left[G^r(\varepsilon) - G^a(\varepsilon)\right], \tag{3.10}$$

the lesser Green's function $G^<$ does not provide new information on the system in equilibrium. In contrast, in the case of the nonequilibrium situation, which there is no universal statistical distribution, the lesser Green's function $G^<$, which is natually included in the contour-ordered Green's function formalism, is crucial in order to know the electron density information.

3.2 Ensemble average in non-equilibrium

To proceed we need to obtain an ensemble average under non-equilibrium condition. First the system Hamiltonian $\mathcal{H}$ can be divided as follows,

$$\mathcal{H}(t) = H + H'(t) = H_0 + H_i + H'(t), \tag{3.11}$$

where $H = H_0 + H_i$. H_0 is the non-interacting (quadratic) free particle Hamiltonian, and H_i indicates a possible interaction, for example, the electron-vibration interaction of this study. $H'(t)$ is the Hamiltonian that drives the system out of equilibrium. In the transport problem, a finite bias corresponds to $H'(t)$. We assume that the system is in equilibrum for $t < t_0$. Thus the ensemble average for an operator $\mathcal{O}$ is given by

$$\langle\mathcal{O}\rangle = \mathrm{Tr}\left[\rho(H)\mathcal{O}\right], \tag{3.12}$$

where $\rho(H) = e^{-\beta H}/\mathrm{Tr}[e^{-\beta H}]$.

Let us consider that H' is turned on at $t = t_0$ and kept switched on for $t \geq t_0$. From $t = t_0$ the time evolution of the ensemble average is obtained by using the time-evolved density operator $\rho(t)$,

$$\rho(t) = \mathcal{U}(t, t_0)\rho(H)\mathcal{U}^\dagger(t, t_0), \tag{3.13}$$

where $\mathcal{U}(t, t_0) = \mathcal{T}\exp[-\frac{i}{\hbar}\int_{t'}^{t} d\tau \mathcal{H}(\tau)]$ is the time evolution operator with respect to the *full* Hamiltonian $\mathcal{H}$. Thus the ensemble average becomes

$$\langle \mathcal{O} \rangle(t) = \mathrm{Tr}\left[\rho(t)\mathcal{O}\right]. \tag{3.14}$$

This can be readily written in the Heisenberg picture,

$$\langle \mathcal{O} \rangle(t) = \mathrm{Tr}\left[\rho(H)\mathcal{O}_{\mathcal{H}}(t)\right]. \tag{3.15}$$

Furthermore $\mathcal{O}_{\mathcal{H}}$ can be transformed in the interaction picture with respect to H, which is time-independent. For the reference time t_0, we have

$$\mathcal{O}_{\mathcal{H}}(t) = V^\dagger(t, t_0)\mathcal{O}_H(t)V(t, t_0), \tag{3.16}$$

where

$$V(t, t_0) = \mathcal{T}\exp\left[-\frac{i}{\hbar}\int_{t_0}^{t} dt' H'_H(t')\right]. \tag{3.17}$$

Here $H'_H(t)$ is the operator $H'(t)$ written in the interaction picture with respect to H. By introducing the closed path c in Fig.(3-2), Eq.(3.16) is equivalently rewritten as follows [77],

$$\mathcal{O}_{\mathcal{H}}(t) = \mathcal{T}_c\left[\exp\left(-\frac{i}{\hbar}\int_c d\tau H'_H(\tau)\right)\mathcal{O}_H(t)\right] \tag{3.18}$$

This formulation will be used for the perturbative expansion of the contour-ordered Green's functions in the following section.

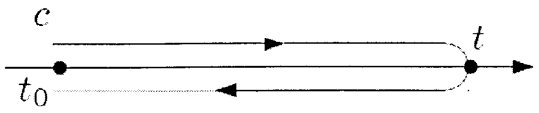

Figure 3-2: Closed time contour, starting at the reference time t_0, changing its direction at t, and returning to t_0.

3.3 Perturbative Expansion

In the definition of the contour-ordered Green's functions Eq. (3.3), the time evolution of the field operator $\psi(t)$ is governed by the full Hamiltonian $\mathcal{H}$, which cannot be exactly solved. The key strategy to obtain the contour-ordered Green's functions is to rewrite the field operator in the interaction picture with respect to the free-particle quadratic operator H_0, which is solvable. This transformation enables us to take advantage of Wick's theorem and Feynman diagram rules [76].

As an intermediate step one can write the contour-ordered Green's function $G(\tau, \tau')$ in the interaction picture with respect to H by using the formulation discussed in the previous section,

$$G(\tau,\tau') = \frac{1}{i\hbar}\left\langle \mathcal{T}_c\left(\exp\left(-\frac{i}{\hbar}\int_c dt H'_H(t)\right)\psi_H(\tau)\psi^\dagger_H(\tau')\right)\right\rangle . \tag{3.19}$$

We can separate the effect of the time-dependent term $H'(t)$ in the form of the S-operator, but the field operator is still written with respect to H, which contains the interaction term H_i. By taking the transformation from the interaction picture with respect to H to one with respect to H_0 once again, one can readily write the contour-ordered Green's functions in the following way,

$$\begin{aligned} G(\tau,\tau') &= \frac{1}{i\hbar}\left\langle \mathcal{T}_c\left(\exp\left(-\frac{i}{\hbar}\int_c dt H^i_{H_0}(t) + H'_{H_0}(t)\right)\psi_{H_0}(\tau)\psi^\dagger_{H_0}(\tau')\right)\right\rangle & (3.20)\\ &= \frac{1}{i\hbar}\frac{\mathrm{Tr}\left[e^{-\beta H}\mathcal{T}_c\left(e^{\left(-\frac{i}{\hbar}\int_c dt H^i_{H_0}(t)+H'_{H_0}(t)\right)}\psi_{H_0}(\tau)\psi^\dagger_{H_0}(\tau')\right)\right]}{\mathrm{Tr}\left(e^{-\beta H}\right)} & (3.21)\end{aligned}$$

The Boltzmann factor $e^{-\beta H}$ is also needed to be expressed in the interaction

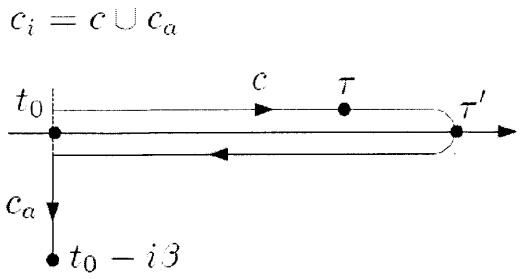

Figure 3-3: Extended contour c_i including the imaginary time contour c_a for thermal statistics.

picture with respect to the free particle Hamiltonian H_0. When we introduce an imaginary time path c_a from t_0 to $t_0 - i\beta$, the Boltzmann factor satisfies the following relation,

$$e^{-\beta H} = e^{-\beta H_0} \mathcal{T}_{c_a} \exp\left(-\frac{i}{\hbar}\int_{t_0}^{t_0-i\beta} dt H^i_{H_0}(t)\right). \tag{3.22}$$

With this relation, known as the Dyson formula [77], all the operators in the contour-ordered Green's functions are written in the interaction picture with respect to H_0. In the numerator the two contour ordering operations $\mathcal{T}_c$ and $\mathcal{T}_{c_a}$ can be merged by combining the closed-time contour c and the imaginary-time contour c_a and defining a new contour c_i as shown in Fig. 3-3. On the new contour c_i, the contour-ordered Green's function becomes

$$G(\tau,\tau') = \frac{1}{i\hbar}\frac{\mathrm{Tr}\left[e^{-\beta H_0}\mathcal{T}_{c_i}\left(e^{\left(-\frac{i}{\hbar}\int_{c_i} dt H^i_{H_0}(t)\right)} e^{\left(-\frac{i}{\hbar}\int_c dt H'_{H_0}(t)\right)} \psi_{H_0}(\tau)\psi^\dagger_{H_0}(\tau')\right)\right]}{\mathrm{Tr}\left[e^{-\beta H_0}\mathcal{T}_{c_a}\left(e^{\left(-\frac{i}{\hbar}\int_{t_0}^{t_0-i\beta} dt H^i_{H_0}(t)\right)}\right)\right]} \tag{3.23}$$

The contribution of the contour c_a, which contains only the interaction H^i, indicates the initial correlation between particles via the interaction H^i. If one is interested only in the physics after the initial correlation is damped out, or in the steady state situation, one may set $t_0 \to -\infty$ and safely neglect the contribution of the contour c_a [78]. Exploiting the unitarity of the time-evolution operator, the closed-time contour can be extended to $t \to \infty$. Thus the time contour to describe the steady state has two time branches: the upper branch c_1 starting at $t \to -\infty$ and ending at $t \to \infty$,

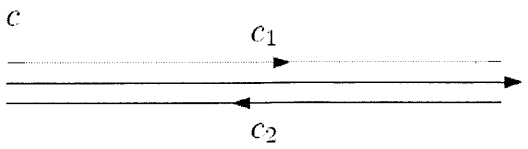

Figure 3-4: The Schwinger-Keldysh contour extended to $t = \pm\infty$.

and the lower branch c_2 starting at $t \to \infty$ and moving back to $t \to -\infty$. This time contour is called the *Schwinger-Keldysh* contour. To sum up, the contour-ordered Green's functions for the steady state is

$$G(\tau, \tau') = \frac{1}{i\hbar}\mathrm{Tr}\left[\rho(H_0)\mathcal{T}_c\left(e^{\left(-\frac{i}{\hbar}\int_c dt H'_{H_0}(t)\right)}e^{\left(-\frac{i}{\hbar}\int_c dt H^i_{H_0}(t)\right)}\psi_{H_0}(\tau)\psi^\dagger_{H_0}(\tau')\right)\right], \quad (3.24)$$

where $\rho(H_0) = \frac{e^{-\beta H_0}}{\mathrm{Tr}[e^{-\beta H_0}]}$.

Now, the contour-ordered Green's functions can be expanded in terms of the unperturbed Green's functions G_0 as one did in equilibrium Green's function theory [76]. The unperturbed Green's function is defined as

$$G_0(\tau, \tau') = \frac{1}{i\hbar}\left\langle \mathcal{T}_c\psi_{H_0}(\tau)\psi^\dagger_{H_0}(\tau')\right\rangle_0, \quad (3.25)$$

where $\langle\cdots\rangle_0 = \mathrm{Tr}\left[\rho(H_0)\cdots\right]$. Because the contour-ordered Green's functions and the equilibrium Green's functions are topologically equivalent except for time ordering, Wick's theorem and Feynman diagrammatic rules can be readily applied. Furthermore, one can write down the Dyson equation for the contour-ordered Green's functions,

$$G(\tau, \tau') = G_0(\tau, \tau') + \int_c d\tau_1 \int_c d\tau_2 G_0(\tau, \tau_1)\Sigma(\tau_1, \tau_2)G(\tau_2, \tau'), \quad (3.26)$$

where $\Sigma(\tau_1, \tau_2)$ is the self-energy that contains all possible connected diagrams.

Contour C	Real Axis t
$C = \int_c AB$	$C^< = \int_t [A^r B^< + A^< B^a]$ $C^r = \int_t A^r B^r$
$D = \int_c ABC$	$D^< = \int_t [A^r B^r C^< + A^r B^< C^a + A^< B^a C^a]$ $D^r = \int_t A^r B^r C^r$
$C(\tau, \tau') = A(\tau, \tau')B(\tau, \tau')$	$C^<(t, t') = A^<(t, t')B^<(t, t')$ $C^r(t, t') = A^<(t, t')B^r(t, t') + A^r(t, t')B^<(t, t')$ $+A^r(t, t')B^r(t, t')$
$C(\tau, \tau') = A(\tau, \tau')B(\tau', \tau)$	$C^<(t, t') = A^<(t, t')B^>(t', t)$ $C^r(t, t') = A^<(t, t')B^a(t', t) + A^r(t, t')B^<(t', t)$

Table 3.1: Several examples of Langreth's rules

3.4 Langreth's rules: from contour to real time

We have discussed the systematic perturbative expansion of the contour-ordered Green's functions. However, since the time argument for the contour-ordered Green's functions lies on the closed-path time contour, one needs to convert to real time in order to get physical information desired. For example, to access the electron density of the system, we need to extract the lesser Green's function $G^<(t, t')$ from $G(\tau, \tau')$. This conversion rule is known as Langreth's rule [33]. Let us consider the following quantity, defined on the Schwinger-Keldysh contour c,

$$C(\tau, \tau') = \int_c d\tau_1 A(\tau, \tau_1)B(\tau_1, \tau'). \tag{3.27}$$

According to Langreth's rule, the lesser and retarded parts of $C(\tau, \tau')$ can be calculated in the following way,

$$C^<(t, t') = \int_{-\infty}^{\infty} dt_1 \left(A^r(t, t_1)B^<(t_1, t') + A^<(t, t_1)B^a(t_1, t')\right) \tag{3.28}$$

$$C^r(t, t') = \int_{-\infty}^{\infty} dt_1 A^r(t, t_1)B^r(t_1, t'). \tag{3.29}$$

Note that the contour integral is replaced by the time integral from $-\infty$ to ∞. Table (3.1) shows several examples of Langreth's rules.

3.5 Kinetic Equation

Now we can derive kinetic equations for the retarded, advanced, lesser, and greater Green's functions by applying Langreth's rule to the Dyson equation for the contour-ordered Green's function Eq.(3.26).

For the retarded and the advanced Green's functions, one can obtain the usual Dyson's equation that one may be familiar with in the equilibrium theory [76].

$$G^{r,a}(t,t') = G_0^{r,a}(t,t') + \int_{-\infty}^{\infty} dt_1 dt_2 G_0^{r,a}(t,t_1)\Sigma^{r,a}(t_1,t_2)G^{r,a}(t_2,t') \tag{3.30}$$

Similary one can obtain the kinetic equation for the lesser and the greater Green's functions, which is named the *Keldysh* equation. For the lesser Green's function,

$$\begin{aligned} G^<(t,t') &= G_0^<(t,t') + \int_{-\infty}^{\infty} dt_1 dt_2 \left[G_0^r(t,t_1)\Sigma^r(t_1,t_2)G^<(t_2,t')\right. \\ &\quad \left. + G_0^r(t,t_1)\Sigma^<(t_1,t_2)G^a(t_2,t') + G_0^<(t,t_1)\Sigma^a(t_1,t_2)G^a(t_2,t')\right] \\ &= G_0^< + G_0^r \cdot \Sigma^r \cdot G^< + G_0^r \cdot \Sigma^< \cdot G^a + G_0^< \cdot \Sigma^a \cdot G^a \end{aligned}$$

Here a shorthand notation for the integral is introduced:

$$A \cdot B \equiv \int_{-\infty}^{\infty} dt_1 A(t,t_1)B(t_1,t') \tag{3.31}$$

Iterating this equation for $G^<$ one can obtain the following closed equation,

$$G^< = (1 + G^r \cdot \Sigma^r) \cdot G_0^< \cdot (1 + G^a \cdot \Sigma^a) + G^r \cdot \Sigma^< \cdot G^a \tag{3.32}$$

From the Dyson equation Eq.(3.30), $(1 + G^r \cdot \Sigma^r) \cdot G_0^< = G^r \cdot (G_0^r)^{-1} \cdot G_0^<$ holds. The equation of motion for $G^<$ leads to $(G_0^r)^{-1} \cdot G_0^< = 0$ plus a boundary term introduced by the inverse of the integral operator. As pointed out in Ref. [24], the boundary term contains the memory of the initial condition. In the steady state problem, this initial memory can be neglected. Thus we reach the steady state Keldysh equation

for the lesser Green's function

$$G^<(t,t') = \int_{-\infty}^{\infty} dt_1 dt_2 G^r(t,t_1)\Sigma^<(t_1,t_2)G^a(t_2,t'). \tag{3.33}$$

For the greater one one can obtain the same form of the Keldysh equation

$$G^>(t,t') = \int_{-\infty}^{\infty} dt_1 dt_2 G^r(t,t_1)\Sigma^>(t_1,t_2)G^a(t_2,t'). \tag{3.34}$$

In steady state the Green's function $G(t,t')$ depends on a time difference $t-t'$. Using Fourier tranformations and the convolution theorem, one can obtain the Dyson equation and the Keldysh equation in energy space,

$$G^{r,a}(\omega) = G_0^{r,a}(\omega) + G_0^{r,a}(\omega)\Sigma^{r,a}(\omega)G^{r,a}(\omega) \tag{3.35}$$

$$G^{>,<}(\omega) = G^r(\omega)\Sigma^{>,<}(\omega)G^a(\omega) \tag{3.36}$$

In the next Chapter we will apply this formalism to nanostructures coupled to two electrodes and in the presence of electron-vibration interactions.

Chapter 4

Electron-Vibration Interactions in Molecular Junctions

In the previous Chapter we reviewed the general formulation for non-equilibrium Green's functions, which enables us to calculate physical properties of interacting system out of equilibrium. In this chapter we calculate the contour-ordered Green's functions in the presence of electron-vibration interactions in a two-terminal geometry.

4.1 Hamiltonian

Our system consists of three sub-systems: a left electrode, a right electrode, and a device region that contains the vibrating molecule. Conducting electrons are assumed to be scattered off by molecular vibrations only inside the device region. In contrast, electrons in the electrodes are described by non-interacting quasi-particles with phonons, or between each other (In the latter case, they do, but are renormalized by DFT). Each electrode plays the role of an electron reservoir in equilibrium. The chemical potential difference $\mu_L - \mu_R$ leads to the nonequilibrium state in the device region. The corresponding Hamiltonian is expressed in terms of second quantized operators as follows:

$$\mathcal{H} = H_D + H_{lead} + H_T \tag{4.1}$$

$$H_D = H_0 + H_{el-vib} + H_{vib} \tag{4.2}$$

$$H_0 = \sum_{i,j} \varepsilon_{i,j} d_i^\dagger d_j \tag{4.3}$$

$$H_{vib} = \sum_{\lambda} \hbar\omega_\lambda \left(a_\lambda^\dagger a_\lambda + \frac{1}{2} \right) \tag{4.4}$$

$$H_{el-vib} = \sum_{\lambda} \sum_{i,j} \mathcal{M}_{ij}^{\lambda} d_i^\dagger d_j \left(a_\lambda^\dagger + a_\lambda \right) \tag{4.5}$$

$$H_{lead} = \sum_{\alpha=L,R} \sum_{k} \varepsilon_{\alpha k} c_{\alpha k}^\dagger c_{\alpha k} \tag{4.6}$$

$$H_T = \sum_{\alpha=L,R} \sum_{k} \sum_{i} \left[V_{\alpha k,i} c_{\alpha k}^\dagger d_i + V_{\alpha k,i}^* d_i^\dagger c_{\alpha k} \right] \tag{4.7}$$

Here d_i and $d_i^\dagger$ in H_D are annihilation and creation operators for electrons in the device region. In this study we choose localized Wannier functions as basis. $c_{\alpha k}$ and $c_{\alpha k}^\dagger$ in H_{lead} are annihilation and creation operators for the non-interacting Kohn-Sham electrons in the αth electrode. k is a set of quantum numbers for the electrode electrons. a_λ and $a_\lambda^\dagger$ are the bosonic operators corresponding to the λth molecular vibration. H_T describes the tunneling between the device region and the electrodes.

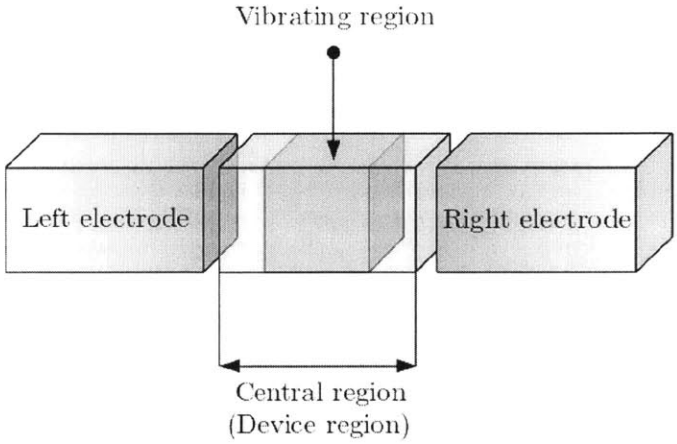

Figure 4-1: Schematic geometry of a two-terminal set-up. The electron-vibration interaction exists only inside the device region.

Because the electron-vibration interaction H_{el-vib} does not distinguish between spin degrees of freedom, the spin index is not explicitly specified.

4.2 Device Green's function

Now we want to calculate the *full* device Green's functions

$$G_{ij}(\tau,\tau') = \frac{1}{i\hbar}\left\langle \mathcal{T}_c d_i(\tau) d_j^\dagger(\tau')\right\rangle \tag{4.8}$$

in the presence of the coupling to electrodes and the interaction with local vibrations. As seen in the previous chapter, $G(\tau,\tau')$ satisfies the Dyson equation,

$$G(\tau,\tau') = g(\tau,\tau') + \left[g\cdot(\Sigma_{lead}+\Sigma_{vib})\cdot G\right](\tau,\tau') \tag{4.9}$$

Here $G(\tau,\tau')$ can be interpreted as a matrix Green's function whose (i,j) component is $G_{ij}(\tau,\tau')$. $g_{ij}(\tau,\tau')$ is an *isolated* device Green's function when there is no interaction with electrodes and local vibrations:

$$g_{ij}(\tau,\tau') = \frac{1}{i\hbar}\left\langle \mathcal{T}_c d_i(\tau) d_j^\dagger(\tau')\right\rangle_{H_0}. \tag{4.10}$$

Here we put the subscript H_0 to emphasize that its dynamics is governed solely by H_0. Σ_{lead} is the *lead* self-energy coming purely from coupling with electrodes. Σ_{vib} is the electron-vibration self-energy that is a sum of all the connected irreducible diagrams containing the electron-vibration interaction [76].

Applying Langreth's rules and taking the Fourier transformation to the energy space, the Dyson and Keldysh equations for the device Green's function are obtained as

$$G^r(\varepsilon) = g^r(\varepsilon) + g^r(\varepsilon)\left[\Sigma^r_{lead}(\varepsilon)+\Sigma^r_{vib}(\varepsilon)\right]G^r(\varepsilon) \tag{4.11}$$

$$G^<(\varepsilon) = G^r(\varepsilon)\left[\Sigma^<_{lead}(\varepsilon)+\Sigma^<_{vib}(\varepsilon)\right]G^a(\varepsilon). \tag{4.12}$$

Here we can simplify the Dyson equation further by introducing the *non-interacting* device Green's function $G_0(\tau, \tau')$ that is calculated without the electron-vibration interactions, but only with connections to the electrodes,

$$G_{0,ij}(\tau, \tau') = \frac{1}{i\hbar} \left\langle \mathcal{T}_c d_i(\tau) d_j^\dagger(\tau') \right\rangle_{H_0+H_T}. \tag{4.13}$$

Note that the subscript $H_0 + H_T$ indicates that the device region is coupled to the electrodes. For this non-interacting Green's function one can write down the Dyson equation for the retarded part,

$$G_0^r(\varepsilon) = g^r(\varepsilon) + g^r(\varepsilon)\Sigma_{lead}^r(\varepsilon)G_0^r(\varepsilon). \tag{4.14}$$

Using the fact that $[g^r(\varepsilon)]^{-1} = [(\varepsilon + i0^+) - H_0]$, Eqs. (4.11) and (4.14) are rewritten as

$$G^r(\varepsilon) = \frac{1}{(\varepsilon + i0^+) - H_0 - \Sigma_{lead}^r - \Sigma_{vib}^r} \tag{4.15}$$

$$G_0^r(\varepsilon) = \frac{1}{(\varepsilon + i0^+) - H_0 - \Sigma_{lead}^r}. \tag{4.16}$$

Rearranging these equations, one can express the Dyson equation for $G^r(\varepsilon)$ in terms of $G_0^r(\varepsilon)$,

$$G^r(\varepsilon) = \frac{1}{[G_0^r]^{-1} - \Sigma_{vib}^r(\varepsilon)} \tag{4.17}$$

$$= G_0^r(\varepsilon) + G_0^r(\varepsilon)\Sigma_{vib}^r(\varepsilon)G^r(\varepsilon). \tag{4.18}$$

4.3 Self-energy

The next step to obtain the full device Green's function is to calculate the lead self-energy and the electron-vibration self-energy. The self-energy in the Dyson equation is a collection of all the possible *irreducible* diagrams, in which *irreducible* means that the diagram cannot be divided into two pieces by cutting one device Green's function [76]. While the lead self-energy can be exactly calculated when electrons in

the electrodes are assumed to be in equilibrium, the electron-vibration self-energy is approximatedly calculated by using diagrammatic perturbation theory.

4.3.1 Lead Self-energy

We first discuss the lead self-energy $\Sigma_{lead}(\tau,\tau')$. In case of coupling to the electrodes one can have the following irreducible term,

$$\Sigma_{lead,ij}(\tau,\tau') = \sum_{\alpha=L,R} \Sigma_{\alpha,ij}(\tau,\tau') = \sum_{\alpha=L,R}\sum_{k} V^{*}_{\alpha k,i} g_{\alpha k}(\tau,\tau') V_{\alpha k,j}, \tag{4.19}$$

where

$$g_{\alpha k}(\tau,\tau') = \frac{1}{i\hbar}\left\langle \mathcal{T}_c c_{\alpha k}(\tau) c^{\dagger}_{\alpha k}(\tau')\right\rangle_0 \tag{4.20}$$

is a *free* Green's function for an electron in the αth electrode decoupled to its surrounding. The retarded, advanced, lesser, and greater parts of the lead self-energy are obtained straightforwardly:

$$\Sigma^{r,a}_{lead,ij}(\varepsilon) = \sum_{\alpha=L,R}\sum_{k} V^{*}_{\alpha k,i} g^{r,a}_{\alpha k}(\varepsilon) V_{\alpha k,j} \tag{4.21}$$

$$\Sigma^{>,<}_{lead,ij}(\varepsilon) = \sum_{\alpha=L,R}\sum_{k} V^{*}_{\alpha k,i} g^{>,<}_{\alpha k}(\varepsilon) V_{\alpha k,j} \tag{4.22}$$

For the electrode assumed to be in equilibrium with the chemical potential μ_α, the lesser and greater free electrode Green's functions are

$$g^{<}_{\alpha k}(\varepsilon) = i2\pi n_F(\varepsilon-\mu_\alpha)\delta(\varepsilon-\varepsilon_{\alpha k}) \tag{4.23}$$

$$g^{>}_{\alpha k}(\varepsilon) = i2\pi\left[n_F(\varepsilon-\mu_\alpha)-1\right]\delta(\varepsilon-\varepsilon_{\alpha k}). \tag{4.24}$$

Thus the lesser and greater parts of the lead self-energy are rewritten as

$$\Sigma^{<}_{lead,ij}(\varepsilon) = \sum_{\alpha=L,R} i n_F(\varepsilon-\mu_\alpha)\Gamma^{\alpha}_{ij}(\varepsilon) \tag{4.25}$$

$$\Sigma^{>}_{lead,ij}(\varepsilon) = \sum_{\alpha=L,R} i\left[n_F(\varepsilon-\mu_\alpha)-1\right]\Gamma^{\alpha}_{ij}(\varepsilon), \tag{4.26}$$

where

$$\Gamma^{\alpha}_{ij}(\varepsilon) \equiv 2\pi \sum_{k} V^{*}_{\alpha k,i} V_{\alpha k,j} \delta(\varepsilon - \varepsilon_{\alpha k}). \tag{4.27}$$

Γ^{α} is called a *broadening* function because it physically describes broadening of an electronic level when a level is coupled to electrodes. Using the relation $g^{>} - g^{<} = g^{r} - g^{a}$, the broadening function can be obtained from the retarded and advanced lead self-energies,

$$\Gamma^{\alpha}(\varepsilon) = i\left[\Sigma^{r}_{\alpha}(\varepsilon) - \Sigma^{a}_{\alpha}(\varepsilon)\right] = i\left[\Sigma^{r}_{\alpha}(\varepsilon) - (\Sigma^{r}_{\alpha}(\varepsilon))^{\dagger}\right]. \tag{4.28}$$

Once one can calculate the retarded lead self-energy, then one can directly obtain the broadening function Γ, and the lesser and greater self-energies $\Sigma^{>,<}_{lead}$.

4.3.2 Electron-Vibration Self-energy

As stated before, the electron-vibration self-energy consists of all the irreducible connected diagrams. Building blocks of the diagrams are the non-interacting electron device Green's function

$$G_{0,ij}(\tau,\tau') = \frac{1}{i\hbar}\left\langle \mathcal{T}_c d_i(\tau) d^{\dagger}_j(\tau') \right\rangle_{H_0+H_T}, \tag{4.29}$$

the unperturbed vibration Green's function

$$D_{0,\lambda}(\tau,\tau') = \frac{1}{i\hbar}\left\langle \mathcal{T}_c \left[a^{\dagger}_{\lambda}(\tau) + a_{\lambda}(\tau)\right]\left[a^{\dagger}_{\lambda}(\tau') + a_{\lambda}(\tau')\right]\right\rangle_{0}, \tag{4.30}$$

and the vertex factor $\mathcal{M}^{\lambda}$. The retarded and lesser vibration Green's functions in the energy representation are

$$D^{r}_{0,\lambda}(\varepsilon) = \frac{1}{\varepsilon - \hbar\omega_{\lambda} + i0^{+}} - \frac{1}{\varepsilon + \hbar\omega_{\lambda} + i0^{+}} \tag{4.31}$$

$$D^{<}_{0,\lambda}(\varepsilon) = -2\pi i\left[(N_{\lambda}+1)\,\delta(\varepsilon + \hbar\omega_{\lambda}) + N_{\lambda}\delta(\varepsilon - \hbar\omega_{\lambda})\right]. \tag{4.32}$$

Figure 4-2: Lowest-order electron-vibration diagrams: (a) Hartree and (b) Fock. The arrowed line and wiggly line indicate electronic and vibrational Green's functions. The black filled circle represents the vertex factor of the electron-vibration interaction.

For the isolated vibration N_λ obeys the Bose-Einstein distribution $n_B(\hbar\omega_\lambda) = \frac{1}{e^{\beta\hbar\omega_\lambda}-1}$. In reality the molecule is mechanically coupled to bulk phonons in the electrodes. In addition, when conducting electrons are scattered off by the molecular vibrations due to the electron-vibration coupling, the electrons can emit or absorb molecular vibrons. As a result, the vibron population can deviate from Bose-Einstein equilibrium. These effects may result in two changes in the vibrational Green's function: a vibrational frequency shift $\omega_\lambda \to \omega_\lambda + \Delta\omega_\lambda$, and a finite lifetime $i0^+ \to i\eta$. The delta-function may be replaced by Lorentzian with the broadening correponding to the lifetime. In the weak coupling regime one might use the same form of the unperturbed Green's function as a first approximation, except for the nonequilibrium vibron occuption $N_\lambda \neq n_B(\hbar\omega_\lambda)$. This is called the *vibronic quasiparticle approximation* [82]. We will discuss how to calculate the non-equilibrium vibron occupation number N_λ in the next chapter.

With these components one can generate a variety of diagrams by following Feynman rules as one does in the equilibrium theory [9]. Because the exact self-energy includes an infinite number of irreducible digrams, it is impossible to calculate the exact self-energy. For a real calculation we have to replace the exact self-energy by an approximate one. In this study the lowest-order diagrams, which are in the second order of $\mathcal{M}^\lambda$, are considered: *Hartree* and *Fock* diagrams in Fig. 4-2. We discuss several methods to calculate the full device Green's functions with these two diagrams. They are different in terms of the order of $\mathcal{M}^\lambda$ and the summation of the diagrams.

Lowest-order approximation

The simplist way to calculate the self-energy is just to compute the Hartree and Fock diagrams by using $G_{0,ij}$ and $D_{0,\lambda}$ in the second order of the electron-vibration interaction $\mathcal{M}^{\lambda}$. This approximation can be valid in the weak coupling regime. According to Feynman rules, the Hartree and Fock terms are evaluated to be

$$\Sigma^{H}_{vib,(2)} = -i2\sum_{\lambda}\mathcal{M}^{\lambda}D_0(\lambda,\varepsilon=0)\mathrm{Tr}\left[G_0^{<}(\tau=0,\tau'=0)\mathcal{M}^{\lambda}\right], \tag{4.33}$$

$$\Sigma^{F}_{vib,(2)} = i\sum_{\lambda}\mathcal{M}^{\lambda}D_{0,\lambda}(\tau,\tau')G_0(\tau,\tau')\mathcal{M}^{\lambda}. \tag{4.34}$$

The factor 2 in the Hartree diagram accounts for the spin degeneracy in the electron loop in the diagram. The subscript (2) indicates that these diagrams are second order in the vertex factor $\mathcal{M}^{\lambda}$.

When Langreth's rule is applied, the Hartree term is written as

$$\Sigma^{H,r}_{vib,(2)} = -2i\sum_{\lambda}\frac{2}{\hbar\omega_{\lambda}}\int_{-\infty}^{\infty}\frac{d\varepsilon'}{2\pi}\mathcal{M}^{\lambda}\mathrm{Tr}\left[G_0^{<}(\varepsilon')\right], \tag{4.35}$$

$$\Sigma^{H,>,<}_{vib,(2)} = -2i\sum_{\lambda}\mathcal{M}^{\lambda}D_0^{>,<}(\lambda,\varepsilon=0)\mathrm{Tr}\left[G_0^{<}(0,0)\mathcal{M}^{\lambda}\right]=0. \tag{4.36}$$

Note that the Hartree retarded contribution is energy-independent, which means that it gives a static correction to the electronic potential. The lesser and greater contributions identically vanish.

In the energy representation the Fock term reads

$$\Sigma^{F,r}_{vib,(2)}(\varepsilon) = i\sum_{\lambda}\int_{-\infty}^{\infty}\frac{d\varepsilon'}{2\pi}\mathcal{M}^{\lambda}\left[D^{r}_{0,\lambda}(\varepsilon-\varepsilon')G_0^{>}(\varepsilon')+D^{<}_{0,\lambda}(\varepsilon-\varepsilon')G_0^{r}(\varepsilon')\right]\mathcal{M}^{\lambda}, \tag{4.37}$$

$$\Sigma^{F,>,<}_{vib,(2)}(\varepsilon) = i\sum_{\lambda}\int_{-\infty}^{\infty}\frac{d\varepsilon'}{2\pi}\mathcal{M}^{\lambda}D^{>,<}_{0,\lambda}(\varepsilon-\varepsilon')G_0^{>,<}(\varepsilon')\mathcal{M}^{\lambda}. \tag{4.38}$$

In fact the retarded Fock term can be expressed in terms of the lesser and greater

ones via the Kramers-Krönig relation as follows:

$$\Sigma^{F,r}_{vib,(2)}(\varepsilon) = \frac{1}{2}\left[\Sigma^{F,>}_{vib,(2)} - \Sigma^{F,<}_{vib,(2)}\right](\varepsilon) - \frac{i}{2}\mathcal{H}_{\varepsilon'}\left[\Sigma^{F,>}_{vib,(2)}(\varepsilon') - \Sigma^{F,<}_{vib,(2)}(\varepsilon')\right](\varepsilon), \quad (4.39)$$

where

$$\mathcal{H}_{\varepsilon'}\left[f(\varepsilon')\right](\varepsilon) \equiv \frac{1}{\pi}\mathcal{P}\int_{-\infty}^{\infty} d\varepsilon' \frac{f(\varepsilon')}{\varepsilon' - \varepsilon} \quad (4.40)$$

is called the *Hilbert* transformation.

With the lowest-order irreducible diagrams one can calculate the full device Green's function G_{ij} in two ways. The first one is to insert $\Sigma^r_{vib,(2)} = \Sigma^{H,r}_{vib,(2)} + \Sigma^{F,r}_{vib,(2)}$ into Σ^r_{vib} in the Dyson equation Eq.(4.17). Essentially this solution is the same as a geometrical series, obtained by expanding Eq.(4.18) iteratively,

$$\begin{aligned} G^r(\varepsilon) &\approx G^r_0 + G^r_0\Sigma^r_{vib,(2)}G^r_0 + G^r_0\Sigma^r_{vib,(2)}G^r_0\Sigma^r_{vib,(2)}G^r_0 + \cdots & (4.41)\\ &= \left[(G^r_0)^{-1} - \Sigma^r_{vib,(2)}\right]^{-1} \equiv G^r_{1BA}(\varepsilon) & (4.42)\end{aligned}$$

With $G^r_{1BA}(\varepsilon)$ the lesser and greater ones are readily obtained from the Keldysh equation Eq.(4.12),

$$G^{>,<}_{1BA}(\varepsilon) = G^r_{1BA}(\varepsilon)\left[\Sigma^{>,<}_{lead}(\varepsilon) + \Sigma^{>,<}_{vib,(2)}(\varepsilon)\right]G^a_{1BA}(\varepsilon) \quad (4.43)$$

This is called the *first Born* approximation.

The second method is to truncate the geometrical series Eq.(4.41) and to keep the lowest-order term only,

$$G^r(\varepsilon) \approx G^r_0 + G^r_0\Sigma^r_{vib.(2)}G^r_0 \equiv G^r_{(2)} \quad (4.44)$$

Similarly for the lesser and greater Green's functions one can keep up to the lowest-order term,

$$G^{>,<}(\varepsilon) \approx G^r_0\Sigma^{>,<}_{lead}G^a_0 + G^r_0\Sigma^{>,<}_{vib,(2)}G^a_0 + G^r_{(2)}\Sigma^{>,<}_{lead}G^a_0 + G^r_0\Sigma^{>,<}_{lead}G^a_{(2)} \equiv G^{>,<}_{(2)}(\varepsilon) \quad (4.45)$$

Throughout this study we call this the *lowest-order expansion* [72, 27].

However, one should be very careful in using these approximated Green's functions. One should make sure whether the approximation used in the theory is physically reasonable. For our problem, where a finite-bias current will be calculated, the most important criterion is that the current conservation must hold, together with the approximation to calculate self-energy and the Green's function. Unfortunately the first Born approximation, which is often used in equilibrium theory, does not guarantee current conservation. In constrast, when the current is calculated up to the lowest order of the electron-vibration interaction $\mathcal{M}^\lambda$ with $G^r_{(2)}$ and $G^{>,<}_{(2)}$, it satisfies the current conservation condition. We will discuss this issue in detail in the next chapter.

Self-Consistent Born Approximation

One can further improve the Green's function calculation together with the Hartree and Fock diagrams. Let us replace the non-interacting device Green's function $G_0^{r,>,<}$ by the full Green's function $G^{r,>,<}$ in the Hartree and Fock diagrams,

$$\Sigma^{H,r}_{vib,SCBA} = -2i\sum_\lambda \frac{2}{\hbar\omega_\lambda}\int_{-\infty}^{\infty}\frac{d\varepsilon'}{2\pi}\mathcal{M}^\lambda \mathrm{Tr}\left[G^<(\varepsilon')\right], \tag{4.46}$$

$$\Sigma^{F,r}_{vib,SCBA}(\varepsilon) = i\sum_\lambda \int_{-\infty}^{\infty}\frac{d\varepsilon'}{2\pi}\mathcal{M}^\lambda\left[D^r_{0,\lambda}(\varepsilon-\varepsilon')G^>(\varepsilon') + D^<_{0,\lambda}(\varepsilon-\varepsilon')G^r(\varepsilon')\right]\mathcal{M}^\lambda, \tag{4.47}$$

$$\Sigma^{F,>,<}_{vib,SCBA}(\varepsilon) = i\sum_\lambda \int_{-\infty}^{\infty}\frac{d\varepsilon'}{2\pi}\mathcal{M}^\lambda D^{>,<}_{0,\lambda}(\varepsilon-\varepsilon')G^{>,<}(\varepsilon')\mathcal{M}^\lambda. \tag{4.48}$$

With the Dyson and Keldysh equations

$$G^r(\varepsilon) = G^r_0(\varepsilon) + G^r_0(\varepsilon)\Sigma^r_{vib}(\varepsilon)G^r(\varepsilon) \tag{4.49}$$

$$G^<(\varepsilon) = G^r(\varepsilon)\left[\Sigma^<_{lead}(\varepsilon) + \Sigma^<_{vib}(\varepsilon)\right]G^a(\varepsilon). \tag{4.50}$$

one has a closed set of the equations for $G^{r,>,<}$ and $\Sigma^{r,>,<}_{vib}$ to be solved in a self-consistent way. This self-consistent calculation method is called the *self-consistent*

Born approximation (SCBA). From a viewpoint of the diagrammatic perturbation, this approximation includes more diagrams than the first Born approximation or the lowest-order expansion. Moreover, because the SCBA satisfies the current conservation, it is a relevant approximation to a finite-bias transport problem. In this study the lowest-order expansion and the self-consistent Bǒrn approximation are adopted for the electron transport calculation.

Chapter 5

Quantum Transport with Electron-Vibration Interactions

The Landauer-Büttiker formalism is the basic quantum mechanical description for the electron transport, and has been widely used in many nanoscale transport problems. However it is suitable only to non-interacting electrons or quasiparticles. In 1992 Y. Meir and N. S. Wingreen developed a generalized transport formalism that enables us to take into account interaction effects on transport properties [65]. The Meir-Wingreen transport formalism, which we want to discuss here, can deal not only with electron-vibration interactions, but also with a variety of interactions, from electron-electron to electron-photon interactions in nanoscale systems. The ingredients for the Meir-Wingreen formalism are non-equilibrium Green's functions and self-energies coming from the interactions and the coupling to electrodes, which have been discussed in the last two chapters. In this chapter we provide a brief derivation of the Meir-Wingreen transport formula, and discuss the current conservation condition and non-equilibrium vibrational populations within the formalism.

5.1 Meir-Wingreen Transport Formalism

5.1.1 Derivation

The system Hamiltonian is the same as our Hamiltonian introduced in the previous Chapter except that the electron-vibration interaction is replaced by a general interaction Hamiltonian H_{int},

$$\begin{aligned}
\mathcal{H} &= H_D + H_{lead} + H_T && (5.1)\\
H_D &= \sum_{i,j} \varepsilon_{i,j} d_i^\dagger d_j + H_{int}(\{d_i^\dagger, d_j\}) && (5.2)\\
H_{lead} &= \sum_{\alpha=L,R} \sum_k \varepsilon_{\alpha k} c_{\alpha k}^\dagger c_{\alpha k} && (5.3)\\
H_T &= \sum_{\alpha=L,R} \sum_k \sum_i \left[V_{\alpha k,i} c_{\alpha k}^\dagger d_i + V_{\alpha k,i}^* d_i^\dagger c_{\alpha k} \right]. && (5.4)
\end{aligned}$$

When I_α is defined as the electron current entering the αth electrode, it can be calculated as

$$\begin{aligned}
I_\alpha &= e \left\langle \frac{d}{dt} N_\alpha \right\rangle = \frac{ie}{\hbar} \langle [\mathcal{H}, N_\alpha] \rangle && (5.5)\\
&= -\frac{ie}{\hbar} \sum_{k,n} \left[V_{k\alpha,n} \langle c_{k\alpha}^\dagger d_n \rangle - V_{k\alpha,n}^* \langle d_n^\dagger c_{k\alpha} \rangle \right] && (5.6)
\end{aligned}$$

where $N_\alpha = \sum_k c_{k\alpha}^\dagger c_{k\alpha}$, and k is a set of quantum numbers for the electrode electron, including the spin quantum number $\sigma = \uparrow, \downarrow$.

When we define the following contour-ordered Green's functions

$$\begin{aligned}
G_{n,k\alpha}(\tau, \tau') &= -\frac{1}{i\hbar} \left\langle \mathcal{T}_c d_n(\tau) c_{k\alpha}^\dagger(\tau') \right\rangle && (5.7)\\
G_{k\alpha,n}(\tau, \tau') &= -\frac{1}{i\hbar} \left\langle \mathcal{T}_c c_{k\alpha}(\tau) d_n^\dagger(\tau') \right\rangle, && (5.8)
\end{aligned}$$

one can notice that

$$G^{<}_{n,k\alpha}(t,t) = \frac{i}{\hbar}\langle c^{\dagger}_{k\alpha}(t)d_n(t)\rangle \tag{5.9}$$

$$G^{<}_{k\alpha,n}(t,t) = \frac{i}{\hbar}\langle d^{\dagger}_{n}(t)c_{k\alpha}(t)\rangle. \tag{5.10}$$

Thus, the current expression becomes

$$I_\alpha = -e\sum_{k,n}\left[V_{k\alpha,n}G^{<}_{n,k\alpha}(t,t) - V^{*}_{k\alpha,n}G^{<}_{k\alpha,n}(t,t)\right] \tag{5.11}$$

$$= -\frac{e}{\hbar}\int_{-\infty}^{\infty}\frac{d\varepsilon}{2\pi}\sum_{k,n}\left[V_{k\alpha,n}G^{<}_{n,k\alpha}(\varepsilon) - V^{*}_{k\alpha,n}G^{<}_{k\alpha,n}(\varepsilon)\right]. \tag{5.12}$$

From the Dyson equation or the equation of motion technique [39] one can evaluate $G_{n,k\alpha}(\tau,\tau')$ and $G_{k\alpha,n}(\tau,\tau')$ in terms of full device Green's functions $G_{mn}(\tau,\tau')$ and free electrode Green's functions $g_{k\alpha}(\tau,\tau')$,

$$G_{n,k\alpha}(\tau,\tau') = \sum_m\int_c \tau_1 G_{nm}(\tau,\tau_1)V^{*}_{k\alpha,m}g_{k\alpha}(\tau_1,\tau') \tag{5.13}$$

$$G_{k\alpha,n}(\tau,\tau') = \sum_m\int_c \tau_1 g_{k\alpha}(\tau,\tau_1)V^{*}_{k\alpha,m}G_{mn}(\tau_1,\tau'). \tag{5.14}$$

Using Langreth's rules and the convolution theorem, the lesser parts of $G_{n,k\alpha}(\tau,\tau')$ and $G_{k\alpha,n}(\tau,\tau')$ are

$$G^{<}_{n,k\alpha}(\varepsilon) = \sum_m V^{*}_{k\alpha,m}\left[G^{r}_{nm}(\varepsilon)g^{<}_{k\alpha}(\varepsilon) + G^{<}_{nm}(\varepsilon)g^{a}_{k\alpha}(\varepsilon)\right] \tag{5.15}$$

$$G^{<}_{k\alpha,n}(\varepsilon) = \sum_m V_{k\alpha,m}\left[g^{r}_{k\alpha}(\varepsilon)G^{<}_{mn}(\varepsilon) + g^{<}_{k\alpha}(\varepsilon)G^{a}_{mn}(\varepsilon)\right] \tag{5.16}$$

Let us insert Eq.(5.15) and (5.16) into Eq.(5.12). Using the relation $G^r - G^a = G^> - G^<$ and the definition of the electrode self-energy that we discussed in the last

chapter, one can find that

$$I_\alpha = \frac{2e}{\hbar}\int_{-\infty}^{\infty}\frac{d\varepsilon}{2\pi}\sum_{m,n}\left[\Sigma^{>}_{\alpha,mn}(\varepsilon)G^{<}_{n}m(\varepsilon) - \Sigma^{<}_{\alpha,mn}(\varepsilon)G^{>}_{nm}(\varepsilon)\right] \tag{5.17}$$

$$= \frac{2e}{\hbar}\int_{-\infty}^{\infty}\frac{d\varepsilon}{2\pi}\mathrm{Tr}\left[\Sigma^{>}_{\alpha}(\varepsilon)G^{<}(\varepsilon) - \Sigma^{<}_{\alpha}(\varepsilon)G^{>}(\varepsilon)\right], \tag{5.18}$$

where $\Sigma^{<,>}_{\alpha}$ are the lesser and greater αth electrode self-energies. The factor 2 accounts for the spin degree of freedom. This is the *Meir-Wingreen* transport formula [65].

This formula is readily applied to the energy current carried by the conducting electrons. The power transferred into the αth electrode P_α is

$$P_\alpha = \left\langle \frac{d}{dt}H_\alpha \right\rangle = \frac{2}{\hbar}\int_{-\infty}^{\infty}\frac{d\varepsilon}{2\pi}\varepsilon\mathrm{Tr}\left[\Sigma^{>}_{\alpha}(\varepsilon)G^{<}(\varepsilon) - \Sigma^{<}_{\alpha}(\varepsilon)G^{>}(\varepsilon)\right]. \tag{5.19}$$

5.1.2 Non-interacting Case

As a sanity check one can apply Eq. (5.18) to the case where there is no interaction in the device region, $H_{int} = 0$. The Dyson and Keldysh equations read

$$G^r_0(\varepsilon) = \left[\varepsilon + i0^+ - H_D - \Sigma^r_L(\varepsilon) - \Sigma^r_R(\varepsilon)\right]^{-1} \tag{5.20}$$

$$G^{>,<}_0(\varepsilon) = G^r_0(\varepsilon)\left[\Sigma^{>,<}_L + \Sigma^{>,<}_R\right]G^a_0(\varepsilon), \tag{5.21}$$

where the subscript 0 indicates the non-interacting system. Recalling that

$$\Sigma^{<}_{L,R}(\varepsilon) = in_F\left(\varepsilon - \mu_{L,R}\right)\Gamma_{L,R}(\varepsilon) \tag{5.22}$$

$$\Sigma^{>}_{L,R}(\varepsilon) = i\left[n_F\left(\varepsilon - \mu_{L,R}\right) - 1\right]\Gamma_{L,R}(\varepsilon), \tag{5.23}$$

the non-interacting current is straightforward calculated as

$$I_\alpha = \frac{2e}{\hbar}\int_{-\infty}^{\infty}\frac{d\varepsilon}{2\pi}\mathrm{Tr}\left[\Sigma^{>}_{\alpha}(\varepsilon)G^{<}(\varepsilon) - \Sigma^{<}_{\alpha}(\varepsilon)G^{>}(\varepsilon)\right] \tag{5.24}$$

$$= \frac{2e}{\hbar}\int_{-\infty}^{\infty}\frac{d\varepsilon}{2\pi}\mathrm{Tr}\left[\Gamma_L G^r_0\Gamma_R G^a_0\right](\varepsilon)\left[n_F(\varepsilon - \mu_L) - n_F(\varepsilon - \mu_R)\right]. \tag{5.25}$$

The transmission probability function $T(\varepsilon) = \mathrm{Tr}\left[\Gamma_L G_0^r \Gamma_R G_0^a\right](\varepsilon)$ is known as the *Fisher-Lee* relation [26]. For simplicity let us consider a very small bias regime $eV = \mu_L - \mu_R \ll 1$ at zero temperature. If we assume that the transmission probability function $T(\varepsilon)$ is almost constant at the energy range between $\mu_L = \mu + eV/2$ and $\mu_R = \mu - eV/2$, the current might be approximated as $I(V) \approx \frac{2e}{h} T(\mu) eV$. Therefore the zero-bias conductance is

$$\mathcal{G} = \frac{\partial I(V)}{\partial V} = \frac{2e^2}{h} T(\mu) \tag{5.26}$$

The Meir-Wingreen transport formula recovers the Landauer-Büttiker one for the non-interacting case.

5.1.3 Current Conservation

As we pointed out in the last chapter, the approximation adopted for the interacting self-energy calculation should satisfy the current conservation. Here we want to find out an explicit condition that the approximated self-energy should satisfy for the current conservation from the Meir-Wingreen formula. The current conservation is stated as $I_L = -I_R$ in our definition of the current. Let us calculate

$$I_L + I_R = \sum_{\alpha=L,R} \frac{2e}{\hbar} \int_{-\infty}^{\infty} \frac{d\varepsilon}{2\pi} \mathrm{Tr}\left[\Sigma_\alpha^>(\varepsilon) G^<(\varepsilon) - \Sigma_\alpha^<(\varepsilon) G^>(\varepsilon)\right] \tag{5.27}$$

$$= \frac{2e}{\hbar} \int_{-\infty}^{\infty} \frac{d\varepsilon}{2\pi} \mathrm{Tr}\left[\left(\Sigma_{tot}^> - \Sigma_{int}^>\right) G^<(\varepsilon) - \left(\Sigma_{tot}^< - \Sigma_{int}^<\right) G^>(\varepsilon)\right], \tag{5.28}$$

where $\Sigma_{tot}^{>,<} \equiv \Sigma_L^{>,<} + \Sigma_R^{>,<} + \Sigma_{int}^{>,<}$. Here we claim that

$$\mathrm{Tr}\left[\Sigma_{tot}^>(\varepsilon) G^<(\varepsilon) - \Sigma_{tot}^<(\varepsilon) G^>(\varepsilon)\right] = 0 \tag{5.29}$$

for any energy ε. In order to prove this cancellation, one can use the Keldysh equation

$$G^{>,<}(\varepsilon) = G^r(\varepsilon) \Sigma^{>,<} G^a(\varepsilon), \tag{5.30}$$

and the following relation

$$(G^a)^{-1} - (G^r)^{-1} = (G^r)^{-1}(G^> - G^<)(G^a)^{-1} = \Sigma^>_{tot} - \Sigma^<_{tot}. \tag{5.31}$$

The second relation is immediately derived from the fundamental relation $G^r - G^a = G^> - G^<$. With these relations one can show as follows:

$$\begin{aligned}
\mathrm{Tr}\left[\Sigma^>_{tot}G^< - \Sigma^<_{tot}G^>\right] &= \mathrm{Tr}\left[\Sigma^>_{tot}G^r\Sigma^<_{tot}G^a - \Sigma^<_{tot}G^r\Sigma^>_{tot}G^a\right] && (5.32)\\
&= \mathrm{Tr}\left[\left(\Sigma^<_{tot} + (G^a)^{-1} - (G^r)^{-1}\right)G^r\Sigma^<_{tot}G^a\right. \\
&\quad \left. -\Sigma^<_{tot}G^r\left(\Sigma^<_{tot} + (G^a)^{-1} - (G^r)^{-1}\right)G^a\right] && (5.33)\\
&= \mathrm{Tr}\left[\left(G^r - G^a\right)\Sigma^<_{tot} - \Sigma^<_{tot}\left(G^r - G^a\right)\right] = 0, && (5.34)
\end{aligned}$$

where the cyclic property of the trace operation $\mathrm{Tr}\,[AB] = \mathrm{Tr}\,[BA]$ is used. Therefore the current conservation condition is simplified as

$$I_L + I_R = \frac{2e}{\hbar}\int_{-\infty}^{\infty}\frac{d\varepsilon}{2\pi}\mathrm{Tr}\left[-\Sigma^>_{int}G^<(\varepsilon) + \Sigma^<_{int}G^>(\varepsilon)\right] = 0 \tag{5.35}$$

With this explicit condition we can check whether the approximations introduced in the last Chapter satisfy the current conservation.

Current Conservation within the SCBA

Recalling the lesser and greater electron-vibration self-energies in the SCBA

$$\begin{aligned}
\Sigma^<_{vib}(\varepsilon) &= \sum_\lambda \Sigma^<_{vib,\lambda}(\varepsilon) \\
&= \sum_\lambda \mathcal{M}^\lambda\left[N_\lambda G^<(\varepsilon - \hbar\omega_\lambda) + (N_\lambda + 1)\,G^<(\varepsilon + \hbar\omega_\lambda)\right]\mathcal{M}^\lambda && (5.36)\\
\Sigma^>_{vib}(\varepsilon) &= \sum_\lambda \Sigma^>_{vib,\lambda}(\varepsilon) \\
&= \sum_\lambda \mathcal{M}^\lambda\left[N_\lambda G^>(\varepsilon + \hbar\omega_\lambda) + (N_\lambda + 1)\,G^>(\varepsilon - \hbar\omega_\lambda)\right]\mathcal{M}^\lambda, && (5.37)
\end{aligned}$$

the current conservation condition becomes

$$\begin{aligned} I_L + I_R &= \frac{2e}{\hbar}\int_{-\infty}^{\infty}\frac{d\varepsilon}{2\pi}\mathrm{Tr}\left[\mathcal{M}^\lambda\left(N_\lambda G^<(\varepsilon-\hbar\omega_\lambda)+(N_\lambda+1)G^<(\varepsilon+\hbar\omega_\lambda)\right)\mathcal{M}^\lambda G^>(\varepsilon)\right] \\ &\quad -\mathrm{Tr}\left[\mathcal{M}^\lambda\left(N_\lambda G^>(\varepsilon+\hbar\omega_\lambda)+(N_\lambda+1)G^>(\varepsilon-\hbar\omega_\lambda)\right)\mathcal{M}^\lambda G^<(\varepsilon)\right] \quad (5.38) \\ &= 0. \quad (5.39) \end{aligned}$$

One can realize that Eq.(5.38) vanishes by changing the integral variable $\varepsilon \to \varepsilon + \hbar\omega_\lambda$ and using the cyclic property of the trace operation.

Current Conservation within the 1BA

By analogy with the SCBA, the current conservation condition for the first Born approximation is readily written as

$$\begin{aligned} I_L + I_R &= \frac{2e}{\hbar}\int_{-\infty}^{\infty}\frac{d\varepsilon}{2\pi}\mathrm{Tr}\left[\mathcal{M}^\lambda\left(N_\lambda G_0^<(\varepsilon-\hbar\omega_\lambda)+(N_\lambda+1)G_0^<(\varepsilon+\hbar\omega_\lambda)\right)\mathcal{M}^\lambda G_{1BA}^>(\varepsilon)\right] \\ &\quad -\mathrm{Tr}\left[\mathcal{M}^\lambda\left(N_\lambda G_0^>(\varepsilon+\hbar\omega_\lambda)+(N_\lambda+1)G_0^>(\varepsilon-\hbar\omega_\lambda)\right)\mathcal{M}^\lambda G_{1BA}^<(\varepsilon)\right] \quad (5.40) \\ &\neq 0. \quad (5.41) \end{aligned}$$

Since $G_{1BA}^{>,<}(\varepsilon) \neq G_0^{>,<}(\varepsilon)$, Eq.(5.40) is nonzero in general.

Current Conservation within the LOE

Up to the lowest order of $\mathcal{M}^\lambda$, the current conservation condition turns out to be

$$\begin{aligned} I_L + I_R &\approx I_L^{(0)} + I_R^{(0)} + I_L^{(2)} + I_R^{(2)} \quad (5.42) \\ &= \frac{2e}{\hbar}\int_{-\infty}^{\infty}\frac{d\varepsilon}{2\pi}\mathrm{Tr}\left[-\Sigma_{vib,(2)}^>G_0^<(\varepsilon)+\Sigma_{vib,(2)}^<G_0^>(\varepsilon)\right]. \quad (5.43) \end{aligned}$$

Notice that $I_L^{(0)} + I_R^{(0)} = 0$. Because the lowest-order diagrams are

$$\begin{aligned} \Sigma_{vib,(2)}^<(\varepsilon) &= \sum_\lambda \mathcal{M}^\lambda\left[N_\lambda G_0^<(\varepsilon-\hbar\omega_\lambda)+(N_\lambda+1)\,G_0^<(\varepsilon+\hbar\omega_\lambda)\right]\mathcal{M}^\lambda \quad (5.44) \\ \Sigma_{vib,(2)}^>(\varepsilon) &= \sum_\lambda \mathcal{M}^\lambda\left[N_\lambda G_0^>(\varepsilon+\hbar\omega_\lambda)+(N_\lambda+1)\,G_0^>(\varepsilon-\hbar\omega_\lambda)\right]\mathcal{M}^\lambda, \quad (5.45) \end{aligned}$$

the current conservation rule reads

$$
\begin{aligned}
I_L^{(2)} + I_R^{(2)} &= \frac{2e}{\hbar}\int_{-\infty}^{\infty}\frac{d\varepsilon}{2\pi}\mathrm{Tr}\left[\mathcal{M}^{\lambda}\left(N_\lambda G_0^{<}(\varepsilon-\hbar\omega_\lambda)+(N_\lambda+1)G_0^{<}(\varepsilon+\hbar\omega_\lambda)\right)\mathcal{M}^{\lambda}G_0^{>}(\varepsilon)\right] \\
&\quad -\mathrm{Tr}\left[\mathcal{M}^{\lambda}\left(N_\lambda G_0^{>}(\varepsilon+\hbar\omega_\lambda)+(N_\lambda+1)G_0^{>}(\varepsilon-\hbar\omega_\lambda)\right)\mathcal{M}^{\lambda}G_0^{<}(\varepsilon)\right] \qquad (5.46) \\
&= 0. \qquad (5.47)
\end{aligned}
$$

Thus one can conclude that current is conserved in the lowest-order expansion.

5.2 Non-Equilibrium Vibrational Occupations

One of the most important issues to address is the non-equilibrium vibron population induced by conducting electrons. Vibrational occupation is determined by two competing mechanisms. The first one is an energy exchange with the conducting electrons, via electron-vibration interactions. The electrons can be scattered off by emitting or absorbing molecular vibrational quanta. Whether the conducting electrons heat up or cool down the molecular junction depends on the relative strength between vibrational emission and absorption rates. The second mechanism is the vibration decaying to heat reservoirs. Since the molecule is mechanically connected to bulk electrodes, the locally excited vibraions can decay to bulk phonons. This argument can be formulated in a rate equation for the vibrational occupation N_λ [27],

$$
\begin{aligned}
\frac{d}{dt}N_\lambda &= \frac{P_\lambda}{\hbar\omega_\lambda} - \gamma_\lambda\left(N_\lambda - n_B\left(\hbar\omega_\lambda\right)\right) \qquad (5.48) \\
&= \left(N_\lambda+1\right)E_\lambda - N_\lambda A_\lambda - \gamma_\lambda\left(N_\lambda - n_B\left(\hbar\omega_\lambda\right)\right), \qquad (5.49)
\end{aligned}
$$

where P_λ is the power transferred from electrons to the vibrational mode λ, and γ_λ is a decaying rate of the mode λ by coupling to bulk vibrations. n_B is the Bose-Einstein distribution of the heat reservoir. $\frac{P_\lambda}{\hbar\omega_\lambda}$ is further expressed in terms of emission and absorption rates E_λ and A_λ. $(N_\lambda+1)E_\lambda$ is vibrational excitation by conducting electrons which lose their energy in this emission process. Likewise, $N_\lambda A_\lambda$ describes a

vibrational de-excitation process in which electrons get energies from local vibrations. The third term corresponds to coupling between local vibrations and bulk phonons. This coupling keeps local vibrations equilibrated with heat reservoirs (bulk phonons). Unlike absorption (emission) processes that always decrease (increase) local vibrons, the coupling to heat reservoirs can either decrease or increase the populations, depending on the difference between N_λ and $n_B(\hbar\omega_\lambda)$. If the local vibration is beyond the equilibrium value $n_B(\hbar\omega_\lambda)$, the local vibration is decayed into heat reservoirs. In contrast, if the vibrating molecule is cooled down below the equilibrium occupation $n_B(\hbar\omega_\lambda)$ due to the interactions with electrons, heat reservoirs supply a vibrational energy to local vibrations in order to make the molecule in equilibrium with the Bose-Einstein distribution.

The steady state solution for Eq.(5.48) is immediately obtained as

$$N_\lambda = \frac{n_B\left(\hbar\omega_\lambda\right)\gamma_\lambda + E_\lambda}{A_\lambda + \gamma_\lambda - E_\lambda}. \tag{5.50}$$

Note that the steady state solution does not always exist. If $E_\lambda > A_\lambda + \gamma_\lambda$, the solution for Eq.(5.48) is exponentially growing as a function of time, which implies a vibrational instability.

5.2.1 Emission and Absorption Rates

By analogy with current conservation one can consider energy conservation, i.e.

$$P_L + P_R + P_{vib} = P_L + P_R + \sum_\lambda P_\lambda = 0. \tag{5.51}$$

Note that P_α ($\alpha = L, R, vib$) is defined as the power transferred *into* the electrodes or the molecular vibration. Using the relation Eq.(5.29) one can find that

$$P_\lambda = \frac{2}{\hbar}\int_{-\infty}^{\infty}\frac{d\varepsilon}{2\pi}\varepsilon \mathrm{Tr}\left[\Sigma^{>}_{vib,\lambda}G^{<}(\varepsilon) - \Sigma^{<}_{vib,\lambda}G^{>}(\varepsilon)\right], \tag{5.52}$$

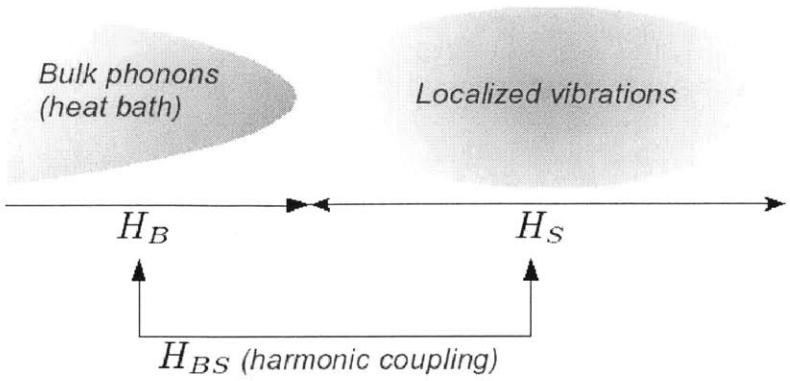

Figure 5-1: Local vibrations coupled to bulk phonons (heat bath).

In the SCBA scheme, using Eq.(5.36) and (5.37), it can be re-expressed as

$$\begin{aligned}\frac{P_\lambda}{\hbar\omega_\lambda} &= (N_\lambda+1)\frac{2}{\hbar}\int_{-\infty}^{\infty}\frac{d\varepsilon}{2\pi}\mathrm{Tr}\left[\mathcal{M}^\lambda G^<(\varepsilon+\hbar\omega_\lambda)\mathcal{M}^\lambda G^>(\varepsilon)\right] \\ &\quad -N_\lambda\frac{2}{\hbar}\int_{-\infty}^{\infty}\frac{d\varepsilon}{2\pi}\mathrm{Tr}\left[\mathcal{M}^\lambda G^<(\varepsilon-\hbar\omega_\lambda)\mathcal{M}^\lambda G^>(\varepsilon)\right]. \qquad (5.53)\end{aligned}$$

The emission and absorption rates for mode λ are identified as

$$E_\lambda^{SCBA} = \frac{2}{\hbar}\int_{-\infty}^{\infty}\frac{d\varepsilon}{2\pi}\mathrm{Tr}\left[\mathcal{M}^\lambda G^<(\varepsilon+\hbar\omega_\lambda)\mathcal{M}^\lambda G^>(\varepsilon)\right] \qquad (5.54)$$

$$A_\lambda^{SCBA} = \frac{2}{\hbar}\int_{-\infty}^{\infty}\frac{d\varepsilon}{2\pi}\mathrm{Tr}\left[\mathcal{M}^\lambda G^<(\varepsilon-\hbar\omega_\lambda)\mathcal{M}^\lambda G^>(\varepsilon)\right]. \qquad (5.55)$$

In the lowest-order expansion, $G^{>,<}$ is replaced by $G_0^{>,<}$:

$$E_{\lambda,(2)} = \frac{2}{\hbar}\int_{-\infty}^{\infty}\frac{d\varepsilon}{2\pi}\mathrm{Tr}\left[\mathcal{M}^\lambda G_0^<(\varepsilon+\hbar\omega_\lambda)\mathcal{M}^\lambda G_0^>(\varepsilon)\right] \qquad (5.56)$$

$$A_{\lambda,(2)} = \frac{2}{\hbar}\int_{-\infty}^{\infty}\frac{d\varepsilon}{2\pi}\mathrm{Tr}\left[\mathcal{M}^\lambda G_0^<(\varepsilon-\hbar\omega_\lambda)\mathcal{M}^\lambda G_0^>(\varepsilon)\right]. \qquad (5.57)$$

5.2.2 Vibrational Decay Rates

In order to obtain vibrational decay rates, let us consider a situation where localized vibrations are harmonically coupled to bulk phonons (heat reservoir). Localized

molecular vibrations and bulk phonons are described by collections of harmonic oscillators in the second quantized form:

$$\mathcal{H}_S = \sum_{i=1}^{3n} \hbar\omega_i \left(b_i^\dagger b_i + \frac{1}{2} \right) \tag{5.58}$$

$$\mathcal{H}_B = \sum_k \hbar\bar{\omega}_k \left(c_k^\dagger c_k + \frac{1}{2} \right), \tag{5.59}$$

where $b_i(b_i^\dagger)$ and $c_k(c_k^\dagger)$ are annihilation (creation) operators for localized vibrations and bulk phonons respectively. The molecule consists of n atoms. In this study, it is assumed that local vibrations are harmonically coupled to bulk phonons:

$$\mathcal{H}_C = \sum_{i=1}^{n} \sum_{\alpha=x,y,z} \sum_{j=1}^{N} \sum_{\beta=x,y,z} u_{i\alpha,j\beta} q_{i\alpha} \bar{q}_{j\beta} \tag{5.60}$$

$$= \sum_{i=1}^{n} \sum_{\alpha=x,y,z} \sum_{j=1}^{N} \sum_{\beta=x,y,z} U_{i\alpha,j\beta} Q_{i\alpha} \bar{Q}_{j\beta} \tag{5.61}$$

where $q_{i\alpha}$ is the α-direction Cartesian coordinate of ith atom in the molecule. Similarly $\bar{q}_{j\beta}$ represents the β-direction Cartesian coordinate of jth atom in the bulk electrode. $u_{i\alpha,j\beta}$ is the (harmonic) interatomic force constant between the molecule and the electrode. $U_{i\alpha,j\beta}$, $Q_{i\alpha}$, and $\bar{Q}_{j\beta}$ are mass-renormalized interatomic force constant and coordinates defined as follows:

$$U_{i\alpha,j\beta} \equiv \frac{u_{i\alpha,j\beta}}{\sqrt{m_i}\sqrt{\bar{m}_j}} \tag{5.62}$$

$$Q_{i\alpha} \equiv \sqrt{m_i} q_{i\alpha} \tag{5.63}$$

$$\bar{Q}_{j\beta} \equiv \sqrt{\bar{m}_j} \bar{q}_{j\beta}. \tag{5.64}$$

$$\tag{5.65}$$

One may use the *Fermi golden rule* to calculate harmonic vibrational decay rates. When the ith molecular vibrational state is occupied, the decay rate at which the

vibration decays by exciting bulk phonons is given by

$$\Gamma_{i\to\text{bath}} = \frac{2\pi}{\hbar} \sum_{k\in\text{bath}} |{}_B\langle k|\mathcal{H}_C|i\rangle_S|^2 \, \delta\left(\hbar\bar{\omega}_k - \hbar\omega_i\right), \tag{5.66}$$

where $|i\rangle_S = b_i^\dagger|0\rangle$ and $|k\rangle_B = c_k^\dagger|0\rangle$. Here $|0\rangle$ represents a vacuum state. After some lengthy algebra, Eq.(5.66) can be re-expressed as follows:

$$\Gamma_{i\to\text{bath}} = -\frac{1}{\omega_i}\vec{X}_i^T \text{Im}\Pi^r\left(\omega_i\right)\vec{X}_i, \tag{5.67}$$

where $\vec{X}_i$ is the normal mode vector of the ith local vibration. $\Pi^r(\omega)$ is the retarded *heat bath self-energy*, which is defined as

$$\Pi^r(\omega) = U\frac{1}{(\omega+i\eta)^2 - \mathcal{H}_B}U^\dagger. \tag{5.68}$$

In fact, one can easily notice that the system discussed here is essentially the same as the *lead-conductor-lead* geometry in the electron transport problem. Π^r is the *mechanical* counterpart to the electronic lead self-energy $\Sigma^r(\varepsilon)$. The numerical method to calculate $\Sigma^r(\varepsilon)$ can be directly applied to Π^r calculation. For a detailed derivation, see Appendix A.

Chapter 6

Numerical Implementation

In this chapter we discuss the numerical implementation and technical issues for a non-equilibrium Green's function formulation in combination with DFT. The calculation consists of three parts:

1. The first part is a planewave-based DFT calculation. By solving the Kohn-Sham equation we construct a self-consistent charge density, a self-consistent potential, and an electronic Hamiltonian. Using density-functional perturbation theory the vibrational spectra of a molecule, and the electron-vibration interactions are obtained.

2. The second part constructs maximally localized Wannier functions. As seen in the past Chapters, the Meir-Wingreen transport formula needs an atomic-like localized basis or localized states. Bloch orbitals used in the DFT calculation do not meet this condition. Once the unitary mapping into Wannier functions is constructed, the electronic Hamiltonian and the electron-vibration interactions in the Bloch representation can be transformed into those in the Wannier representation.

3. The last part is to calculate the electrode and the electron-vibration self-energies, and the device Green's functions from the Hamiltonain in the Wannier representation.

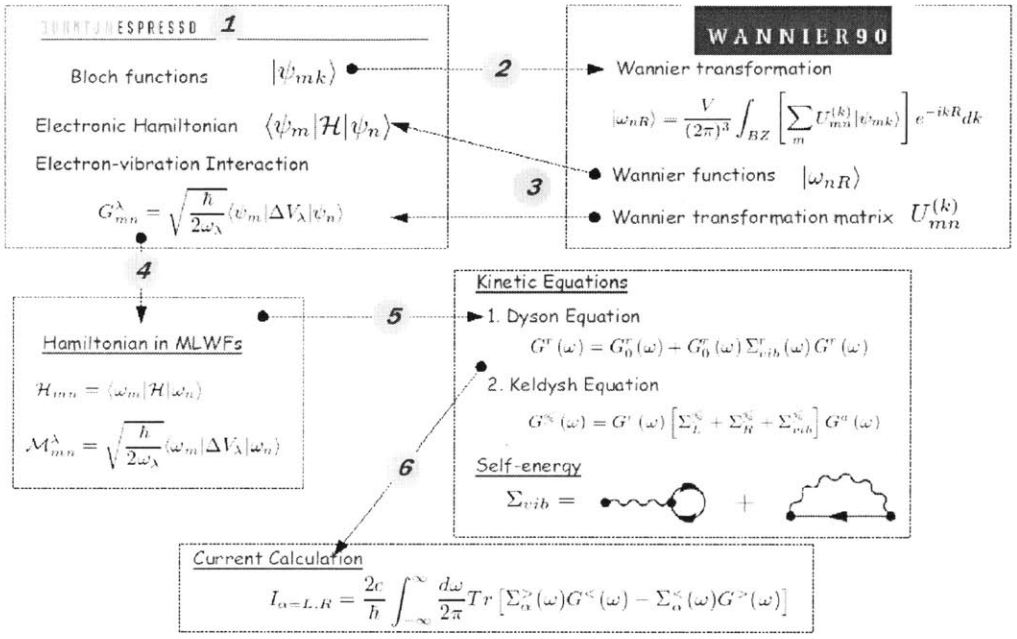

Figure 6-1: Road map for *ab initio* inelastic transport calculation based on Wannier functions.

The first step in performing these calculations is to decide the supercell geometry from which Hamiltonian matrices are extracted. Although the system in theory is composed of the device region containing a vibrating molecule, and two *semi-infinite* electrodes, one has to use a finite size supercell in any practical calculation. We will first discuss how to decide the size of the device region in the supercell. For the electrodes we will introduce the concept of a *principal layer* [55], which is the building block of the semi-infinite electrode.

6.1 System Partitioning

The system Hamiltonian $\mathcal{H}$ for the two-terminal geometry is written as

$$\mathcal{H} = \begin{pmatrix} \mathcal{H}_L & \mathcal{H}_{LC} & 0 \\ \mathcal{H}_{CL} & \mathcal{H}_C & \mathcal{H}_{CR} \\ 0 & \mathcal{H}_{RC} & \mathcal{H}_R \end{pmatrix}, \tag{6.1}$$

where $\mathcal{H}_L$, $\mathcal{H}_R$, and $\mathcal{H}_C$ represent the *non-interacting* Hamiltonian matrices for the left and the right electrode, and the device region. Note that $\mathcal{H}_C$ corresponds to H_0 in Eq. (4.3). $\mathcal{H}_{L(R)C}$ is the coupling matrix between the left (right) electrode and the central region.

6.1.1 Device Region

Note that the device region does not consist of only the conducting molecule. In general the device region is required to be larger than the vibrating molecules by considering the following conditions.

1. The central region needs to be large enough to make a direct coupling between the electrodes zero, $\mathcal{H}_{LR} = \mathcal{H}_{RL} = 0$. This can be achieved by including some surface atoms of the electrodes into the central region and defining them as an *extended molecule*.

2. The electrode Hamiltonian $\mathcal{H}_{L,R}$ is assumed to be the same as the bulk Hamiltonian. If the device region is not sufficiently large, the potential profile of the electrode close to the device region may deviate from the bulk one.

3. For an elastic quantum conductance calculation, the former conditions are sufficient to decide the optimal size of the device region. However, remembering that the Meir-Wingreen formulation assumes that the interaction is confined only in the device region, the electron-vibration coupling matrix should be zero outside the device region. In other words, when $\mathcal{P}_C$ denotes a projection operator onto the device region, $\mathcal{H}_{el-vib} = \mathcal{P}_C \mathcal{H}_{el-vib} \mathcal{P}_C$ should be satisfied.

6.1.2 Principal Layer

In principle left and the right electrodes are semi-infinite, but in a real DFT calculations it is impossible to include a semi-infinite lead in the supercell. However, it turns out that we can model a semi-infinite electrode by using surface Green's function

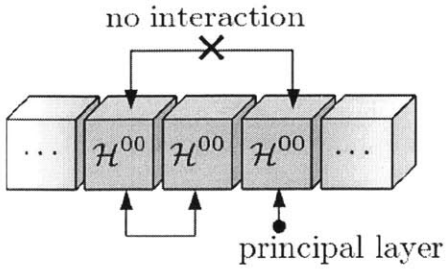

Figure 6-2: An infinite electrode consisting of a repeated array of principal layers. The principal layer interacts only with its nearest neighbor.

techniques. We can have a hint from tight-binding calculations. Recalling the tight-binding model, one can reproduce an entire band structure at any k-point by knowing on-site energies of orbitals and hopping parameters between neighboring orbitals. We can use this idea. For a localized basis $|\omega_m\rangle$ a Hamiltonian matrix $\langle\omega_m|\mathcal{H}|\omega_n\rangle$ converges to zero as the distance between two localized basis functions increases. Based on this localization property of the basis function, one can define a *principal layer* by combining adjacent unit cells in order to satisfy the condition that the principal layer interacts only with the nearest neighboring principal layer. More precisely, when $|\omega_j^i\rangle$ denotes the jth localized orbital in the ith principal layer, $\langle\omega_j^i|\mathcal{H}|\omega_k^{i\pm2}\rangle = 0$ holds for the principal layers. So, the principal layer should be large enough to reproduce the band structure of the electrode accurately. The lead Hamiltonian, which is constructed by translating the principal layer repeatedly, can be written in the form of a tri-digonal block matrix,

$$\mathcal{H}_{lead} = \begin{pmatrix} \ddots & \ddots & 0 & 0 & 0 \\ \ddots & \mathcal{H}^{00} & \mathcal{H}^{01} & 0 & 0 \\ 0 & \mathcal{H}^{01\dagger} & \mathcal{H}^{00} & \mathcal{H}^{01} & 0 \\ 0 & 0 & \mathcal{H}^{01\dagger} & \mathcal{H}^{00} & \ddots \\ 0 & 0 & 0 & \ddots & \ddots \end{pmatrix}. \tag{6.2}$$

Here $\mathcal{H}^{00}$ represents the block matrix between localized functions in the same principal layer, i.e. $\mathcal{H}^{00}_{mn} = \langle\omega_m^i|\mathcal{H}|\omega_n^i\rangle$. $\mathcal{H}^{01}$ ($\mathcal{H}^{01}_{mn} = \langle\omega_m^i|\mathcal{H}|\omega_n^{i+1}\rangle$) is the interaction block

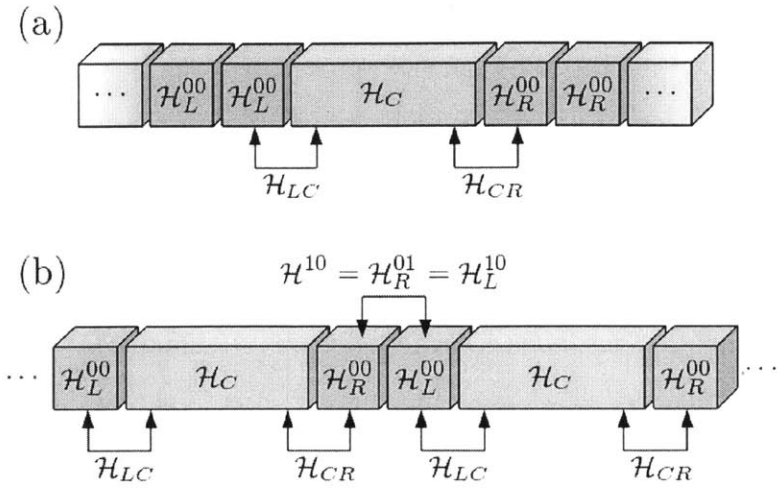

Figure 6-3: (a) Actual two-terminal geometry. The left and right electrodes do not interact with each other. (b) Supercell geometry used in DFT calculation. The principal layers for the left and right electrode interact with each other in a periodic image. This interaction gives $\mathcal{H}^{10} = \mathcal{H}_R^{01} = \mathcal{H}_L^{10}$.

matrix between neighboring principal layers. $\mathcal{H}^{00}$ and $\mathcal{H}^{01}$, corresponding to the on-site energy and the hopping parameter in the simplest tight-binding model, are the *master keys* to enable us to access all the electronic properties of the electrode. The entire system Hamiltonian reads

$$\begin{pmatrix} \mathcal{H}_L & \mathcal{H}_{LC} & 0 \\ \mathcal{H}_{CL} & \mathcal{H}_C & \mathcal{H}_{CR} \\ 0 & \mathcal{H}_{RC} & \mathcal{H}_R \end{pmatrix} = \begin{pmatrix} \ddots & \ddots & 0 & 0 & 0 & 0 & 0 \\ \ddots & \mathcal{H}_L^{00} & \mathcal{H}_L^{10} & 0 & 0 & 0 & 0 \\ 0 & \mathcal{H}_L^{10\dagger} & \mathcal{H}_L^{00} & \mathcal{H}_{LC} & 0 & 0 & 0 \\ 0 & 0 & \mathcal{H}_{CL} & \mathcal{H}_C & \mathcal{H}_{CR} & 0 & 0 \\ 0 & 0 & 0 & \mathcal{H}_{RC} & \mathcal{H}_R^{00} & \mathcal{H}_R^{01} & 0 \\ 0 & 0 & 0 & 0 & \mathcal{H}_R^{01\dagger} & \mathcal{H}_R^{00} & \ddots \\ 0 & 0 & 0 & 0 & 0 & \ddots & \ddots \end{pmatrix}. \quad (6.3)$$

6.1.3 Supercell Calculations

As discussed before, what one needs to obtain are $\mathcal{H}_L^{00}$, $\mathcal{H}_L^{01}$, $\mathcal{H}_{LC}$, $\mathcal{H}_C$, $\mathcal{H}_{CR}$, $\mathcal{H}_R^{00}$, and $\mathcal{H}_R^{01}$. For this purpose one can construct a supercell that is composed of the principal layers for the left and the right electrodes and the device region. Thanks

to the large size of the supercell one can safely use Γ-point sampling. Let us restrict ourselves to considering the case that the left and right electrodes are of the same kind, that is, $\mathcal{H}_L^{00} = \mathcal{H}_R^{00}$. In a real system, principal layers for the left and the right electrodes do not interact with each other because of the long device region. However because we adopt Γ-point sampling with periodic-boundary conditions in the DFT calculation, the principal layers of the left and the right electrodes interact with each other's periodic image. This interaction actually gives $\mathcal{H}_L^{01}$ and $\mathcal{H}_R^{01}$. The Hamiltonian obtained in the supercell calculation is as follows:

$$\mathcal{H}_{supercell} = \begin{pmatrix} \mathcal{H}_L^{00} & \mathcal{H}_{LC} & \mathcal{H}^{01} \\ \mathcal{H}_{CL} & \mathcal{H}_C & \mathcal{H}_{CR} \\ \mathcal{H}^{10} & \mathcal{H}_{RC} & \mathcal{H}_R^{00} \end{pmatrix}, \tag{6.4}$$

where $\mathcal{H}_L^{00} = \mathcal{H}_R^{00}$, $\mathcal{H}^{01} = \mathcal{H}_R^{01\dagger} = \mathcal{H}_L^{10\dagger}$, and $\mathcal{H}^{10} = \mathcal{H}_R^{01} = \mathcal{H}_L^{10}$. One can, therefore, construct all the parts of the entire Hamiltonian Eq.(6.3) from a single Γ-point calculation.

6.2 Hamiltonian in a Wannier Basis

In the Γ-point formalism, the integration over the first Brillouin zone is dropped, so the Wannier transformation becomes a pure matrix multiplication. Let rectangular U^{dis} and square U denote the disentanglement matrix used to extract the maximally-connected subspace from the the entire entangled Bloch space, and the Wannier unitary matrix acting on the maximally-connected subspace respectively. Using these two transformations Wannier orbitals $|\omega_n\rangle$ are obtained from Bloch states $|\psi_i\rangle$:

$$|\omega_n\rangle = \sum_{i,j} U_{in} U_{ji}^{dis} |\psi_j\rangle \tag{6.5}$$

$$= \sum_j \left(U^{dis} U\right)_{jn} |\psi_j\rangle, \tag{6.6}$$

where $|\psi_j\rangle$ is the Bloch state. The electronic Hamiltonian and the electron-vibration interaction can be written in the Wannier representation.

$$\mathcal{H}_e = \sum_{m,n} \mathcal{H}_{mn} c_m^\dagger c_n \tag{6.7}$$

$$\mathcal{H}_{el-vib} = \sum_{\lambda} \sum_{m,n} \mathcal{M}_{mn}^{\lambda} c_m^\dagger c_n \left(b_\lambda^\dagger + b_\lambda \right), \tag{6.8}$$

where

$$\mathcal{H}_{mn} = \langle \omega_m | \mathcal{H}_e | \omega_n \rangle \tag{6.9}$$

$$= \sum_{ij} \left(U^{dis} U \right)_{im}^{*} \langle \psi_i | \mathcal{H}_e | \psi_j \rangle \left(U^{dis} U \right)_{jn} \tag{6.10}$$

$$\mathcal{M}_{mn}^{\lambda} = \sqrt{\frac{\hbar}{2\omega_\lambda}} \langle \omega_m | \Delta V^{\lambda} | \omega_n \rangle \tag{6.11}$$

$$= \sqrt{\frac{\hbar}{2\omega_\lambda}} \sum_{ij} \left(U^{dis} U \right)_{im}^{*} \langle \psi_i | \Delta V^{\lambda} | \psi_j \rangle \left(U^{dis} U \right)_{jn}. \tag{6.12}$$

Here ΔV^{λ} is the derivative of the self-consistent potential with respect to the normal mode λ of the molecular vibration. $c_m(c_m^\dagger)$ is the annihilation (creation) operator for the Wannier function $|\omega_n\rangle$. Similarly $b_\lambda(b_\lambda^\dagger)$ denotes the annihilation (creation) operator for the vibrational mode λ.

6.3 Lead Self-energy

In the theory Chapter we used the eigenstate representation for the electrode to calculate lead self-energies. Instead of diagonalizing the semi-infinite electrode Hamiltonian, we can equivalently compute the lead self-energy by using the lead Hamiltonian in a localized basis representation. Once the system Hamiltonian $\mathcal{H}$ is obtained, the

retarded Green's function for non-interacting electrons is defined as

$$\left[(\varepsilon + i0^+) - \mathcal{H}\right] \begin{pmatrix} \mathcal{G}^r_L & \mathcal{G}^r_{LC} & \mathcal{G}^r_{LR} \\ \mathcal{G}^r_{CL} & \mathcal{G}^r_C & \mathcal{G}^r_{CR} \\ \mathcal{G}^r_{RL} & \mathcal{G}^r_{RC} & \mathcal{G}^r_R \end{pmatrix} = \mathcal{I}, \tag{6.13}$$

where $\mathcal{I}$ is the identity matrix in the Wannier basis. After some algebra, one finds that the non-interacting device Green's function is

$$G^r_0(\varepsilon) = \mathcal{G}^r_C(\varepsilon) = \left[(\varepsilon + i\eta) - \mathcal{H}_C - \Sigma^r_L - \Sigma^r_R\right]^{-1}, \tag{6.14}$$

where

$$\Sigma^r_L = \mathcal{H}_{CL} \frac{1}{(\varepsilon + i0^+) - \mathcal{H}_L} \mathcal{H}_{LC}, \tag{6.15}$$

$$\Sigma^r_R = \mathcal{H}_{CR} \frac{1}{(\varepsilon + i0^+) - \mathcal{H}_R} \mathcal{H}_{RC}. \tag{6.16}$$

Since $\mathcal{H}_{L,R}$ is semi-infinite it is impossible to calculate the lead Green's function $g^r_{L,R}(\varepsilon) = \left[(\varepsilon + i0^+) - \mathcal{H}_{L,R}\right]^{-1}$ directly. Luckily what one has to compute is not $g^r_{L,R}(\varepsilon)$ itself, but its sub-matrix. That is because the localized functions in the device region are coupled only to the finite range of the electrodes close to the conductor, that is, the outmost principal layer. When $\mathcal{P}^L_0$ and $\mathcal{P}^R_0$ denote the projection operators onto the first principal layers of the left and the right leads next to the device region, the coupling matrices with the device region can be re-written as $\mathcal{H}_{LC} = \mathcal{P}^L_0 \mathcal{H}_{LC}$ and $\mathcal{H}_{CR} = \mathcal{H}_{CR} \mathcal{P}^R_0$. Therefore, the electrode self-energies can be expressed as

$$\Sigma^r_L = \mathcal{H}_{CL} \mathcal{P}^L_0 \frac{1}{(\varepsilon + i0^+) - \mathcal{H}_L} \mathcal{P}^L_0 \mathcal{H}_{LC}, \tag{6.17}$$

$$\Sigma^r_R = \mathcal{H}_{CR} \mathcal{P}^R_0 \frac{1}{(\varepsilon + i0^+) - \mathcal{H}_R} \mathcal{P}^R_0 \mathcal{H}_{RC}. \tag{6.18}$$

The sub-matrix $\mathcal{P}^{L,R}_0 \frac{1}{(\varepsilon + i0^+) - \mathcal{H}_{L,R}} \mathcal{P}^{L,R}_0$ is called the surface Green's function. The surface Green's function can be numerically calculated in several ways. In this study we use an efficient and fast iterative method suggested by Sancho et al[83, 84, 85].

In a principal layer representation for the electrode, the lead Green's function $G = [\varepsilon - \mathcal{H}]^{-1}$ satisfies the following equation,

$$\begin{pmatrix} \varepsilon - \mathcal{H}^{00} & -\mathcal{H}^{01} & 0 & \cdots \\ -\mathcal{H}^{01\dagger} & \varepsilon - \mathcal{H}^{00} & -\mathcal{H}^{01} & \cdots \\ 0 & -\mathcal{H}^{01\dagger} & \varepsilon - \mathcal{H}^{00} & \cdots \\ \vdots & \vdots & \vdots & \ddots \end{pmatrix} \begin{pmatrix} G^{00} & G^{01} & G^{02} & \cdots \\ G^{10} & G^{11} & G^{12} & \cdots \\ G^{20} & G^{21} & G^{22} & \cdots \\ \vdots & \vdots & \vdots & \ddots \end{pmatrix} = \mathcal{I}. \tag{6.19}$$

Here the surface Green's function $\mathcal{P}_0 \frac{1}{(\varepsilon + i0^+) - \mathcal{H}} \mathcal{P}_0$ is G^{00}, which will be numerically calculated below. From Eq. (6.19) one can obtain the following relations between the block Green's functions G^{m0},

$$G^{00} = \left[\varepsilon - \mathcal{H}^{00}\right]^{-1} + \tilde{t}_0 G^{10} \tag{6.20}$$

$$G^{m0} = t_0 G^{(m-1)0} + \tilde{t}_0 G^{(m+1)0} \quad m \geq 1, \tag{6.21}$$

where

$$t_0 = \left[\varepsilon - \mathcal{H}^{00}\right]^{-1} \mathcal{H}^{01\dagger} \tag{6.22}$$

$$\tilde{t}_0 = \left[\varepsilon - \mathcal{H}^{00}\right]^{-1} \mathcal{H}^{01}. \tag{6.23}$$

By iterating Eq. (6.21) i times, one can show that

$$G^{n0} = t_i G^{n-2^i,0} + \tilde{t}_i G^{n+2^i,0}, \tag{6.24}$$

where

$$t_i = \left[1 - t_{i-1}\tilde{t}_{i-1} - \tilde{t}_{i-1}t_{i-1}\right]^{-1} t_{i-1}^2 \tag{6.25}$$

$$\tilde{t}_i = \left[1 - t_{i-1}\tilde{t}_{i-1} - \tilde{t}_{i-1}t_{i-1}\right]^{-1} \tilde{t}_{i-1}^2. \tag{6.26}$$

$$\tag{6.27}$$

Using Eq. (6.21) and Eq. (6.24) with $n = 2^i$, one can solve G^{10} recursively in the following manner,

$$\begin{aligned} G^{10} &= t_0 G^{00} + \tilde{t}_0 G^{20} && (6.28)\\ &= (t_0 + \tilde{t}_0 t_1) G^{00} + \tilde{t}_0 \tilde{t}_1 G^{40} && (6.29)\\ &= (t_0 + \tilde{t}_0 t_1 + \cdots + \tilde{t}_0 \cdots \tilde{t}_{i-1} t_i) G^{00} + \prod_{k=0}^{i} \tilde{t}_k G^{2^{i+1},0} && (6.30) \end{aligned}$$

This recursive calculation will be repeated until $\|t_i\|$ and $\left\|\tilde{t}_i\right\|$ are lesser than a certain threshold. In this limit Eq. (6.28) becomes

$$G^{10} = (t_0 + \tilde{t}_0 t_1 + \cdots + \tilde{t}_0 \cdots \tilde{t}_{i-1} t_i) G^{00} \equiv T G^{00}. \tag{6.31}$$

Inserting Eq. (6.31) into Eq. (6.20), one can finally obtain

$$G^{00}(\varepsilon) = \left[\varepsilon - \mathcal{H}^{00} - \mathcal{H}^{01} T\right]^{-1} \tag{6.32}$$

6.4 Green's function and Current Calculations

When system parameters such as the electronic Hamiltonian $\mathcal{H}$, the electron-vibration interaction $\mathcal{H}_{el-vib}$, and the vibrational spectra $\hbar\omega_\lambda$ are computed, the next task is to calculate the full interacting Green's function that enables us to obtain transport properties.

6.4.1 Discretizing Energy Space

For the numerical calculation, Green's functions and self-energies, which are functions of the energy ε, are required to be discretized. The energy grid size should be small enough to capture all the detailed physics. For example, in order to distinguish vibrational spectra ranging from tens to hundreds of meV, the energy grid may be chosen to be less than 1 meV. If the Green's function has a very sharp resonant structure, one has to use an energy grid smaller than the width of the resonant

peak. Furthermore, the thermal smearing in the Fermi-Dirac distribution should be captured properly by using a fine energy mesh. On the other hand, one has to take into account the fact that using too fine energy mesh makes the numerical calculation slower and increases the computational cost. Thus the size of the energy grid should be tuned by considering these two issues.

6.4.2 Self-consistent Calculation

Figure 6-4 summarizes the self-consistent calculation procedure for the Green's functions. As an initial input the non-interacting Green's functions are used.

$$G_0^r(\varepsilon) = \left[(\varepsilon + i0^+) - \mathcal{H}_C - \Sigma_L^r - \Sigma_R^r\right]^{-1} \tag{6.33}$$

$$G_0^<(\varepsilon) = G_0^r(\varepsilon)\left[\Sigma_L^<(\varepsilon) + \Sigma_R^<(\varepsilon)\right] G_0^a(\varepsilon). \tag{6.34}$$

As discussed before, the electron-vibration self-energies are computed at the level of Hartree and Fock diagrams, Eq.(4.46)-(4.48). The Green's functions are updated by using Dyson and Keldysh equations Eq.(4.49) and (4.50). When $\mathcal{O}_n$ is the object calculated in the nth iteration, self-consistency is tested by using the following convergence criterion:

$$||\mathcal{O}_n - \mathcal{O}_{n+1}|| \equiv \sum_i \sum_{jk} |\mathcal{O}_n(\varepsilon_i) - \mathcal{O}_{n+1}(\varepsilon_i)|_{jk} < \Delta_{\text{conv}}, \tag{6.35}$$

where Δ_{conv} is the convergence threshold. If the convergence criterion is not satisfied, the object that will be used in the next iteration is prepared using a linear mixing scheme,

$$(1-\beta)\mathcal{O}_n + \beta\mathcal{O}_{n+1} \rightarrow \mathcal{O}_{n+1}, \tag{6.36}$$

where β is tuned for the better convergence.

For nonequilibrium vibration populations one can add another self-consistent loop to the Green's function calculation loop, as seen in Fig. 6-5. The equilibrium occupation given by Bose-Einstein distribution is used in the very first run. With the mth

nonequilibrium vibration population $N_{\lambda,m}$, one can calculate the Green's function well converged in a self-consistent way. Using Eq.(5.48) the $(m+1)$th vibration population $N_{\lambda,m+1}$ is updated. Until convergence for vibrational occupations is achieved, this nested self-consistent iteration continues. Once well converged Green's functions and nonequilibrium population are ready, then physical observables such as the current and the spectral density of the central region are straightforwardly calculated from the Meir-Wingreen formulation.

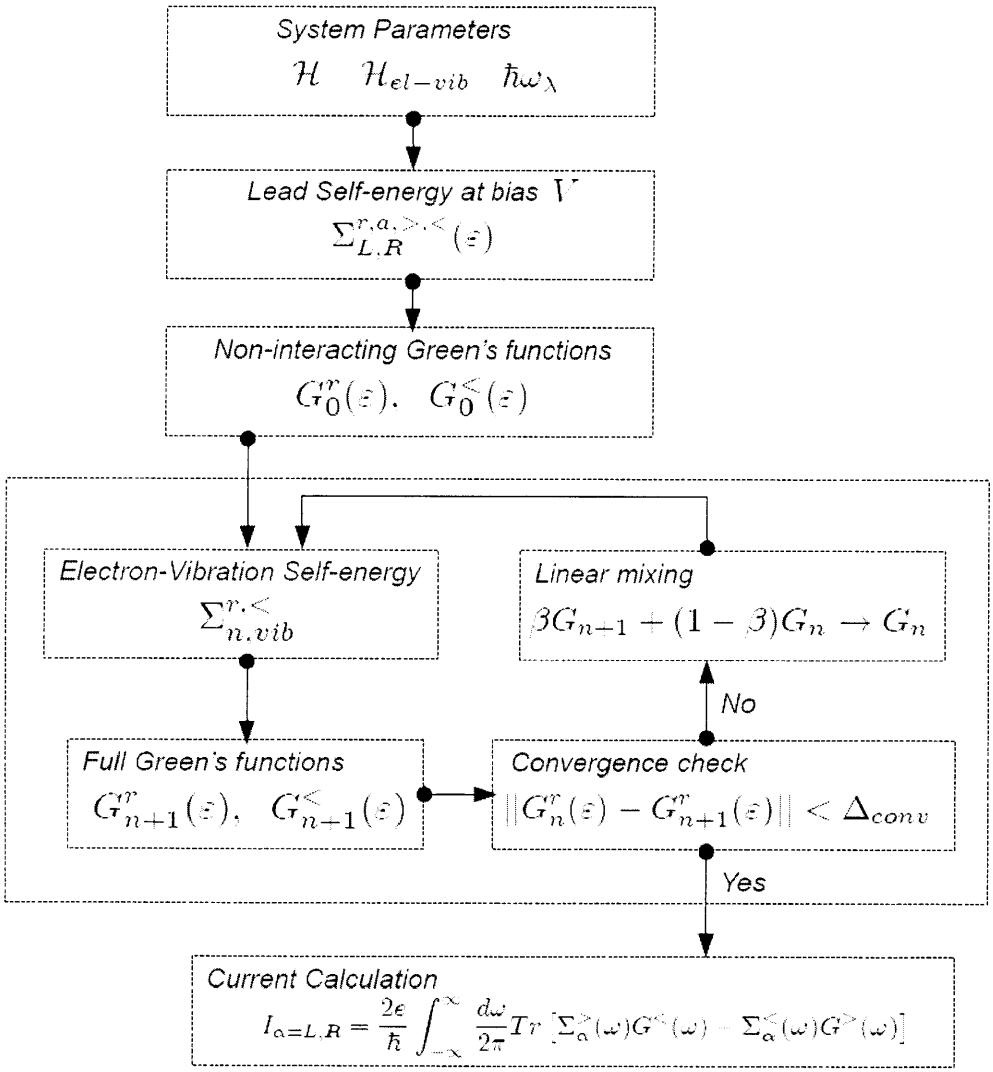

Figure 6-4: Flowchart for SCBA. Here an equilibrium vibrational population is assumed.

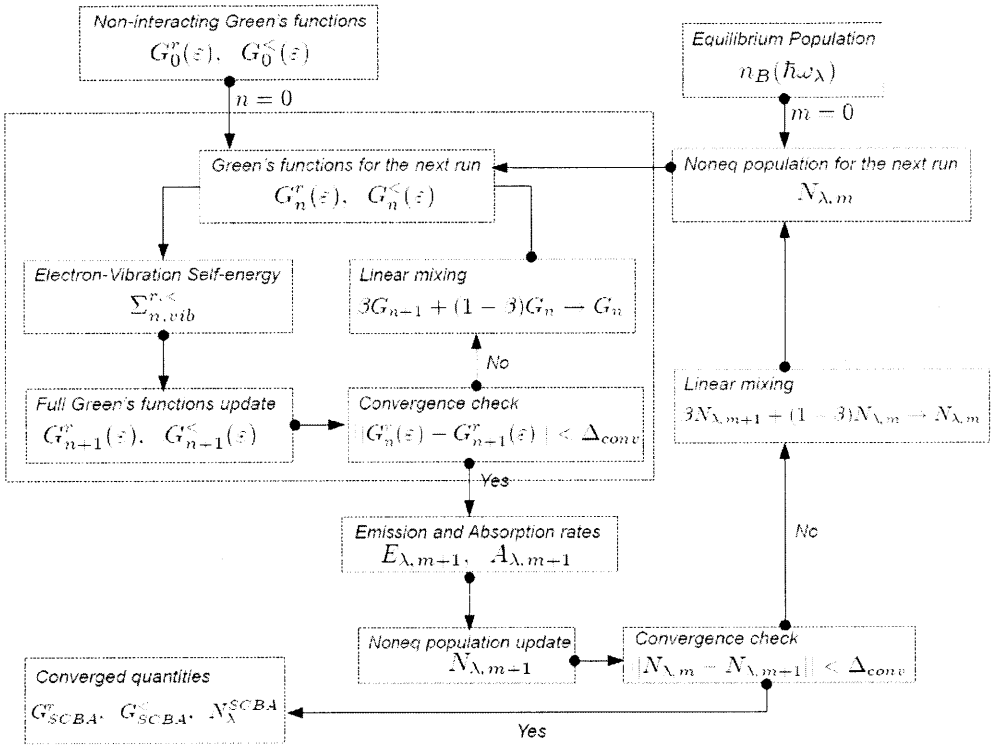

Figure 6-5: Nested self-consistent calculation loop for non-equilibrium vibrational occupation.

Chapter 7

Application: Carbon-based molecular junction

In this Chapter we present two applications of our *ab initio* inelastic transport approach. As a first application we calculate inelastic transport properties of a benzene molecule connected to monoatomic carbon chains (cumulenes). For this benchmark system we apply both the SCBA and the LOPT for equilibrium and non-equilibrium solutions. As a second example we replace cumulene with $(3,3)$ single-wall carbon nanotube (CNT). In this molecular junction we focus on the calculation of realistic decay rates and non-equilibrium vibration populations. Technically, all DFT calculations are performed using the Perdew-Zunger local density approximation[75], norm-conserving pseudopotentials[95], and a plane-wave basis with a cutoff of 55 Ry.

7.1 Cumulene - C_6H_4 - Cumulene

We first study a benzene molecule connected to a monoatomic carbon chain. It is known that cumulene is subject to Peierls distortion: It readily becomes dimerized and opens an energy band gap favored by a lower energy structure. We thus freeze the structure of cumulene and use it as a metallic electrode.

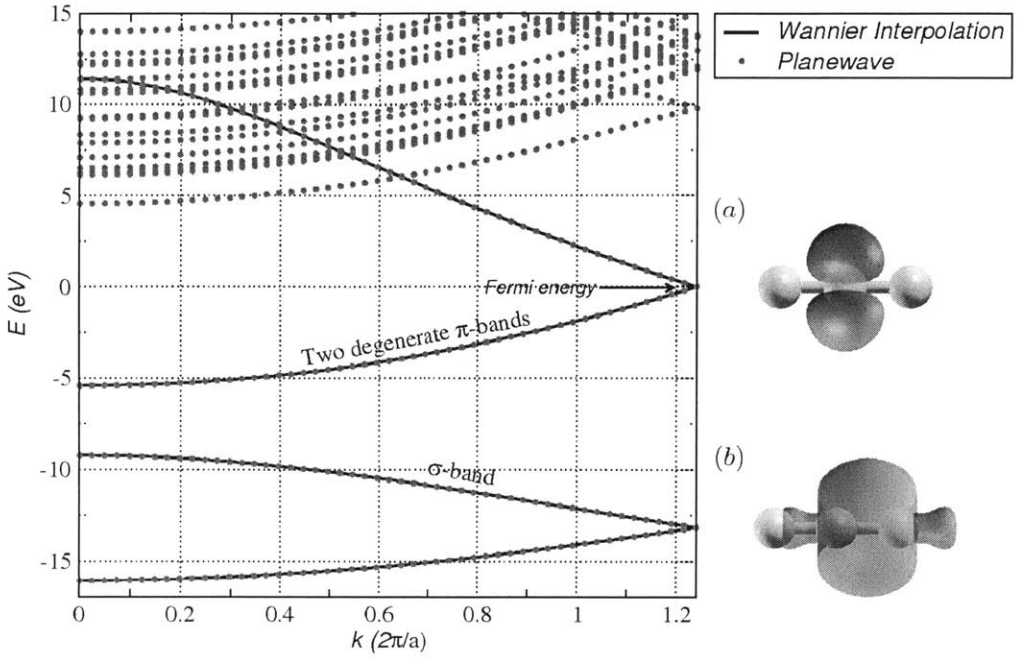

Figure 7-1: Band structure of cumulene for a two-atom unit cell. (Red dots: direct DFT calculation; black solid lines: Wannier interploted bands). (a) p-type Wannier function at an atomic site (b) σ-like Wannier function at a mid-bond site.

7.1.1 System Details

We construct two p-orbitals and one σ-like mid-bond Wannier functions (see Fig. 7-1) for this electrode. The two p-orbitals, p_y and p_z, are perpendicular to the transport direction, which is along the x-axis in our calculation. Figure 7-1 shows the band structure of cumulene. The energy bands are obtained either from a direct planewave-based DFT calculation, or by Wannier band interpolation, and are in excellent agreement. While the lowest energy band originates from σ-orbitals, p-orbitals give rise to doubly degenerate π-bands around the Fermi level, and transport properties at the Fermi energy are characterized by these two π-bands.

Figure 7-2 shows the supercell geometry used in the transport calculations. The benzene molecule alone is allowed to vibrate. The device region, containing the vibrating region and part of the cumulene, is taken to be large enough to make sure that there is no direct coupling between electrodes, and that the electron-vibration coupling is zero outside the device region. For the benzene molecule, p_z-type Wannier

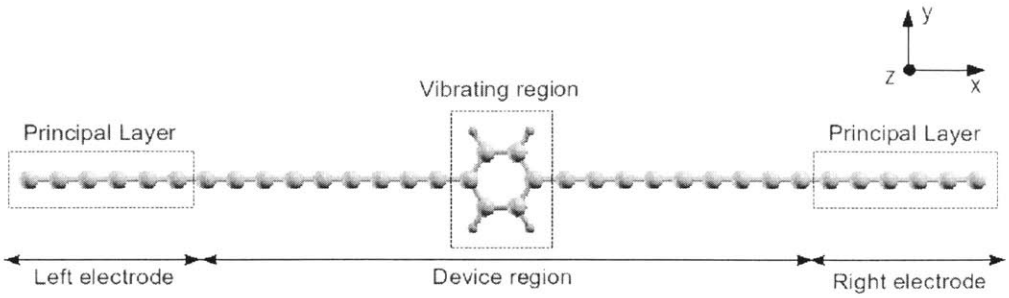

Figure 7-2: The supercell used in the calculation. The coordinate system is indicated in the right top. Only the benzene (C_6H_4) is allowed to vibrate. One principal layer contains six carbon atoms. The device region is taken large enough to make sure that there is no electron-vibration interaction outside the device region.

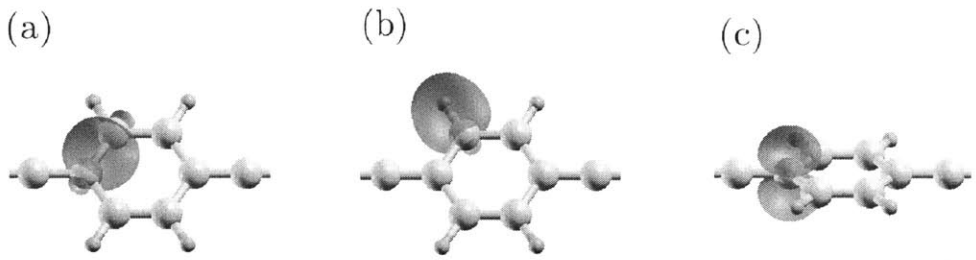

Figure 7-3: Wannier functions of the benzene molecule. (a) σ-like Wannier function between carbon and carbon atoms, (b) σ-bond between carbon and hydrogen atoms , and (c) π orbital at each carbon atomic site.

functions on carbon atoms and σ-like Wannier functions on $C-C$ and $C-H$ bonds are constructed, as illustrated in Fig. 7-3.

7.1.2 Equilibrium Vibrations

The differential conductance $G = dI/dV$ and its derivative dG/dV are calculated using either the SCBA or the LOPT scheme. Temperature is taken to be $k_BT = 1\text{meV}$. As seen in Fig.7-4, these two approximations display essentially perfect agreement. Four conductance changes are observed in the differential conductance curve of Fig. 7-4. The corresponding inelastic transport signals due to electron-vibration interactions appear as peaks in the d^2I/dV^2 plot. The peak position on the bias axis

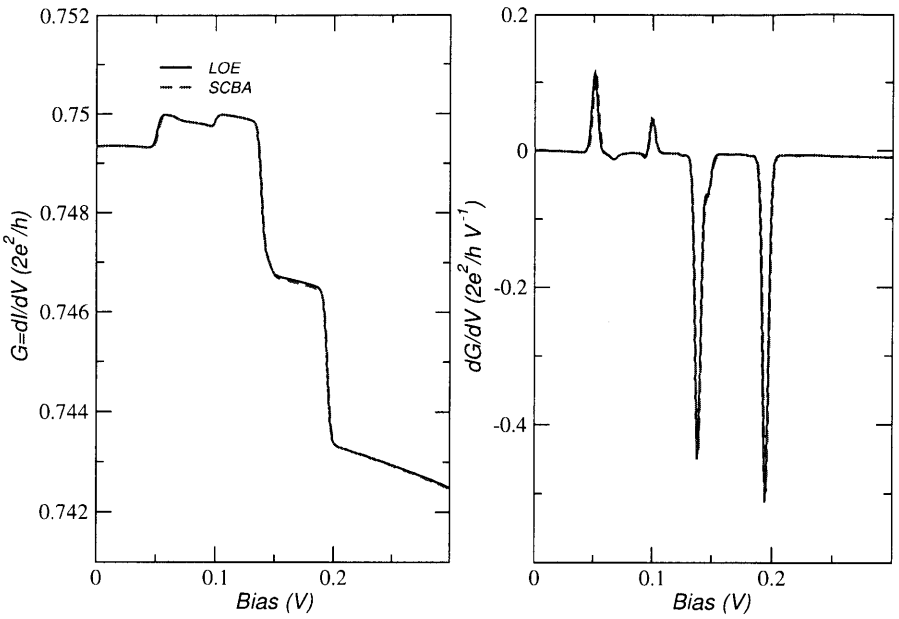

Figure 7-4: Differential conductance $G = dI/dV$ and its derivative dG/dV with equilibrum vibrationl populations calculated using LOPT (black solid line) and SCBA (red dashed line). At lower bias two differential conductance increases are observed. At higher bias, two large conductance drops occur. These conductance changes correspond to peaks in dG/dV.

corresponds to the vibrational energy involved in the electron-vibration scattering events. From four peaks observed in Fig. 7-4 one might conclude that there are four active vibrational modes, but there is a shoulder on the right side of the third peak. This may indicate that there is a fifth active vibrational mode.

To investigate which vibrational modes participate in inelastic transport, we performed *modewise* calculation by keeping only one particular vibrational mode. For clarity the elastic contribution is excluded in the modewise calculation. These calculations show that there are five major peaks in dG/dV (Fig. 7-5). The corresponding vibrational configurations of these five active modes are also shown in Fig. 7-5: While two upward peaks are out-of-plane vibrations, three downward peaks correspond to in-plane motions.

Thus, electron-vibration interactions can lead to both differential conductance rises and drops. This simultaneous occurrence can be understood from scattering

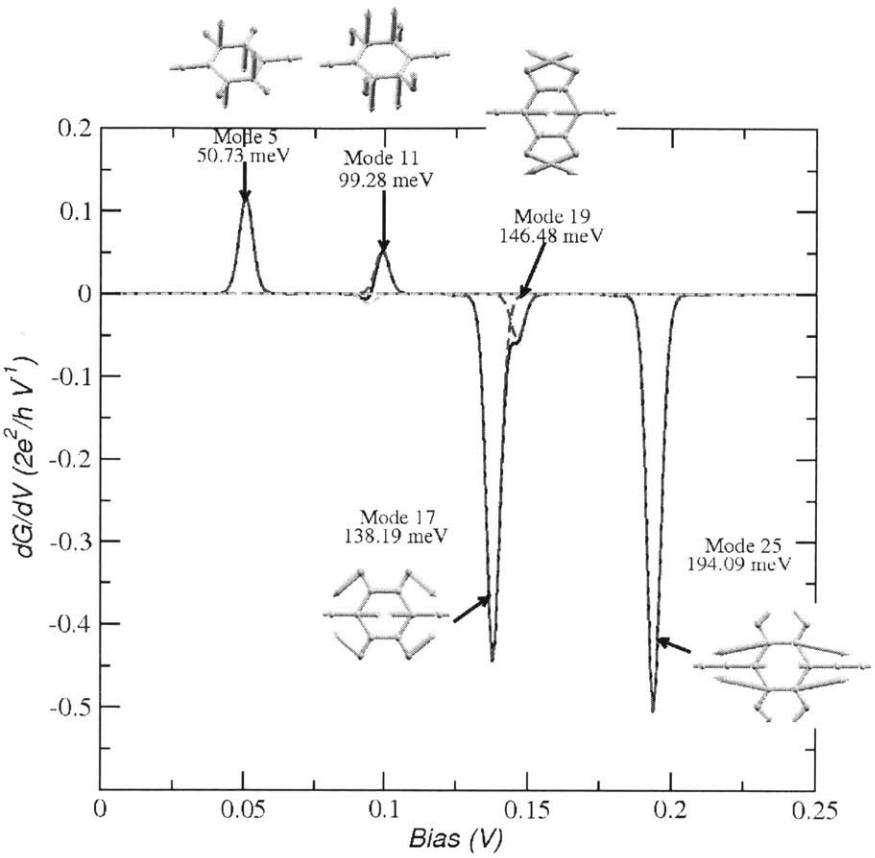

Figure 7-5: dG/dV in modewise calculation. Five active vibrational modes are found. The corresponding vibrational configuration are illustrated. While the first two active modes leading to conductance jumps are out-of-plane motions, the three conductance-drop modes correspond to in-plane vibrations.

theory and transmission eigenchannels[59, 71], following Ref.[38]. As seen in Fig. 7-6, let us consider an electron injected from the left electrode on a left-incident ith eigenchannel $|\Psi_L^i\rangle$ at energy ε. If there is no scattering with molecular vibrations, this electron contributes to elastic conductance

$$G_{no\ el-vib} = G_0 \sum_i \mathcal{T}_{L\to R}^i(\varepsilon), \tag{7.1}$$

where $G_0 = \frac{2e^2}{h}$ and $\mathcal{T}_{L\to R}^i(\varepsilon)$ is the elastic transmission probability of $|\Psi_L^i(\varepsilon)\rangle$. Now let us consider that the electron on a left-incident ith eigenchannel $|\Psi_L^i(\varepsilon)\rangle$ is scattered

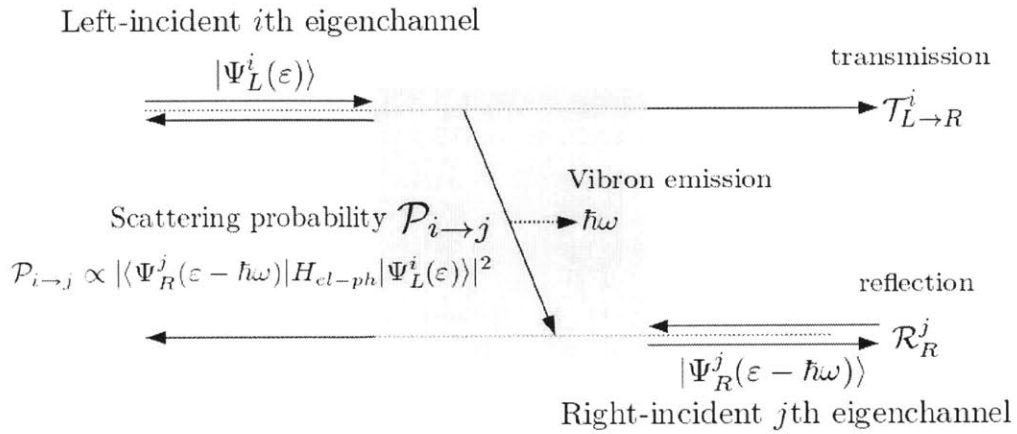

Figure 7-6: Schematic representation of inelastic scattering in the presence of electron-vibration interactions. Solid arrows indicate transmission eigenchannels.

off to a right-incident jth eigenchannel $|\Psi_R^j(\varepsilon-\hbar\omega)\rangle$ by emitting a vibrational quanta $\hbar\omega$. The outgoing state of $|\Psi_R^j(\varepsilon-\hbar\omega)\rangle$ can go either to the left electrode or to the right one. Since conductance measured in the right lead is considered here, the probability to move back to the right electrode for $|\Psi_R^j(\varepsilon-\hbar\omega)\rangle$ is given by its reflection probability $\mathcal{R}_R^j(\varepsilon-\hbar\omega)$. If $\mathcal{P}_{i\to j}$ denotes a probability that $|\Psi_L^i(\varepsilon)\rangle$ is scattered to $|\Psi_R^j(\varepsilon-\hbar\omega)\rangle$, then the total conductance can be computed as:

$$\begin{aligned} G_{el-vib} &= G_0 \left[\sum_i \left(1 - \sum_j \mathcal{P}_{i\to j} \right) \mathcal{T}_{L\to R}^i(\varepsilon) \right. \\ &\quad \left. + \sum_{i,j} \mathcal{P}_{i\to j} \mathcal{R}_R^j((\varepsilon) - \hbar\omega) \right]. \end{aligned} \tag{7.2}$$

Thus, the conductance change is given by

$$\begin{aligned} \Delta G &= G_{el-vib} - G_{no\ el-vib} \\ &= \sum_i G_0 \left[\sum_j \mathcal{P}_{i\to j} \left(\mathcal{R}_R^j(\varepsilon-\hbar\omega) - \mathcal{T}_{L\to R}^i(\varepsilon) \right) \right] \qquad (7.3) \\ &\approx \sum_i G_0 \left[\sum_j \mathcal{P}_{i\to j} \left(\mathcal{R}_R^j(\varepsilon_F) - \mathcal{T}_{L\to R}^i(\varepsilon_F) \right) \right]. \qquad (7.4) \end{aligned}$$

Let us examine these relations in detail. First, transmission and reflection probabili-

(a) Major channel: $|\Psi_1\rangle$

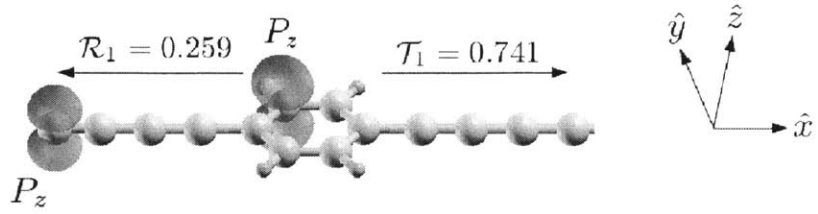

(b) Minor channel: $|\Psi_2\rangle$

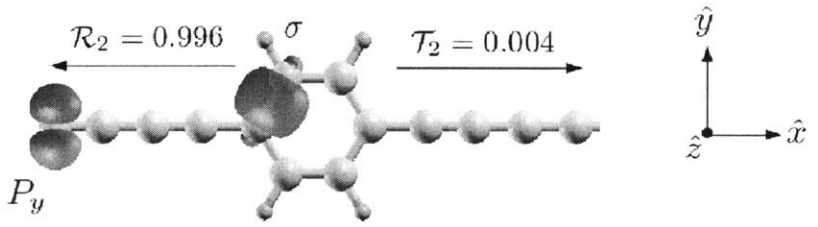

Figure 7-7: Cumulene-benzene-cumulene system has two transmission eigenchannels. The major channel consists of p_y orbitals on the cumulene electrodes and the benzene molecule. p_y on the cumulene leads and σ bonds on the benzene constitute the minor eigenchannel.

ties are approximated by those at Fermi energy ε_F (Since vibrational energies are generally small, one might expect that transmission and reflection probabilities would not change significantly over $[\varepsilon_F - \hbar\omega, \varepsilon_F + \hbar\omega]$). Now, note that conductance can increase or decrease depending on the relative magnitude of $\mathcal{P}_{i\to j}\left(\mathcal{R}^j_R(\varepsilon_F) - \mathcal{T}^i_{L\to R}(\varepsilon_F)\right)$. , and that while $\left(\mathcal{R}^j_R(\varepsilon_F) - \mathcal{T}^i_{L\to R}(\varepsilon_F)\right)$ does not depend on a vibrational configuration, $\mathcal{P}_{i\to j} \propto \left|\langle\Psi^j_R|\mathcal{H}^\lambda_{el-vib}|\Psi^i_L\rangle\right|^2$, which can be calculated from Fermi golden rule[60, 66], is determined by the electron-vibration interaction matrix.

For the cumulene-benzene-cumulene system, it is found that there are two transmission eigenchannels: the major transmission channel $|\Psi^1_{L,R}\rangle$ with $\mathcal{T}^1_{L\to R} = \mathcal{T}^1_{R\to L} = 0.741$ and the minor channel $|\Psi^2_{L,R}\rangle$ with $\mathcal{T}^2_{L\to R} = \mathcal{T}^2_{R\to L} = 0.004$. p_z orbitals on the cumulene wire and the benzene molecule constitute the major transmission eigenchannel $|\Psi^1_{L,R}\rangle$. p_y orbitals on the cumulene wire and σ bonds of the benzene molecule contribute to the minor transmission channel $|\Psi^2_{L,R}\rangle$. In addition, while $|\Psi^1_{L,R}\rangle$ is

symmetric with respect to the zx-plane, $|\Psi^2_{L,R}\rangle$ is anti-symmetric. In other words, when $\hat{P}_{zx}$ denotes the reflection operator with respect to zx-plane, $\hat{P}_{zx}|\Psi^1_{L,R}\rangle = |\Psi^1_{L,R}\rangle$ and $\hat{P}_{zx}|\Psi^2_{L,R}\rangle = -|\Psi^2_{L,R}\rangle$ hold.

The first two active vibrational modes $\lambda = 5, 11$, shown in Fig. 7-5, which lead to differential conductance jumps, show anti-symmetric vibrational motion with respect to the zx-plane. Then, the corresponding electron-vibration interactions $\mathcal{H}^{\lambda=5,11}_{el-vib}$ satisfy

$$\mathcal{H}^{\lambda=5,11}_{el-vib} = -\hat{P}_{zx}\mathcal{H}^{\lambda=5,11}_{el-vib}\hat{P}_{zx}. \tag{7.5}$$

Because of these reflection symmetries,

$$\langle\Psi^1_R|\mathcal{H}^{\lambda=5,11}_{el-vib}|\Psi^1_L\rangle = \langle\Psi^2_R|\mathcal{H}^{\lambda=5,11}_{el-vib}|\Psi^2_L\rangle = 0, \tag{7.6}$$

i.e. scattering from $|\Psi^{1(2)}_L\rangle$ to $|\Psi^{1(2)}_R\rangle$ is prohibited. Since $(\mathcal{R}^2_R - \mathcal{T}^1_{L\to R}) = (\mathcal{R}^1_R - \mathcal{T}^2_{L\to R}) = 0.255$, one obtains a differential conductance rise

$$\begin{aligned}\Delta G &= G_0\Big[\mathcal{P}^{\lambda=5,11}_{1\to 2}(\mathcal{R}^2_R - \mathcal{T}^1_{L\to R}) \\ &\quad +\mathcal{P}^{\lambda=5,11}_{2\to 1}(\mathcal{R}^1_R - \mathcal{T}^2_{L\to R})\Big] > 0.\end{aligned} \tag{7.7}$$

In contrast, the last three active modes $\lambda = 17, 19$ and 25 are symmetric with respect to the zx-plane:

$$\mathcal{H}^{\lambda=17,19.25}_{el-vib} = \hat{P}_{zx}\mathcal{H}^{\lambda=17,19,25}_{el-vib}\hat{P}_{zx}. \tag{7.8}$$

Therefore, one has these reflection selection rules:

$$\langle\Psi^1_R|\mathcal{H}^{\lambda=17,19,25}_{el-vib}|\Psi^2_L\rangle = \langle\Psi^2_R|\mathcal{H}^{\lambda=17,19,25}_{el-vib}|\Psi^1_L\rangle = 0. \tag{7.9}$$

Since $\mathcal{P}^{\lambda=17,19,25}_{1\to 1} \gg \mathcal{P}^{\lambda=17,19,25}_{2\to 2}$ from numerical calculation, then one finds the three differential conductance drops

$$\begin{aligned}\Delta G &= G_0\Big[\mathcal{P}^{\lambda=17,19,25}_{1\to 1}(\mathcal{R}^1_R - \mathcal{T}^1_{L\to R}) \\ &\quad +\mathcal{P}^{\lambda=17,19,25}_{2\to 2}(\mathcal{R}^2_R - \mathcal{T}^2_{L\to R})\Big] < 0,\end{aligned} \tag{7.10}$$

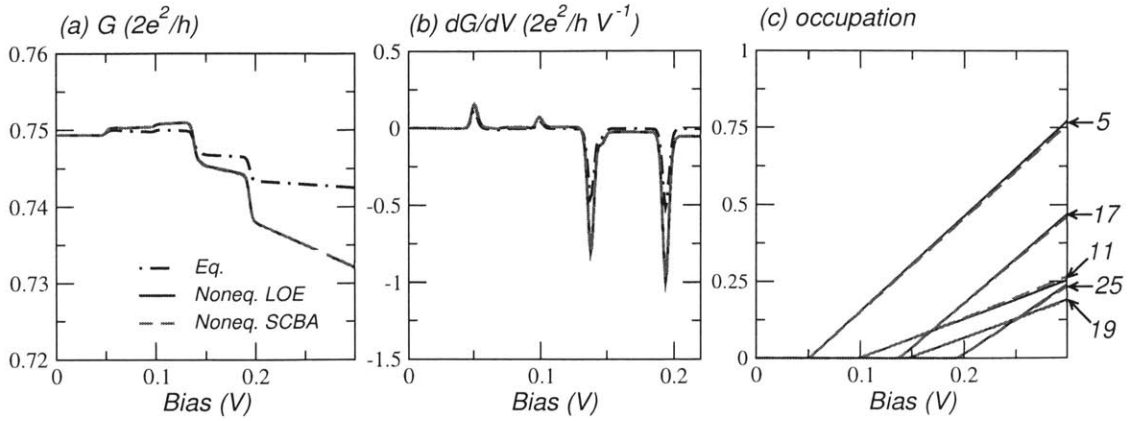

Figure 7-8: Inelastic transport calculations with nonequilibrium vibrational populations (blue solid line: LOPT; red dashed line: SCBA; black dot-dashed line: equilibrium case). (a) differential conductance, (b) second derivative of the current, and (c) vibration populations..

where $(\mathcal{R}_R^1 - \mathcal{T}_{L\to R}^1) = -0.482$ and $(\mathcal{R}_R^2 - \mathcal{T}_{L\to R}^2) = 0.992$. More generally this multi-channel analysis shows that differential conductance rises and drops can occur at the same time.

7.1.3 Non-Equilibrium Vibrations

Next, let us take into account the effect of nonequilibrium vibrational populations on transport properties. This situation corresponds to the case where the decay rate of a molecular vibration to its surrounding is larger than the emission rate due to electron-vibration scattering. In order to compare equilibrium and nonequilibrium vibration cases the decay rate $\hbar\gamma_\lambda = 0.1$ meV is chosen for all vibrational modes; This condition will be relaxed in the next example.

As shown in Fig. 7-8 (a), nonequilibrium effects lead to larger slopes in comparison with the equilibrium case. Furthermore, the differential conductance change increases at the threshold bias voltage. These two changes appear as (1) the finite dG/dV value between peaks and (2) increased peak heights in Fig. 7-8 (b). When the bias exceeds the threshold voltage equal to the vibrational energy, the vibrational population starts to increase as observed in Fig. 7-8 (c). This is because of the increase in phase

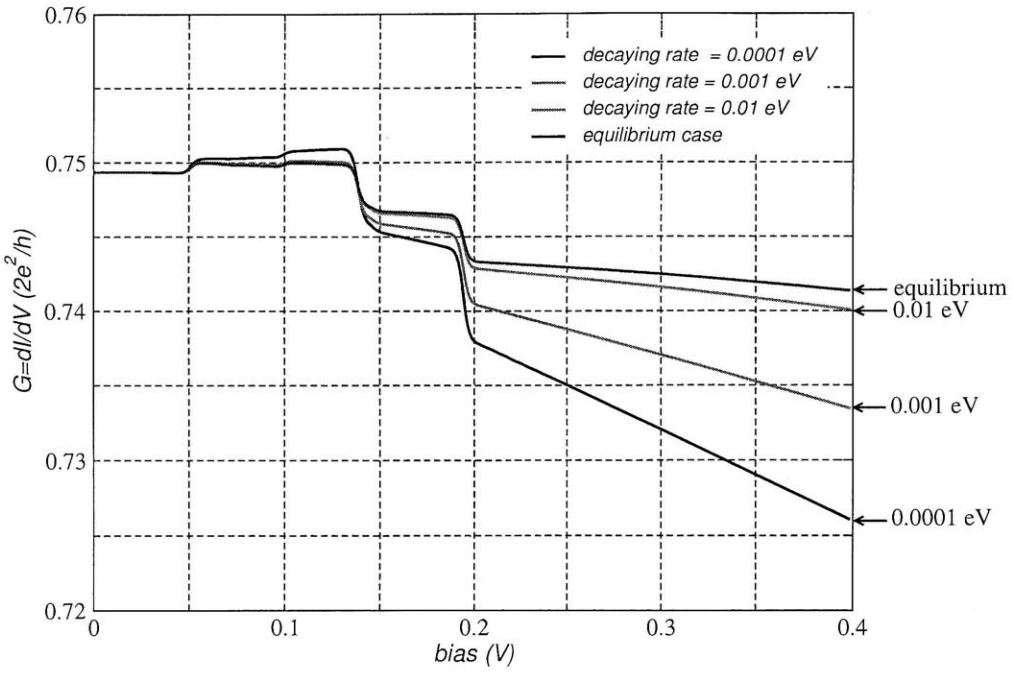

Figure 7-9: Differential conductance for different decay rates (black solid line: $\hbar\gamma_\lambda = 0.1$ meV; red solid line: $\hbar\gamma_\lambda = 1$ meV; green solid line: $\hbar\gamma_\lambda = 10$ meV; blue solid line: equilibrium case ($\hbar\gamma_\lambda \to \infty$)).

space of conducting electrons that can emit molecular vibration quanta. Recalling that electron-vibration scattering is roughly proportional to N_λ, increased vibration populations enhance inelastic transport signals in return. Last, We also considered transport calculations where we change the decay rate. Figure 7-9 shows that the differential conductance approaches the equilibrium case as the decay rate increases.

7.2 CNT(3, 3) - C_6H_4 - CNT(3, 3)

In the previous benchmark, the cumulene wire, subject to Peierl's instability, was frozen in order to keep its metallic character, and a decay rate for molecular vibrations was used as a parameter. Here we replace the cumulene wire by a metallic (3, 3) carbon nanotube (CNT), which is mechanically stable. Using this electrode we derive a fully *ab initio* approach to calculate non-equilibrium populations under electron-vibration interactions.

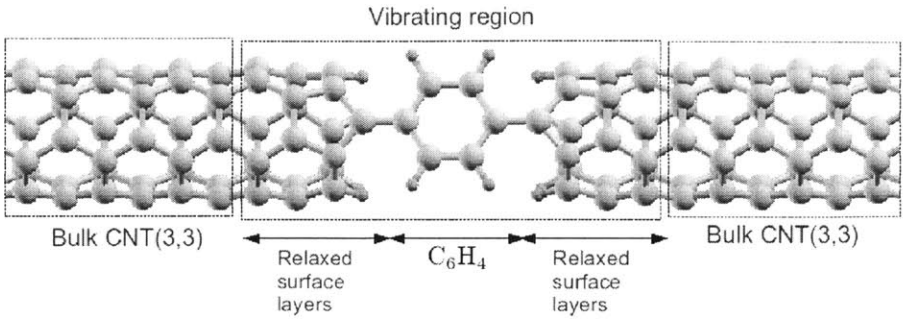

Figure 7-10: (3,3) CNT - Benzene - (3,3) CNT supercell geometry used in the decay rate calculations. The vibrating region contains a benzene molecule and three relaxed surface CNT layers.

Carbon-based nanostructures, such as CNT and graphene, could become new platforms for future nanotechnology applications due to their excellent electronic properties. Recently carbon-based nanojunctions have been experimentally fabricated: a pure carbon chain connected to graphene[43] or CNTs[7], and organic molecules coupled to CNT electrodes with amide linkages[30]. These experimental achievements stimulated theoretical and computational studies on carbon-based nanodevices [45, 63]. In particular, a benzene molecule connected to CNT electrodes (which is the system of our interest) was suggested as a molecular switch, operated by controlling the relative angle between π-orbitals of the benzene and the π-oribtal manifold of CNT electrodes [63]. Functionality and performances of molecular devices are strongly affected by molecular geometries or anchoring points to the electrodes, and they may be affected by vibrations induced by conducting electrons. In the worst case, the local heating may break down the junctions.

7.2.1 System Details

In our work, we choose a vibrating region by defining an extended molecule in which a benzene and the outmost relaxed CNT layers are included. This extended molecule is seamlessly connected to the bulk CNT electrodes. The vibrating region contains 56 atoms in total, and these correspond to 168 vibrational modes. Figure 7-10 illustrates the supercell geometry used in the decay rate calculations: It contains the extended

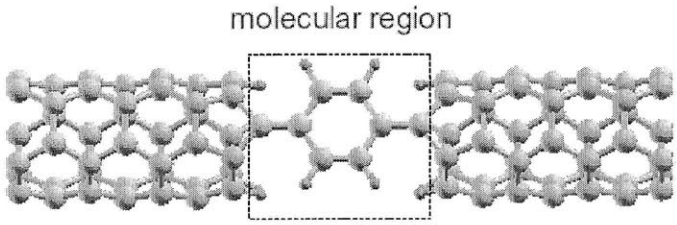

Figure 7-11: Molecular region containing a benzene molecule, anchoring carbon atoms, and hydrogen atoms saturating the CNT edge.

molecule and two *mechanical* principal layers[55] for bulk phonons.

We proceed as follows. First, by allowing only the extended molecule to vibrate, the electron-vibration interaction $\mathcal{H}_{el-vib}$, the vibrational spectrum $\{\hbar\omega_\lambda\}$, and the corresponding normal modes are calculated. For the decay rates the interatomic force constants for the entire supercell in Fig. 7-10 are calculated. From this interatomic force constants one can extract the harmonic coupling matrix $\mathcal{H}_C$ between the extended molecule and the bulk electrodes. In addition, we take a peridoic unit cell of the bulk $(3,3)$ CNT and calculate its interatomic force constants H_B.

7.2.2 Decaying Rates

The calculated decay rates are shown in Fig. 7-12 (a). Note that the decay rates are written in units of eV (of multiplying by $\hbar$). While most of the decay rates are of the order of 10^{-2} to 10^{-3} eV, there are few modes with much smaller rates. These small decay rates can arise for two reasons. First, as seen in Fig. 7-12 (a), decay rates start to increase significantly from mode 153 on. These vibrational modes (between 153 and 168) have energies higher than the highest $(3,3)$ CNT phonon energy. Recalling that decay processes based on the harmonic coupling essentially correspond to *one vibration to one phonon* transitions, there are no bulk phonons to which the vibrational modes lying outside the band width of bulk phonons can transfer their vibrational energies. Once the *anharmonic* coupling that makes *one vibration to multi-phonons* transition possible is taken into account, these modes may have larger decay rates. However, this correction is beyond our work.

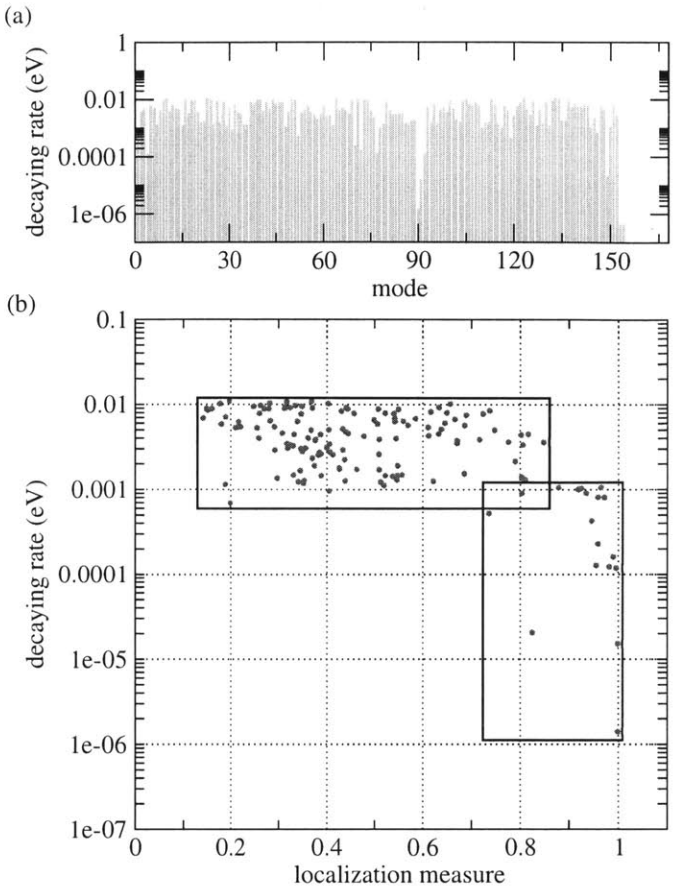

Figure 7-12: (a) Decay rates for each vibrational mode of the $(3,3)$ CNT-Benzene-$(3,3)$ CNT junction. (b) Decay rate vs. localization (see the text for the definition). Decay rates are plotted in a logarithmic scale.

Second, notice that among the vibrational modes whose energies lie inside the bulk phonon dispersions, some of them still have small decay rates. Most of them correspond to vibrations that are localized inside the benzene molecule, or to *wagging* motions of the surface hydrogen atoms. Because these motions are spatially well separated from bulk phonons, one may expect that they are less coupled to bulk phonons. In order to measure how localized these modes are inside the molecule, we define the benzene molecule, two anchoring carbon atoms, and the surface hydrogen atoms as the *molecular region* as seen in Fig. 7-11. When $\mathcal{P}_M$ denotes a projection operator onto the molecular region, one can find out how localized the vibration is inside the molecular region from $|\mathcal{P}_M|\lambda\rangle|^2$ where $|\lambda\rangle$ indicates the vibrational state for

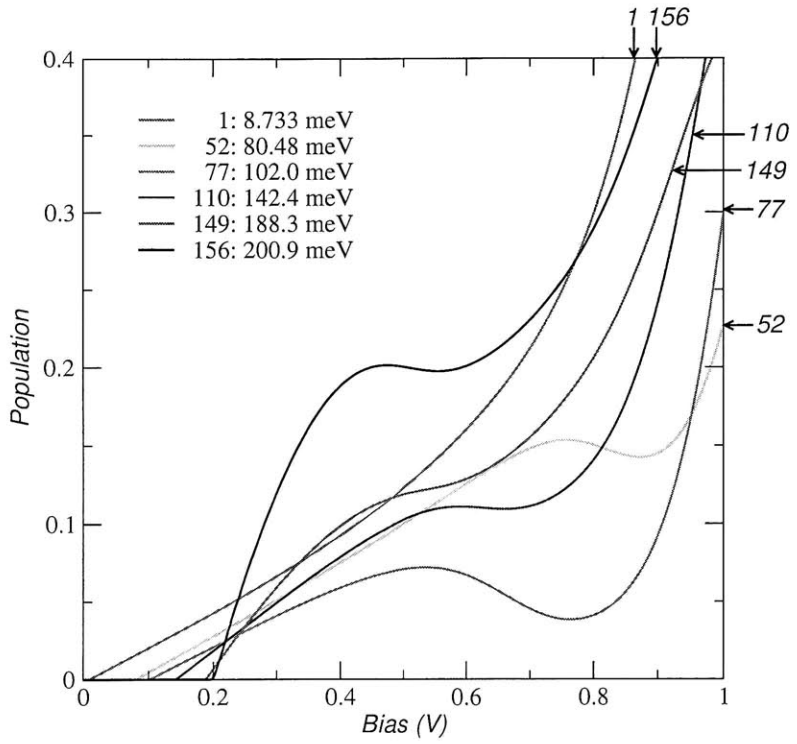

Figure 7-13: Nonequilibrium vibrational populations for the most excitable modes as a function of a bias voltage.

the normal mode λ. We call $|\mathcal{P}_M|\lambda\rangle|^2$ the *localization measure*. Figure 7-12 (b) shows a relation between the localization measures and decay rates. When the vibration is localized in the molecular region, or equivalently $|\mathcal{P}_M|\lambda\rangle|^2$ approaches 1, its decay rate becomes smaller.

Except for modes between 153 and 168, the majority of the vibrational modes overlap with the phonon dispersions of the CNT electrodes. This happens thanks to the same chemical character between hydrocarbon molecules and carbon-based electrodes. If we were to consider organic molecules attached to a metal electrode such as gold or platinum, the large mass difference between atoms in the molecule and those in the electrode would make most of the molecular modes to lie outside the electrode phonon dispersions. Therefore, most of the vibrational modes would have very small decay rates, significantly increaseing the probability of the molecular junction to break down.

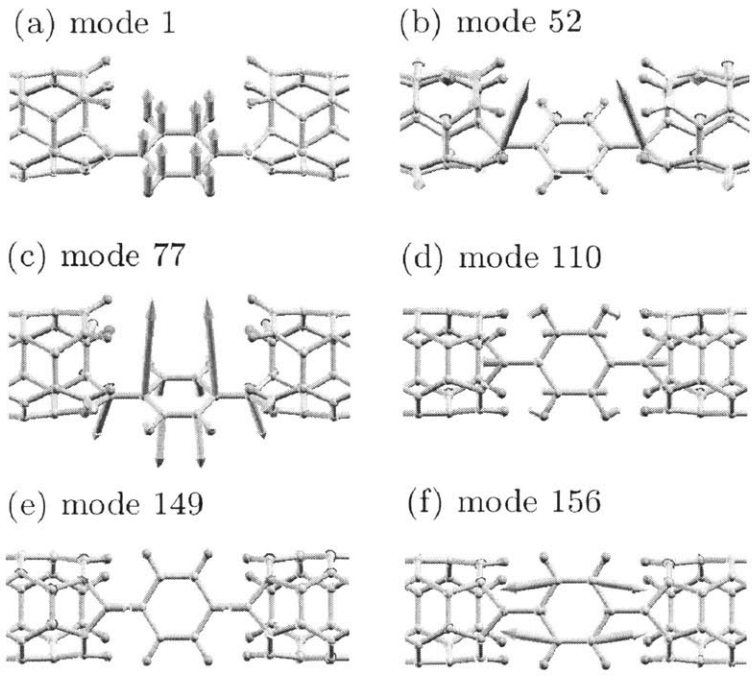

Figure 7-14: Vibrational configurations for the most excitable modes in Fig. 7-13.

7.2.3 Non-Equilibrium Vibration Populations

Together with Eq. (5.48), we can calculate nonequilibrium vibrational populations. Vibrational occupations will start to increase as the bias voltage exceeds their corresponding threshold voltages. While in the vicinity of the threshold voltage the vibrational populations increase linearly, nonlinear effects can appear at higher bias voltages. For low-energy modes vibrational populations monotonically increase with the bias; However, non-monotomic populations are observed for some of the high-energy modes. These trends are shown in Fig. 7-13, where vibrational populations for some of the highly excitable modes are illustrated. The mode 1, which is low-energy, shows monotonically increasing behaviors. For the other high-energy modes, their populations increase, then decrease in a certain bias voltage range, and then start to increase again.

One can hint at a qualitative explanation for this cooling behavior examining the local density of states in the device region, as recently reported in Ref. [81]. As

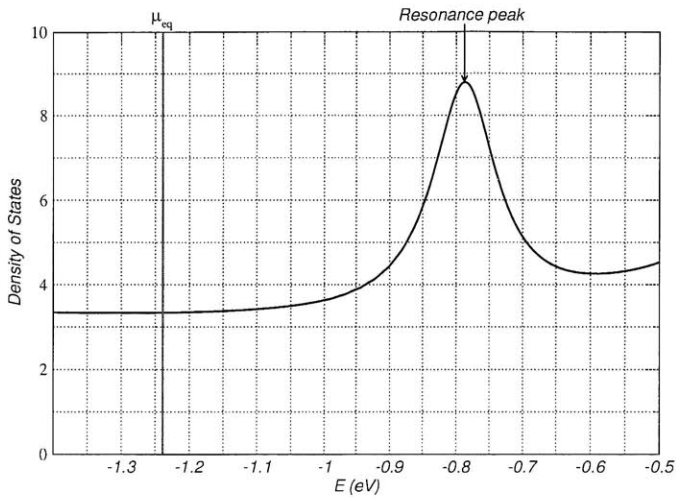

Figure 7-15: Density of states for the device region. Close to the equilibrium Fermi level, one resonance peak is found.

observed in Fig. 7-15, there is one resonant peak located at a energy higher than μ_{eq}, which is the common Fermi level before the bias is applied. Figure 7-16 shows absorption and emission processes where electrons can exploit the resonant density of states for different bias voltages. Red and blue lines indicate absorption and emission processes respectively. For a very small bias none of the electrons can access the resonant peak, as seen in Fig. 7-16-(a). When the bias increases, the absorption process using the resonant peak starts to take place, but the electrons participating in the emission process cannot reach the resonance (See Fig. 7-16-(b)). Therefore the absorption rate A_λ becomes enhanced, so it may lead to a decrease in vibrational populations. For a higher biases such that the resonant peak is located between left and right chemical potentials, the emission process using the resonance is activated, leading to enhanced emission rates, as shown in Fig.7-16-(c). When the bias increases more, another resonant emission process becomes possible, as shown in Fig. 7-16-(d), while the resonant absorption process at which the electrons are reflected back to the left lead is prohibited due to Pauli blocking. As a result, the emission rate becomes more enhanced in comparison to the absorption one, and vibrational populations may increase again in this bias range. As an illustratative example, Fig. 7-17-(b) shows the absorption and emission rates for mode 156. One can clearly observe that the bias

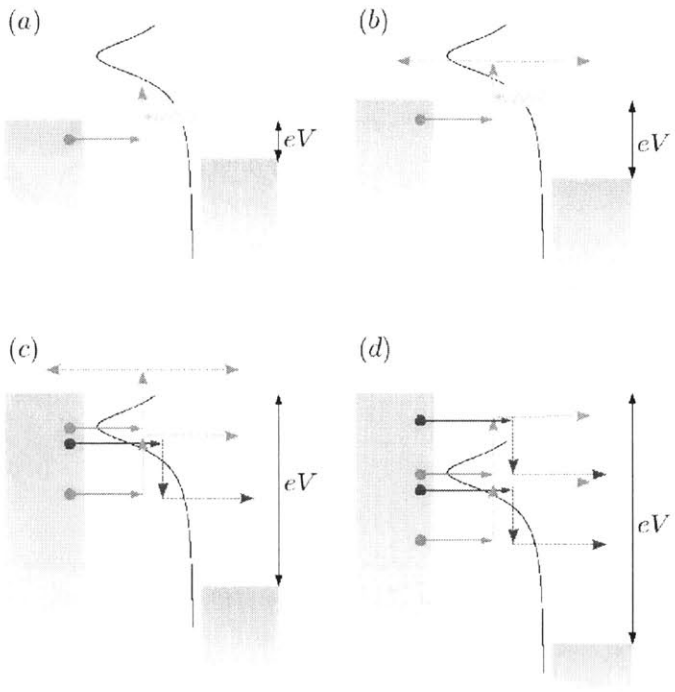

Figure 7-16: Possible absorption (red arrow line) and emission (blue arrow line) processes via the resonant peak as the bias voltage increases.

voltages for which the absorption and emission rates get enhanced are different: The slope of the absorption rate curve first increases around 0.4 V, but then decreases at 0.7 V. By contrast, the emission rate linearly increases up to 0.8 V, and at a bias larger than 0.8 V its slope also increases. Difference between bias voltages at which absorption and emission rates become enhanced results in the observed cooling behavior in the intermediate bias range.

For low-energy modes whose energies are much smaller than the broadening of the resonant peak, the intermediate cooling regime may not distinctly appear. For example, see Fig. 7-17-(a) the absorption and emission rates for mode 1. Unlike mode 156, the absorption and emission rates show quite similar dependence on the bias voltage, implying that the cooling behavior is not observed.

Last, not every high-energy mode goes necessarily through a cooling down phase, since vibrational populations are determined by the interplay of absorption, emission,

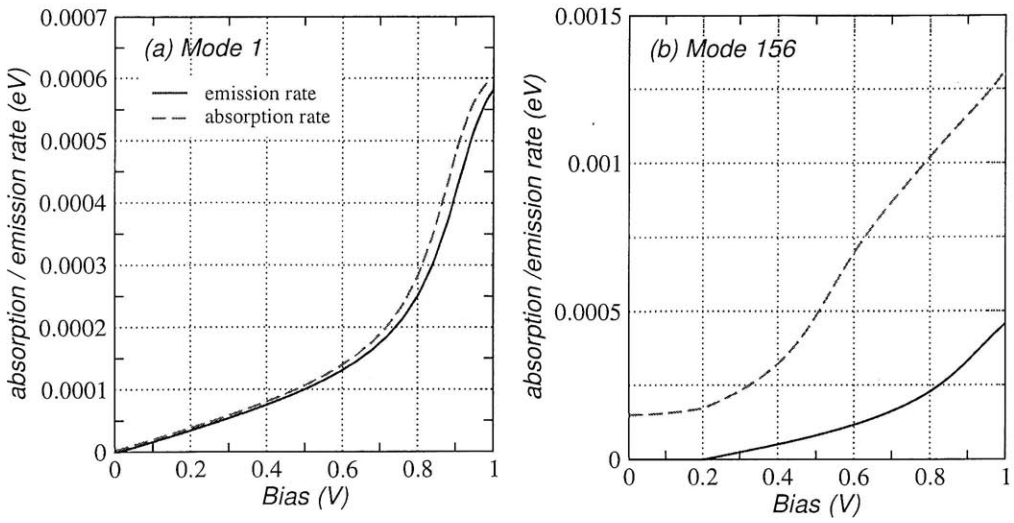

Figure 7-17: Absorption (red dashed line) and emission (blue solid line) rates for (a) the vibrational mode 1 (low-energy mode) and (b) 156 (high-energy mode)

and decay rates. When the decay rate γ_λ is larger than the difference between the absorption and emission rates $A_\lambda - E_\lambda$, the steady state solution can be approximated as

$$N_\lambda = \frac{n_B(\hbar\omega_\lambda) + E_\lambda}{\gamma_\lambda + A_\lambda - E_\lambda} \approx n_B(\hbar\omega_\lambda) + \frac{E_\lambda}{\gamma_\lambda}. \tag{7.11}$$

In this case, the dependence of the vibrational population on the bias voltage becomes similar to that of the emission rate, and the cooling behavior does not appear.

Finally, we would like to stress the importance of the mass ratios between the conducting molecule and electrodes. As pointed out above, since the band width of bulk phonons in the electrodes gets narrower as the atomic mass of electrodes increases, a molecular junction connected to electrodes consisting of heavier atoms will have less opportunities to thermalize. To demonstrate this mass ratio effect, we calculate the total vibrational energy stored in the vibrating region by increasing the mass of the atoms in the carbon electrode to be e.g. silicon or germanium. As shown in Fig. 7-18, the junction with a larger mass ratio has more vibrational energy, and higher probability to break down due to heating effects.

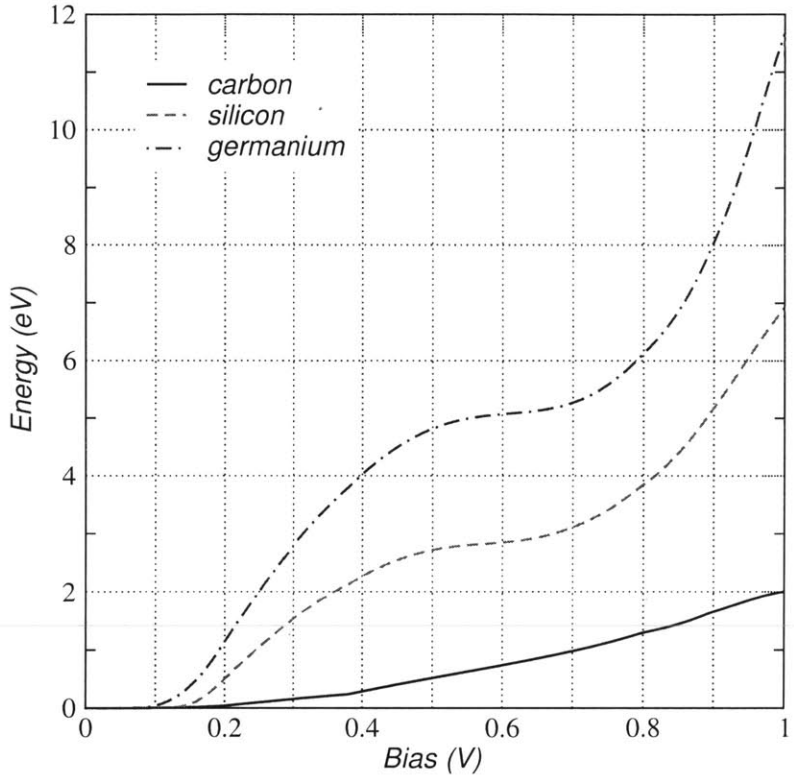

Figure 7-18: Total vibrational energy stored in the vibrating region, as a function of the mass of the electrode atom (black solid line: carbon; red dashed line: silicon; blue dot-dahsed line: germanium).

Chapter 8

Inelastic Local Currents in Molecular Electronics

Nanoscale electronics has been intensively developed over the last decade thanks to advancements in fabrication and measurement technologies. Molecular and atomic conductors, which are regarded as the smallest devices, are actively investigated as candidates for future nanoscale devices [1]. However, there are still many issues to be resolved both experimentally and theoretically.

The effect of electron-vibration interactions on molecular conductors is one of the main issues that have been recently investigated [29]. This is because current-driven atomic excitations might lead to changes in molecular configurations and geometries, thereby affecting performance and functionality of the device. Furthermore, since electron-vibration interactions act as scattering mechanisms, the I-V characteristics also change. However, most of the theoretical work has focused on studying the properties of the net current, and understanding and describing the microscopic picture of inelastic local currents has been rarely attempted.

The spatial and local distributions of elastic currents have been studied in various systems, for example, imaging of the local current in a quantum point contact [94], a disordered quantum wire under a magnetic field [20], a quantum Hall geometry in a two-dimensional electron gas [21], and the formation of a local loop current and a magnetic moment in the C_{60} molecule[67]. In particular, local current profiles have

been calculated in order to investigate quantum interference in molecular junctions [88]. This is particularly since one can interpret quantum interference by applying the concept of Feynman paths to the visualized local current [22].

In this study we derive the expression for the local current profile in a nanoscale junction in the presence of electron-vibration interactions. Considering a weak coupling regime, we calculate the local current up to the second order in the electron-vibration interaction by using non-equilibrium Green's functions [79]. Furthermore, we provide a simplified expression of the local current that approximately holds when the electronic structure changes slowly in comparison with a typical vibrational energy [72]. As an illustrative example we calculate the local current profile for a benzene molecule connected to carbon monoatomic chains to show how the local current distribution can be affected by electron-vibration interactions.

8.1 Local current operator

The average local current can be readily calculated by taking a time derivative of the electron number operator at the site m [88]:

$$\langle \hat{I}_m \rangle = -2e \left\langle \frac{d}{dt} \left[\sum_{i \in m} c_i^\dagger(t) c_i(t) \right] \right\rangle = \frac{2ei}{\hbar} \sum_{i \in m} \left\langle \left[c_i^\dagger c_i, \mathcal{H}_D \right] \right\rangle , \tag{8.1}$$

where i indicates localized orbitals located at the site m. In this letter, we have used the *maximally localzied Wannier functions* as localized orbitals [64]. $\mathcal{H}_D$ is the Hamiltonian for the device region including electron-vibration interactions, $\mathcal{H}_D = \sum_i \varepsilon_i c_i^\dagger c_i + \sum_{i \neq j} V_{ij} c_i^\dagger c_j + \sum_\lambda \sum_{i,j} \mathcal{M}_{ij}^\lambda (b_\lambda + b_\lambda^\dagger) c_i^\dagger c_j$. Here c_i and $c_i^\dagger$ are electronic annihilation and creation operators for the ith localized orbital, and b_λ and $b_\lambda^\dagger$ are vibronic annihilation and creation operators for the λth vibrational mode. ε_i is the on-site energy for the ith orbital, V_{ij} is the hopping parameter between the ith and jth orbitals, and $\mathcal{M}_{ij}^\lambda$ is the electron-vibration coupling term. Unless a spin-orbit coupling is considered, electron-vibration interactions do not distinguish between spin degrees of freedom, and so the spin index is not explicitly indicated here (Hence the factor two

in the current expression). Equation (8.1) can be written as $\langle \hat{I}_m \rangle = \sum_m \sum_n \langle \hat{I}_{mn} \rangle$, where $\langle \hat{I}_{mn} \rangle$ is the local current from site n to site m,

$$\begin{aligned} \langle \hat{I}_{mn} \rangle &= 2e \sum_{\substack{i\in m \\ j\in n \\ n\neq m}} \Big[\left(V_{ij} G^<_{ji}(t,t) - V_{ji} G^<_{ij}(t,t) \right) \\ &\quad + \sum_\lambda \left[\mathcal{M}^\lambda_{ij} G^<_{j,\lambda i}(t,t) - \mathcal{M}^\lambda_{ji} G^<_{i,\lambda j}(t,t) \right] \Big], \end{aligned} \tag{8.2}$$

where $G^<_{ij}(t,t)$ and $G^<_{i,\lambda j}(t,t)$ are the lesser part of the contour-ordered Green's functions [33]

$$G_{ij}(\tau,\tau') = -\frac{i}{\hbar} \langle \mathcal{T}_c \left\{ c_i(\tau), c^\dagger_j(\tau') \right\} \rangle \tag{8.3}$$

$$G_{i,\lambda j}(\tau,\tau') = -\frac{i}{\hbar} \left\langle \mathcal{T}_c \left\{ c_i(\tau), \left(b_\lambda + b^\dagger_\lambda \right)(\tau') c^\dagger_j(\tau') \right\} \right\rangle \tag{8.4}$$

Under steady state, Eq.(8.2) becomes

$$\langle \hat{I}_{mn} \rangle = I^{el}_{mn} + I^{vib}_{mn}, \tag{8.5}$$

where

$$I^{el}_{mn} = \frac{2e}{\hbar} \sum_{i\in m} \sum_{\substack{j\in n \\ n\neq m}} \int \frac{d\varepsilon}{2\pi} \left(V_{ij} G^<_{ji}(\varepsilon) - V_{ji} G^<_{ij}(\varepsilon) \right) \tag{8.6}$$

$$I^{vib}_{mn} = \frac{2e}{\hbar} \sum_{i\in m} \sum_{\substack{j\in n \\ n\neq m}} \sum_\lambda \int \frac{d\varepsilon}{2\pi} \left[\mathcal{M}^\lambda_{ij} G^<_{j,\lambda i}(\varepsilon) - \mathcal{M}^\lambda_{ji} G^<_{i,\lambda j}(\varepsilon) \right]. \tag{8.7}$$

The local current is thus decomposed into two parts I^{el}_{mn} and I^{vib}_{mn}. In the first part I^{el}_{mn}, when the hopping parameters between two localized orbitals V_{ij} are fixed, the electron-vibration interaction can still change the correlation function between orbitals $G^<_{ij}$. The other physical effect of the electron-vibration interaction is that it can modulate the hopping parameters, which are roughly determined by overlap

between localized orbitals. One can note that the second part I^{vib}_{mn} includes this contribution, since $\mathcal{M}^{\lambda}_{ij}\left(b_\lambda + b^\dagger_\lambda\right)$ describes the hopping parameter variation due to the electron-vibration interaction. Recalling the net current measured in the electrode, the second part is newly introduced for the local current. In order to calculate the local current profile with electron-vibration interactions, one might be tempted just to replace the non-interacting Green's function by the full Green's function $G^<$ in the elastic local current expression. However, Eq.(8.2) points out that this replacement would be incorrect, and hopping modulation due to vibrations should be included.

8.2 Lowest-order Perturbation

Assuming weak electron-vibration coupling, Green's functions can be expanded up to the second order of the electron-vibration coupling $\mathcal{M}^\lambda$. Using Dyson and Keldysh equations for the contour-ordered Green's functions, the correlation function $G^<$ in Eq.(8.6) is found to be

$$G^< \approx G^<_0 + G^<_{(2)}, \tag{8.8}$$

where

$$G^<_{(2)} = G^r_0 \Sigma^r_{vib} G^<_0 + G^<_0 \Sigma^a_{vib} G^a_0 + G^r_0 \Sigma^<_{vib} G^a_0, \tag{8.9}$$

where G_0 indicates the non-interacting Green's function that includes only the coupling to the electrodes. The electron-vibration self-energies up to the second order are given by

$$\Sigma^{r,a}_{vib} = \frac{1}{2}\left(\pm\Sigma^>_{vib} \mp \Sigma^<_{vib} - \frac{i}{2}\mathcal{H}\left\{\Sigma^>_{vib} - \Sigma^<_{vib}\right\}\right) + \Sigma^r_H \tag{8.10}$$

$$\Sigma^{\lessgtr}_{vib} = \sum_\lambda \mathcal{M}^\lambda \left[n_\lambda G^<_0\left(\varepsilon \mp \hbar\omega_\lambda\right) + \left(n_\lambda + 1\right) G^<_0\left(\varepsilon \pm \hbar\omega_\lambda\right)\right]\mathcal{M}^\lambda \tag{8.11}$$

$$\Sigma^r_H = -\sum_\lambda\left(\frac{4}{\hbar\omega_\lambda}\sum_\alpha \int \frac{d\varepsilon}{2\pi}\mathrm{Tr}\left[\mathcal{M}^\lambda A_\alpha(\varepsilon)\right] f_\alpha(\varepsilon)\right), \tag{8.12}$$

where $\mathcal{H}\{f\}$ indicates the Hilbert transform, n_λ is the vibrational population for mode λ, and $f_\alpha(\varepsilon) = f(\varepsilon - \mu_\alpha)$ is the Fermi-Dirac function for the electrode α.

Σ_H^r is the Hartree diagram contribution, which does not have an energy dependence. Therefore I_{mn}^{el} can be further decomposed into a non-interacting part and a correction due to electron-vibration interactions:

$$I_{mn}^{el} = I_{mn}^{el,(0)} + I_{mn}^{el,(2)}, \tag{8.13}$$

where

$$I_{mn}^{el,(0)} = \frac{2e}{\hbar} \sum_{i\in m} \sum_{\substack{j\in n \\ n\neq m}} \int \frac{d\varepsilon}{2\pi} \left(V_{ij} G_{0,ji}^{<}(\varepsilon) - V_{ji} G_{0,ij}^{<}(\varepsilon) \right) \tag{8.14}$$

$$I_{mn}^{el,(2)} = \frac{2e}{\hbar} \sum_{i\in m} \sum_{\substack{j\in n \\ n\neq m}} \int \frac{d\varepsilon}{2\pi} \left(V_{ij} G_{(2),ji}^{<}(\varepsilon) - V_{ji} G_{(2),ij}^{<}(\varepsilon) \right). \tag{8.15}$$

The vibronic contribution I_{mn}^{vib} can be obtained by using the $\mathcal{S}$-matrix expansion or equation-of-motion technique. The final expression reads

$$I_{mn}^{vib} \approx \frac{2e}{\hbar} \sum_{i\in m} \sum_{\substack{j\in n \\ n\neq m}} \sum_{\lambda} \int \frac{d\varepsilon}{2\pi} \left[\mathcal{M}_{ij}^{\lambda} G_{j,\lambda i}^{<}(\varepsilon) - \mathcal{M}_{ji}^{\lambda} G_{i,\lambda j}^{<}(\varepsilon) \right], \tag{8.16}$$

where

$$\begin{aligned} G_{i,\lambda j}^{<}(\varepsilon) = \frac{i}{\hbar} \sum_{mn} \mathcal{M}_{mn}^{\lambda} \Bigg[& \int \frac{d\varepsilon'}{2\pi} G_{0,im}^{r}(\varepsilon)\, G_{0,nj}^{<}(\varepsilon - \varepsilon')\, D_{\lambda}^{<}(\varepsilon') \\ & + G_{0,im}^{<}(\varepsilon)\, G_{0,nj}^{<}(\varepsilon - \varepsilon')\, D_{\lambda}^{a}(\varepsilon') \\ & + G_{0,im}^{<}(\varepsilon)\, G_{0,nj}^{a}(\varepsilon - \varepsilon')\, D_{\lambda}^{>}(\varepsilon') \\ & - G_{0,nm}^{<}(\varepsilon) \int \frac{d\varepsilon}{2\pi} G_{0,ij}^{<}(\varepsilon)\, D_{\lambda}^{a}(0) \Bigg], \end{aligned} \tag{8.17}$$

and

$$D_{\lambda}^{r/a}(\varepsilon) = \frac{1}{\varepsilon - \hbar\omega_{\lambda} \pm i0^{+}} - \frac{1}{\varepsilon + \hbar\omega_{\lambda} \pm i0^{+}} \tag{8.18}$$

$$D_{\lambda}^{\lessgtr}(\varepsilon) = -i2\pi \left[n_{\lambda} \delta(\varepsilon \mp \hbar\omega_{\lambda}) + (n_{\lambda} + 1)\, \delta(\varepsilon \pm \hbar\omega_{\lambda}) \right] \tag{8.19}$$

are free non-equilibrium Green's functions for the vibrational mode λ.

8.3 Wide-band limit

One might further approximate Eqs. (8.14) and (8.15) by replacing G_0 and $\Gamma_{\alpha=L,R}$ by $G_0(\varepsilon_F)$ and $\Gamma_{\alpha=L,R}(\varepsilon_F)$ at the common Fermi energy ε_F. This is called the lowest-order expansion in the wide-band limit (LOE-WBL) [72, 27, 97, 34]. This approximation is useful because a typical vibrational energy is smaller than the energy scale where the electronic structure changes. Moreover, LOE-WBL also provides an approximate expression of the bias dependence in the current expression. I_{mn}^{LOE} reads

$$
\begin{aligned}
I_{mn}^{\mathrm{LOE}} &= G_0 V \sum_{i\in m}\sum_{\substack{j\in n\\ n\neq m}} \mathcal{T}_{0,ij}^{el} && (8.20)\\
&+G_0 V \sum_{i\in m}\sum_{\substack{j\in n\\ n\neq m}}\sum_{\lambda} \left[\gamma_H \mathcal{T}_{H,ij}^{el} + (2n_\lambda+1)\,\mathcal{T}_{F,ij}^{el}\right] && (8.21)\\
&+\sum_{i\in m}\sum_{\substack{j\in n\\ n\neq m}}\sum_{\lambda} \mathcal{T}_{sym,ij}^{el,\lambda} \times \mathcal{K}\left(eV,\omega_\lambda\right) && (8.22)\\
&+\sum_{i\in m}\sum_{\substack{j\in n\\ n\neq m}}\sum_{\lambda} \mathcal{T}_{asy,ij}^{el,\lambda} \times \mathcal{G}\left(eV,\omega_\lambda\right) && (8.23)\\
&+G_0 V \sum_{i\in m}\sum_{\substack{j\in n\\ n\neq m}}\sum_{\lambda} \left[\gamma_H \mathcal{T}_{H,ij}^{vib} + (2n_\lambda+1)\,\mathcal{T}_{F,ij}^{vib}\right] && (8.24)\\
&+\sum_{i\in m}\sum_{\substack{j\in n\\ n\neq m}}\sum_{\lambda} \mathcal{T}_{sym,ij}^{vib} \times \mathcal{K}\left(eV,\omega_\lambda\right) && (8.25)\\
&+\sum_{i\in m}\sum_{\substack{j\in n\\ n\neq m}}\sum_{\lambda} \mathcal{T}_{asy,ij}^{vib} \times \mathcal{G}\left(eV,\omega_\lambda\right). && (8.26)
\end{aligned}
$$

where

$$
\mathcal{T}_{0,ij}^{el} = 2V_{ij}\mathrm{Im}\left[A_L\right]_{ji} \tag{8.27}
$$

$$
\mathcal{T}_{H,ij}^{el,\lambda} = 2V_{ij}\mathrm{Im}\left[G_0^r \mathcal{M}^\lambda A_L + A_L \mathcal{M}^\lambda G_0^a\right]_{ji} \tag{8.28}
$$

$$\begin{aligned}\mathcal{T}_{F,ij}^{el,\lambda} &= 2V_{ij}\mathrm{Im}\left[G_0^r\mathcal{M}^\lambda\mathrm{Re}G_0^r\mathcal{M}^\lambda A_L\right. \\ &\quad +A_L\mathcal{M}^\lambda\mathrm{Re}G_0^r\mathcal{M}^\lambda G_0^a\big]_{ji} \\ &\quad +V_{ij}\mathrm{Im}\left[G_0^r\mathcal{M}^\lambda A_L\mathcal{M}^\lambda G_0^r\right. \\ &\quad \left.+G_0^a\mathcal{M}^\lambda A_L\mathcal{M}^\lambda G_0^a\right]_{ji} \end{aligned} \tag{8.29}$$

$$\begin{aligned}\mathcal{T}_{sym,ij}^{el,\lambda} &= V_{ij}\mathrm{Re}\left[G_0^r\mathcal{M}^\lambda\left[A_L\mathcal{M}^\lambda A_R - A_R\mathcal{M}^\lambda A_L\right]\right. \\ &\quad \left.+\left[A_L\mathcal{M}^\lambda A_R - A_R\mathcal{M}^\lambda A_L\right]\mathcal{M}^\lambda G_0^a\right]_{ji} \end{aligned} \tag{8.30}$$

$$\begin{aligned}\mathcal{T}_{asy,ij}^{el,\lambda} &= V_{ij}\mathrm{Im}\left[G_0^r\mathcal{M}^\lambda\left(A_L\mathcal{M}^\lambda A_R + A_R\mathcal{M}^\lambda A_L\right)\right. \\ &\quad \left.+\left(A_L\mathcal{M}^\lambda A_R + A_R\mathcal{M}^\lambda A_L\right)\mathcal{M}^\lambda G_0^a\right]_{ji} \end{aligned} \tag{8.31}$$

$$\mathcal{T}_{H,ij}^{vib,\lambda} = 2\mathcal{M}_{ij}^\lambda\mathrm{Im}\left[A_L\right]_{ji} \tag{8.32}$$

$$\mathcal{T}_{F,ij}^{vib,\lambda} = 2\mathcal{M}_{ij}^\lambda\mathrm{Im}\left[\mathrm{Re}G^r\mathcal{M}^\lambda A_L + A_L\mathcal{M}^\lambda\mathrm{Re}G^r\right]_{ji} \tag{8.33}$$

$$\mathcal{T}_{sym,ij}^{vib,\lambda} = \mathcal{M}_{ij}^\lambda\mathrm{Re}\left[A_L\mathcal{M}^\lambda A_R - A_R\mathcal{M}^\lambda A_L\right]_{ji} \tag{8.34}$$

$$\mathcal{T}_{asy,ij}^{vib,\lambda} = \mathcal{M}_{ij}^\lambda\mathrm{Im}\left[A_L\mathcal{M}^\lambda A_R + A_R\mathcal{M}^\lambda A_L\right]_{ji} \tag{8.35}$$

$$\gamma_H^\lambda = \left(\frac{4}{\hbar\omega_\lambda}\sum_\alpha\int\frac{d\varepsilon}{2\pi}\mathrm{Tr}\left[\mathcal{M}^\lambda A_\alpha(\varepsilon)\right]f_\alpha(\varepsilon)\right), \tag{8.36}$$

where $A_{\alpha=L,R} = G_0^r\Gamma_\alpha G_0^a$ is the spectral function originating from the left or right electrode, and $G_0 = 2e^2/h$. Green's functions and spectral functions are calculated at ε_F except for the spectral functions in Eq. (8.36). This is because the spectral function in Eq. (8.36) does not have a finite support [34], so LOE-WBL cannot be applied to these terms. Equations (8.21), (8.22), and (8.23) originate from I_{mn}^{el}, while Eqs. (8.24), (8.25), and (8.26) come from I_{mn}^{vib}. The functions $\mathcal{K}\left(eV,\omega_\lambda\right)$ and

$\mathcal{G}(eV, \omega_\lambda)$ are defined as follows:

$$\mathcal{K}(eV, \omega_\lambda) = \frac{2e}{\pi\hbar}\left(\frac{\hbar\omega_\lambda - eV}{e^{\beta(\hbar\omega_\lambda - eV)} - 1} - \frac{\hbar\omega_\lambda + eV}{e^{\beta(\hbar\omega_\lambda + eV)} - 1} + 2n_\lambda eV\right) \tag{8.37}$$

$$\begin{aligned}\mathcal{G}(eV, \omega_\lambda) &= \frac{2e}{\hbar}\int \frac{d\varepsilon}{2\pi}\left[f(\varepsilon) - f(\varepsilon - eV)\right] \\ &\quad \times \mathcal{H}_{\varepsilon'}\left\{f(\varepsilon' - \hbar\omega_\lambda) - f(\varepsilon' + \hbar\omega_\lambda)\right\}(\varepsilon)\,.\end{aligned} \tag{8.38}$$

When compared with the total current measured in the electrode [72, 27, 97, 34], each term in I^{LOE}_{mn} can be separatively and meaningfully discussed. Equation (8.20) corresponds to the elastic local current when the electron-vibration interaction is absent. Equations (8.28) and (8.32) are quasi-elastic correction due to the Hartree diagram, while Eqs. (8.29) and (8.33) correspond to quasi-elastic contributions coming from the Fock diagram. Energy levels renormalized due to the electron-vibration interactions lead to these quasi-elastic contributions, which are linearly proportional to the bias voltage. Equations (8.22) and (8.25) are symmetric under the change in the polarity of the bias voltage, $V \to -V$. Meanwhile, Eqs (8.23) and (8.26), which are negligible for a symmetric junction, show asymmetric bias dependence. Equations (8.37) and (8.38) and their derivatives show singular behaviors, for example, a step or a peak structure, which indicate the onset of real vibrational scattering at the threshold voltage $eV = \hbar\omega_\lambda$. Note that Eqs. (8.23) and (8.26) vanish in a symmetric molecular junction, where couplings to the left and right electrode are equal.

8.3.1 Example: Cumulene - C_6H_4 - Cumulene

As an illustrative example we calculate the local current profile for a benzene molecule connected to a cumulene mono-atomic carbon chain (See Fig.8-1 for the atomic configuration and the coordinate system). This system was investigated in our recent work in which an *ab initio* inelastic quantum transport formalism based on Wannier functions was developed [47].

This system has two elastic conducting channels: the major channel $|\Psi_1\rangle$ consisting of p_z orbitals in the cumulene and the benzene molecule, and the minor channel

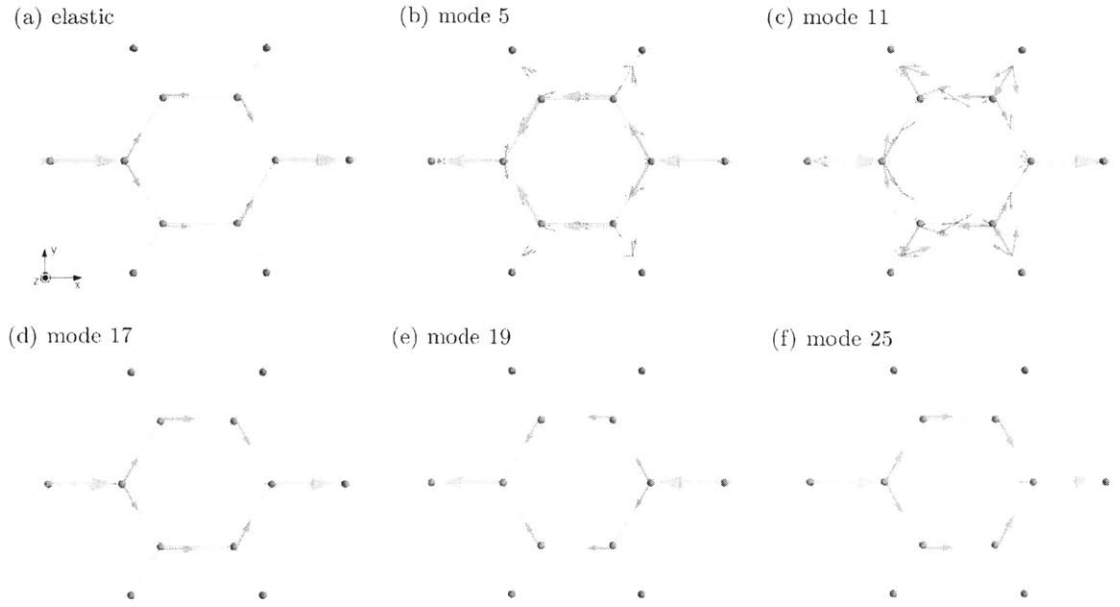

Figure 8-1: Local profiles for elastic current and inelastic currents induced by five active modes. Green and gray spheres indicate hydrogen and carbon atoms. The arrow scale is arbitrary chosen for better illustration.

$|\Psi_2\rangle$ composed of p_y orbitals on the cumulene wire and σ-type midbond states on the benzene molecule. Their transmissions coefficients are $\mathcal{T}_1 = 0.741$ and $\mathcal{T}_2 = 0.004$ respectively.

When the differential conductance G and its derivative dG/dV are calculated, five active vibrational modes are found (see Fig.7-5). In the first two active modes leading to upward peaks in dG/dV, atoms move out of the plane on which the benzene molecule lies. The other three downward peaks correspond to in-plane motions where carbon-carbon bonds inside the benzene molecule and between the benzene and the cumulene chain vibrate.

Figure 8-1 shows the local current profiles for the elastic contribution and the five active modes at the bias voltage $0.2V$. In-plane vibrations (mode 17, 19, and 25) induce current flow along carbon-carbon bonds. The current patterns of these in-plane motions are the same as that of the elastic current. In other words, in-plane motions just enhance or reduce the local profile of the elastic current. Note that

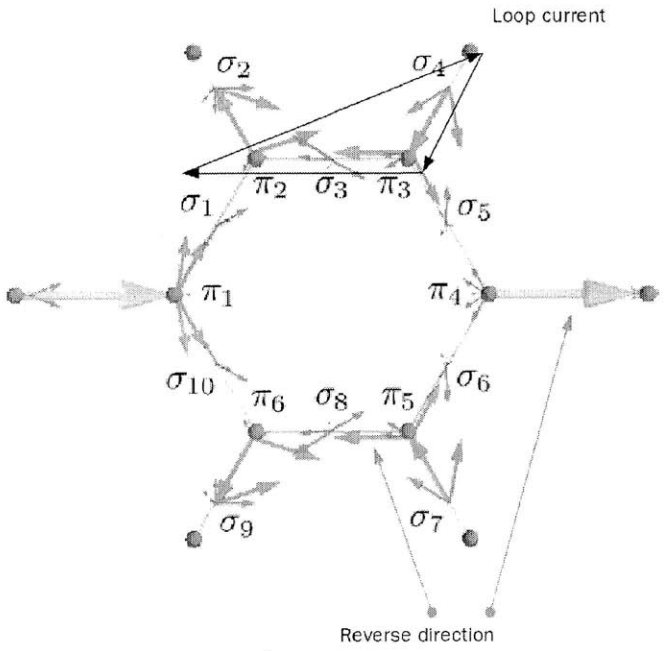

Figure 8-2: Local current profile for mode 11. π orbitals at carbon atoms and σ orbitals at carbon-carbon and carbon-hydrogen mid-bond sites are indicated.

σ-type mid-bonds do not participate in local currents of in-plane motions.

In contrast, the local currents for out-of-plane vibrations (mode 5 and 11) show a different profile since the inelastic current can flow via σ-bonds. This behavior is much clearer for mode 11. Most current flows along the π orbitals at carbon atoms for mode 5, with σ bonds contributing to small residual current for mode 5. In constrast, the significant amount of current for mode 11 is transferred to the right cumulene chain via σ-oribtals. One of the interesting features for mode 11 is that the local current between π_2 and π_3 orbitals flows in the direction opposite to the total current direction (from left to right), as seen in Fig.8-2. Different from other modes, the current reaching π_4 orbital passes through the σ_4 and σ_7 orbitals. Furthermore one can notice that there are local loop currents, i.e. among π_2, σ_4, and π_3.

The difference in the local current patterns between in-plane and out-of-plane motions can be understood from symmetry consideration. Regarding the parity symmetry with respect to zx-plane, whose operator is denoted by $\mathcal{P}_{zx}$, out-of-plane and

in-plane vibrations are anti-symmetric and symmetric respectively:

$$\mathcal{P}_{zx}\mathcal{M}^{\lambda=5,11}\mathcal{P}_{zx}^{\dagger} = -\mathcal{M}^{\lambda=5,11} \tag{8.39}$$

$$\mathcal{P}_{zx}\mathcal{M}^{\lambda=17,19,25}\mathcal{P}_{zx}^{\dagger} = \mathcal{M}^{\lambda=17,19,25}. \tag{8.40}$$

Furthermore, the major and minor conducting channels are symmetric and anti-symmetric under the parity operation $\mathcal{P}_{zx}$,

$$\mathcal{P}_{zx}|\Psi_1\rangle = |\Psi_1\rangle \tag{8.41}$$

$$\mathcal{P}_{zx}|\Psi_2\rangle = -|\Psi_2\rangle. \tag{8.42}$$

This symmetry condition implies that the transition between $|\Psi_1\rangle$ and $|\Psi_2\rangle$ is forbidden for the in-plane vibrations. Thus $|\Psi_1\rangle$ and $|\Psi_2\rangle$ are not mixed together by the in-plane vibrations, and the current profiles of the in-plane motions follow the elastic current.

Chapter 9

Transport properties of CNT-GNR junctions

Since the experimental realization of graphene [70, 69, 102], intense experimental and theoretical studies have been conducted in order to unveil its exceptional electronic properties and find out the possibility to use it as a platform for future devices and integrated circuits [68]. Graphene nanoribbons (GNRs), which have also been investigated, are regarded as candidates for interconnectors of graphene-based integrated circuits. Moreover, because of their peculiar electronic and spin transport properties, GNRs themselves have been studied to use as field effect transistors and spintronics devices. From the experimental viewpoint, it has been a challenge to produce smooth and defectless graphene, and its derivatives, in a controlled fashion. Several methods have been proposed for graphene and GNR production, from lithographic patterning [5, 32] to chemical methods [92, 58, 11] and nano-etching [23, 18, 10]. In particular, lithographic methods have been quite successfully employed to produce a wide graphene sheet ($>$ 20 nm) [5, 32]. Chemical vapor deposition has been used for bulk production of GNRs (to the order of grams per day) [11]. These existing methods, however, are not useful to control edge smoothness and width, and especially to produce narrow nanoribbons at the sub-10 nm scale.

Recently experimental techniques to make narrow GNRs have been proposed and demonstrated by unzipping carbon nanotubes (CNTs): Those have been cut longitu-

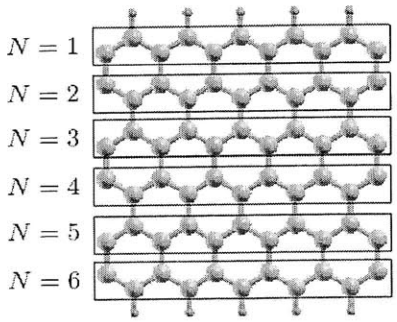

Figure 9-1: Classification of a zigzag nanoribbon by using the number of zigzag carbon chains. The given nanoribbon has 6 zigzag carbon chains as indicated. It is denoted by (N=6) ZGNR in this study.

dinally by using a solution-based oxidative process [53], plasma etching after partial embedding in a polymer film [42], and intercalation followed by exfoliation [12]. Furthermore, the group of Dai has demonstrated that well aligned GNR arrays can be produced by using plasma etching, because the initial alignment of CNT arrays can be maintained while CNTs are embedded in the polymer film, they are partly etched by plasma, and are transferred to another substrate [41].

Unzipped CNTs have been experimentally used to make CNT-GNR and CNT-GNR-CNT junctions [41]. The experimental realization of CNT/GNR junctions has stimulated theoretical investigations on their electronic properties and the possibility of using them as nano-devices such as heterojunction field-effect transistors [101, 61], magnetoresistive devices [86, 98], and nanosensors [48].

Differently from these works that have calculated total zero-bias elastic conductances, we present here *ab initio* transport calculations on armchair CNT (ACNT)-zigzag GNR (ZGNR)-ACNT junctions that focus on the local current distribution over the junctions. In the following section we show the local current distribution of the elastic current through the junctions in comparison with that of pristine ZGNRs. Next we investigate inelastic transport properties and the effect of vibrations on the local current distribution by introducing electron-vibration interactions.

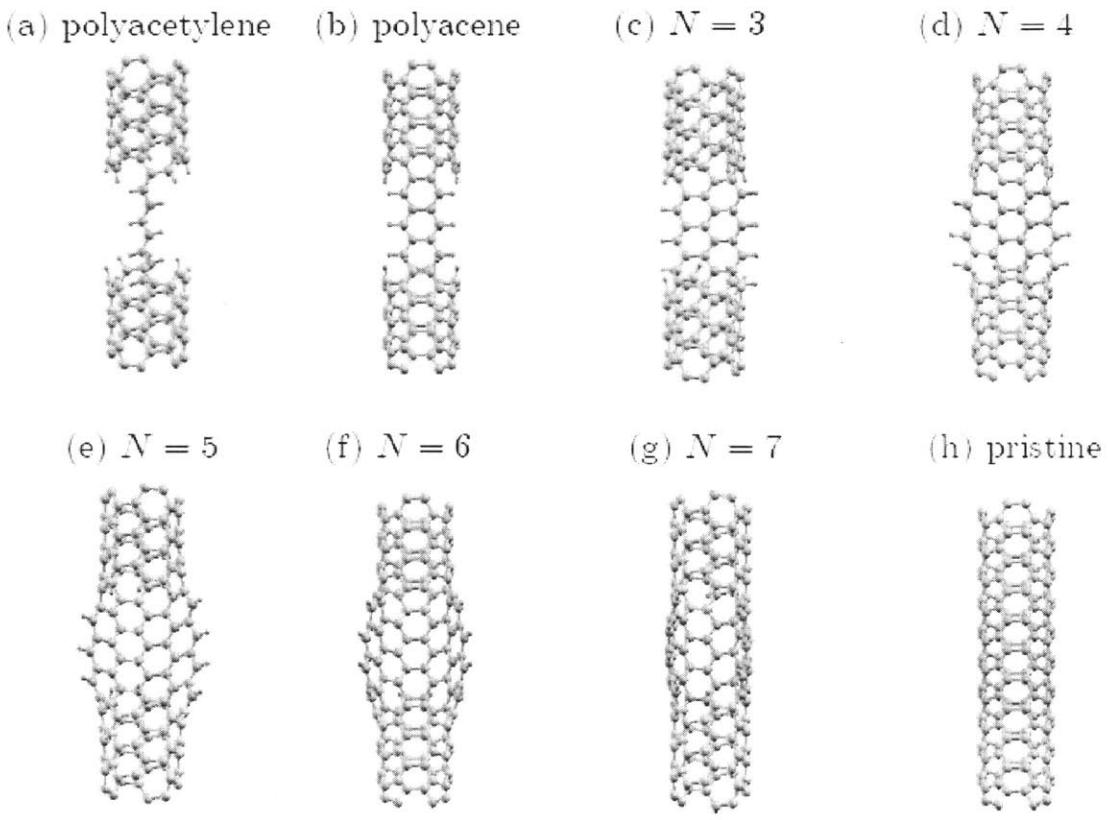

Figure 9-2: Configurations of (4, 4) CNT/ZGNR/(4, 4) CNT junctions. Starting from a single carbon chain (polyacetylene), the zigzag nanoribbon in the central region becomes wider by adding a carbon chain one by one.

9.1 CNT/ZGNR/CNT junction

Figure 9-2 shows the configurations of (4, 4) CNT/ZGNR/(4, 4) CNT junctions exploredin this study. Starting from a single 7-atom carbon chain with hydrogen terminations (i.e. polyacetylene), the ribbon is subsequenctly widened by adding other carbon chains, one by one. In this study, the number of zigzag carbon chains, N, is used in order to classify zigzag nanoribbons in the conductor region. For example, Fig. 9-1 is the (N=6) ZGNRs, according to our classification. DFT calculations are performed using the Perdew-Zunger local density approximation [75], norm-conserving pseudopotentials [95], and a plane-wave basis with a cutoff of 55 Ry.

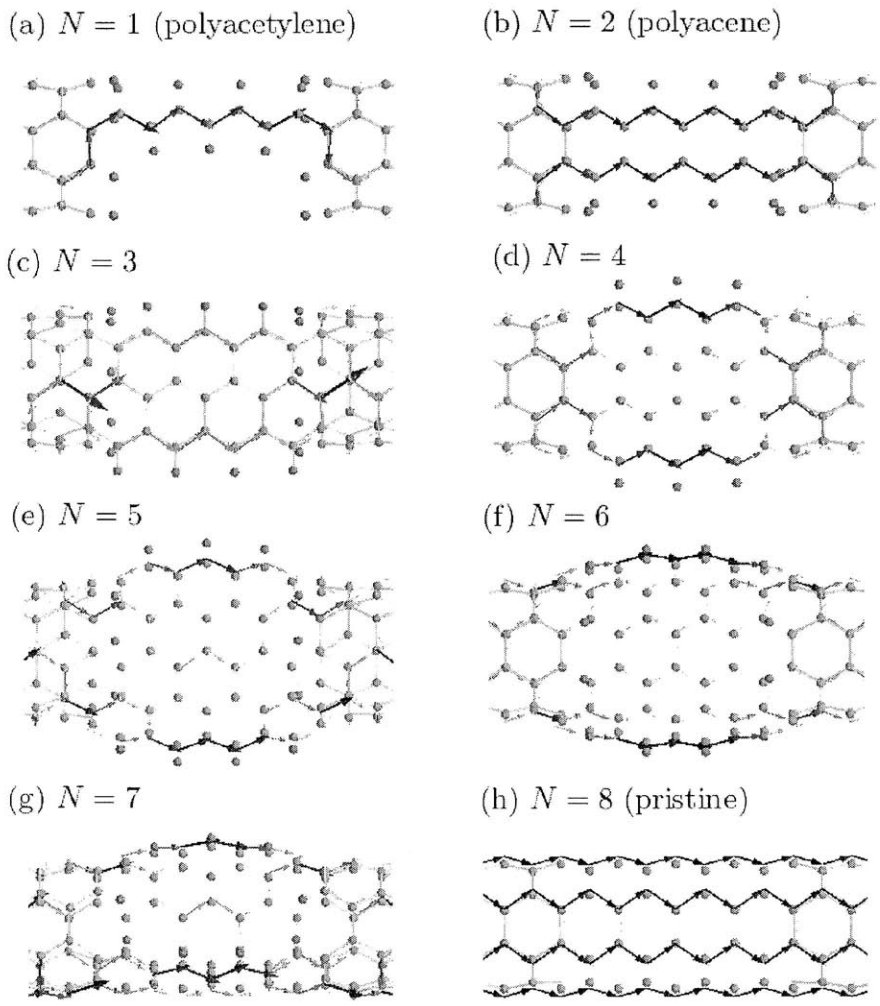

Figure 9-3: The local distribution of elastic currents through $(4, 4)$ CNT/ZGNR/$(4, 4)$ CNT junctions.

9.2 Elastic Current

Using the local current expression discussed in the previous chapter, we have first calculated the local distribution of elastic currents in the $(4, 4)$ CNT/ZGNR/$(4, 4)$ CNT junctions. Figure 9-3 shows the local elastic currents for ZGNRs from $N = 1$ to $N = 8$. The electronic properties of carbon-based materials around the Fermi energy are mainly determined by the π orbitals of the carbon atoms, it is observed that local currents mostly flow via π-type Wannier functions at carbon atoms. For polyacetylene (N=1), there is only one π-orbital bridge in the conductor region, along

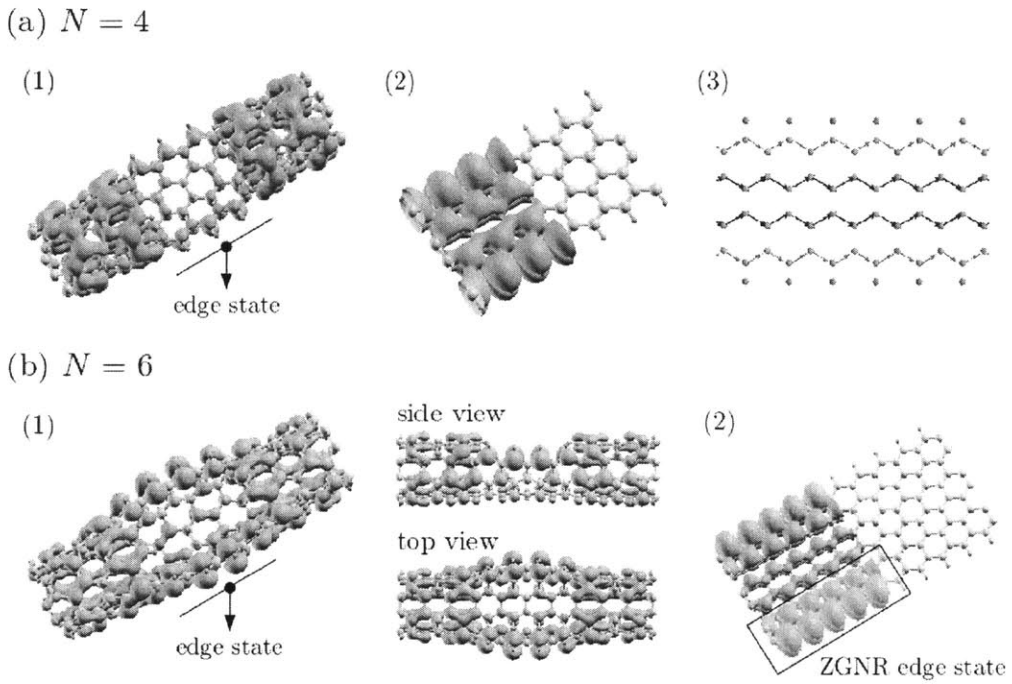

Figure 9-4: Local density of states for (a) (N=4) ZGNR and (b) (N=6) ZGNR junctions. (a)-(1): high local density of states concentrated on the outmost carbon chains of the (N=4) ZGNR junction. (a)-(2): local density of states for a pristine (N=4) ZGNR. (a)-(3): local current distribution for for a pristine (N=4) ZGNR. (b)-(1): local density of states concentrated on the outmost carbon chains of the (N=6) ZGNR junction. (b)-(2): local current distribution for for a pristine (N=6) ZGNR.

which the elastic current flows as shown in Fig. 9-3-(a). In the case of the (N=8) ZGNR junction, which is a pristine $(4, 4)$ nanotube, a homogeneous elastic current along zigzag carbon lines is observed.

9.2.1 Edge current in ZGNR

For $2 \leq N \leq 7$, most of the elastic current flows along the nanoribbon edges. Due to symmetry, the same amount of edge currents are observed for (N=even) nanoribbons, which have symmetric edges. Even for N = odd ≥ 3 nanoribbons whose edges are asymmetric, almost the same amount of current is observed at both edges. The edge current at zigzag nanoribbons agrees with the well-known fact that currents at the Fermi level flow along the edges for pristine zigzag graphene nanoribbons. The edge

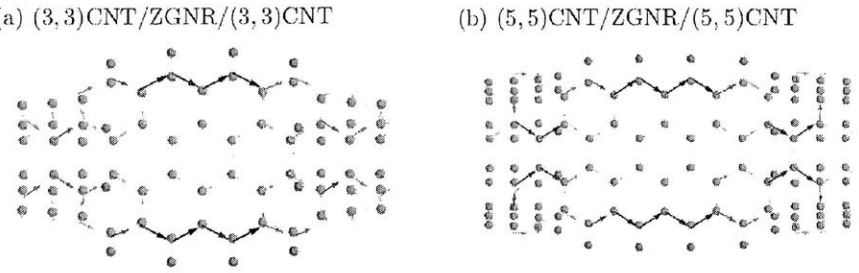

Figure 9-5: Local current distributions for the (N=4) ZGNR connected to $(3,3)$ and $(5,5)$ CNT electrodes.

state of the finite ZGNR between CNT electrodes, however, is more localized than that of a pristine infinite ZGNR. In order to see this difference, we have calculated the local density of states for both cases. Figure 9-4-(a) illustrates the isosurface of the local density of states for the $(4,4)$ CNT/(N=4) ZGNR/$(4,4)$ CNT junction and the pristine (N=4) ZGNR. While the isosurface for the pristine ZGNR spreads out over the whole region of the nanoribbon, the $(4,4)$ CNT/(N=4) ZGNR/$(4,4)$ CNT junction has a well-connected local density of states that are concentrated at the outmost single carbon chain. In fact, for very narrow zigzag nanoribbons like (N=4) ZGNR, the concept of an edge state is meaningless because the spatial dispersion of the edge state in the transverse direction is comparable to the width of the narrow nanoribbon. Moreover, as demonstrated in Fig. 9-4-(a)-(1), the elastic current for the (N=4) nanoribbon is almost uniformly distributed over the whole ribbon. In contrast, in the case of the $(4,4)$ CNT/(N=4) ZGNR/$(4,4)$ CNT junction, a sharp edge current flowing via the outmost carbon line can be generated even for a narrow zigzag nanoribbon. Similarly, Fig. 9-4-(b) illustrates the isosurfaces of the local density of states for a pristine (N=6) ZGNR and a $(4,4)$ CNT/(N=6) ZGNR/$(4,4)$ CNT junction. Just like the $(4,4)$ CNT/(N=4) ZGNR/$(4,4)$ CNT junction, an edge state localized at the outmost carbon chain is clearly formed. In contrast to the (N=4) nanoribbon, one can observe that the (N=6) nanoribbon has an edge state mostly located at the outermost benzene chain (two zigzag carbon chains).

We also checked whether this feature is observed when ZGNRs are connected to

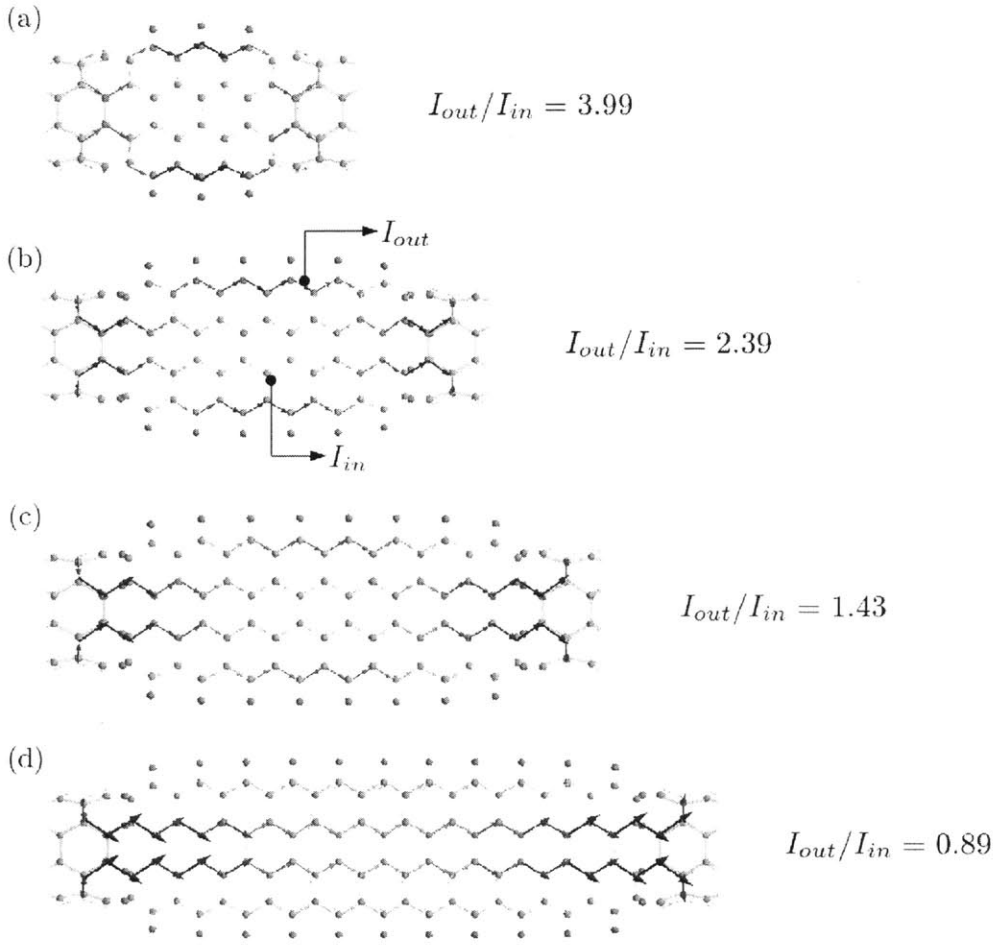

Figure 9-6: Local current distributions for $(4,4)$ CNT/(N=4) ZGNR/$(4,4)$ CNT junction with different lengths. I_{out} and I_{in} represent currents flowing along the outmost carbon chain and the inner one respectively.

smaller and larger CNT electrodes. Figure 9-5 shows the local current distributions for the (N=4) ZGNR connected to $(3,3)$ and $(5,5)$ CNT electrodes. It is clearly seen that both systems have edge currents mostly concentrated on the outermost carbon chains.

One might guess that this feature gets weaker as the length of ZGNRs in the central region increases, sine the bulk properties of the ZGNRs are recovered as the finite ZGNRs in the central region get longer. Because the current inside the ribbon is larger than the edge current for the bulk ZGNRs, as observed in Fig. 9-4-(a)-(3), A similar current distribution will be observed for a long ZGNR junction. In order to

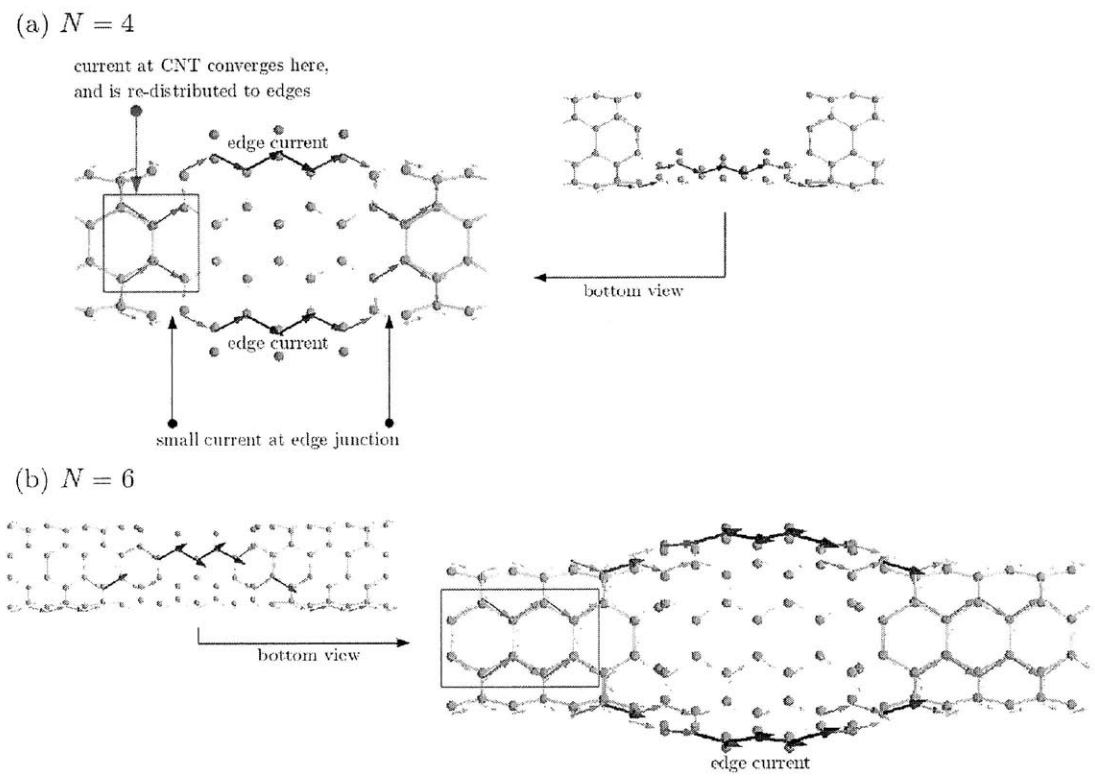

Figure 9-7: Local current distribution in the interface between the CNT electrode and the ZGNR. The elastic current from the CNT electrode converges to the central region indicated by the blue box. The current is re-distributed to the ZGNR edges.

verify this hypothesis, we have calculated local current distributions while increasing the length of the nanoribbon. In Fig. 9-6, (a), (b), (c), and (d) represent the local current distributions when the ZGNR part consists of 4, 7, 9, and 11 unit cells. When I_{out} and I_{in} denote currents flowing along the outermost carbon edge and the inner carbon line, the ratio I_{out}/I_{in} is also calculated. As the size of (N=4) ZGNR increases, the ratio I_{out}/I_{in} gets smaller and approaches that of the infinite bulk ZGNR, 0.73. In particular, for the 11-unit-cell ZGNR, the ratio I_{out}/I_{in} is smaller than unity, which means that this junction no longer has a well-localized edge current.

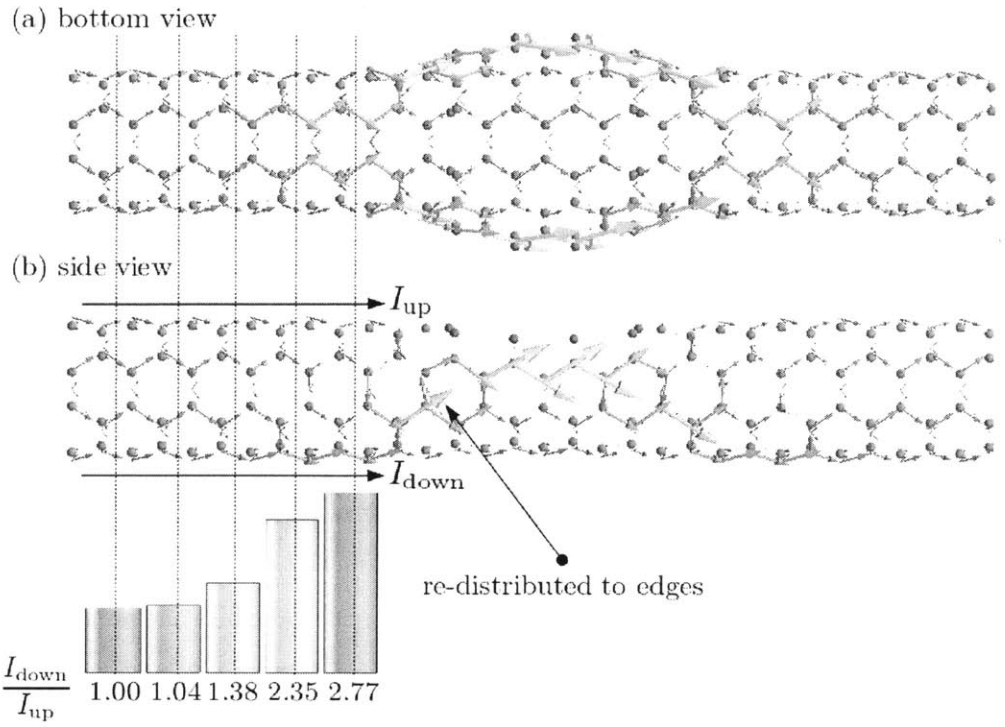

Figure 9-8: The ratio of the current in the lower region I_{down} to that in the upper region I_{up}. Deep inside the CNT electrode I_{down}/I_{up} is unity. Before entering the edges, I_{down}/I_{up} gradually increases to 2.77.

9.2.2 Current injection to edge states

Next let us focus on how the elastic current is injected into the zigzag nanoribbon in the central region. Figure 9-7 illustrates the current injection patterns at the interfaces of CNT/(N=4) ZGNR and CNT/(N=6) ZGNR. It is shown that the current at the CNT electrodes is not directly injected to the edges, but a large amount of the current from the CNT electrodes first converges to the center of the interface between the CNT and the ZGNR. Then the current is re-distributed to the edges. As seen in Fig. 9-3-(h), the elastic current is uniformly distributed deep inside the CNT electrode far away from the central region. Approaching the interface, some of the current flowing along the upper part of CNT moves to the lower part of CNT. To illustrate this, we have calculated the ratio of the lower current I_{down} to the upper current I_{up} for CNT-(N=6) ZGNR as shown in Fig. 9-8. As expected, I_{up} and I_{down} are equal inside the

CNT electrode, which is distant from the ZGNR by 5 unit cells (approximately $12\mathring{A}$). The ratio I_{down}/I_{up} gradually increases up to 2.77 before the current is distributed to the edges.

9.3 Inelastic current

On the top of the elastic transport properties investigated in the previous section, we here study the inelastic transport properties by using the *ab initio* method that we have developed throughout this work, and the expression for the local inelastic current distribution. First we calculate the derivative of the differential conductance dG/dV, which is known as the *inelastic tunneling spectroscopy signal* (IETS), for each $(4,4)$ CNT/ZGNR/$(4,4)$ CNT junction in order to find out active vibrational modes leading to conductance steps. Next we investigate how the electron-vibrational interaction changes the local current distribution.

9.3.1 Inelastic tunneling spectroscopy signal (IETS)

Figure 9-9 shows the derivative of the differential conductance dG/dV for the polyacetylene and polyacene junctions. It is observed that there are two and three large peaks for the polyacetylene and polyacene junctions, respectively. The vibrational configurations for two major peaks of the polyacetylene junction are illustrated above the dG/dV graph in Fig. 9-9. Basically, they correspond to *bond-alternating* longitudinal vibrations, which can lead to large modulations in hopping parameters between Wannier functions. While mode 108 is concentrated inside the polyacetylene, a surface vibration of the CNT electrode has a large contribution to mode 142. Compared with Fig. 9-3-(a), the surface atom vibration matches the main path of the elastic current. Conducting electrons, therefore, can have more chances to interact with local vibrations. It qualitatively explains why vibrational mode 142 leads to the largest conductance peak.

For the polyacene junction, mode 150 has transverse vibrations of the CNT surface layer, but there is no vibration inside polyacene. For mode 157, the vibration is

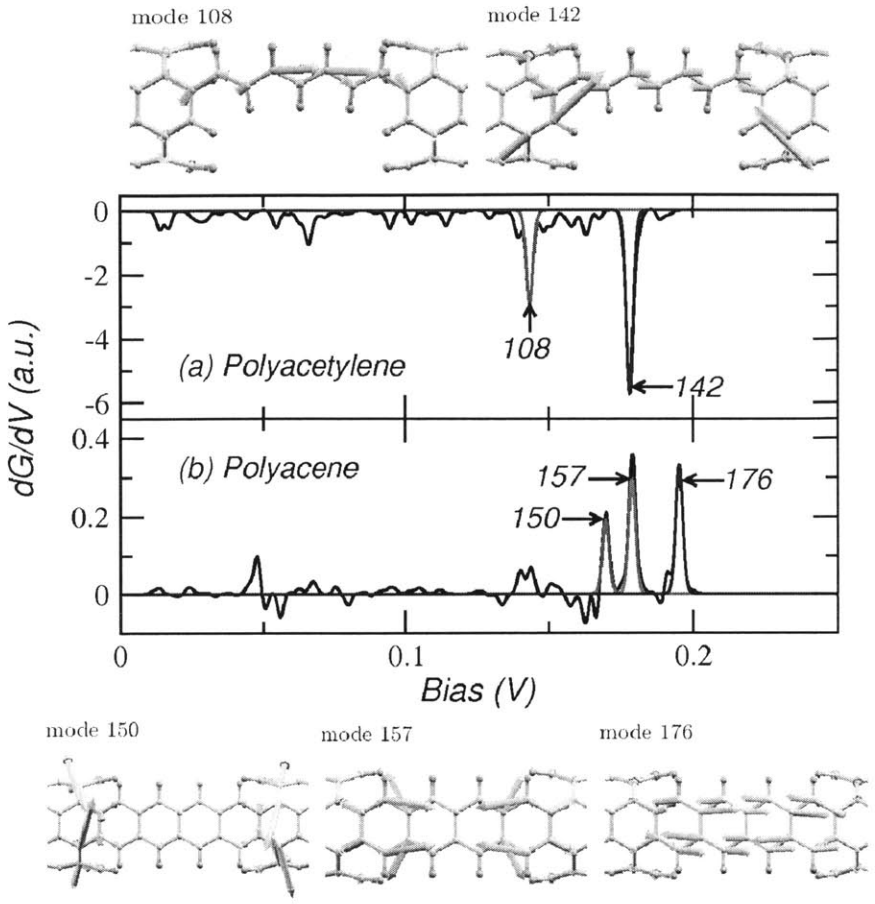

Figure 9-9: The derivative of the differential conductance dG/dV for the (a) polyacetylene and (b) polyacene junctions. The vibrational configurations for major peaks in dG/dV of the polyacetylene and the polyacene are indicated above and below the graph respectively

concentrated on the interfacial region and a part of the polyacene close to the CNT electrode. Compared with vibrational mode 150, mode 157 can be characterized more by a longitudinal vibration than a transverse one. Mode 176 shows a longitudinal stretching vibration of the polyacene.

The IETS graphs for the (N=3) to (N=7) ZGNR junctions show qualitatively similar trends to that of the polyacene junction, as shown in Fig. 9-10. Major IETS peaks occur at three bias voltages, at which the polyacene junction also has three distinct peaks: 170 meV, 185 meV, and 196 meV. These three voltage values are indicated by red, blue, and green dashed lines in Fig. 9-10.

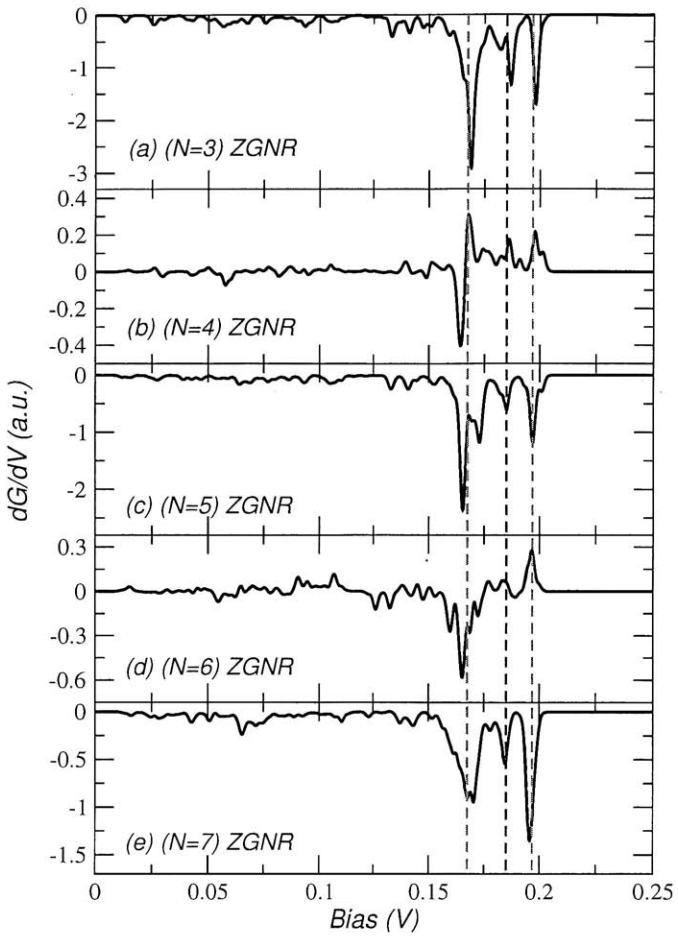

Figure 9-10: The derivative of the differential conductance dG/dV for the (N=3) to (N=7) ZGNR junctions.

Figure 9-11 illustrates some of the active vibrational modes that lead to main peaks for the (N=4) to (N=6) ZGNR junctions. The left, center, and right columns in Fig. 9-11 correspond to three main peak regions indicated by the red, blue, and green dashed lines in Fig. 9-10. The modes in the left panel, whose energies are approximately 170 meV, can be characterized by transverse vibrations whose large contributions come from the surface layer of the CNT electrode and the interface. In contrast, the modes in the right column are longitudinal stretching vibrations of the zigzag nanoribbons. Their vibrational energies are about 196 meV. The modes in the central panel show mixed behaviors of the modes in the left and right columns; for example, a mixture of longitudinal and transverse vibrations, or a combination

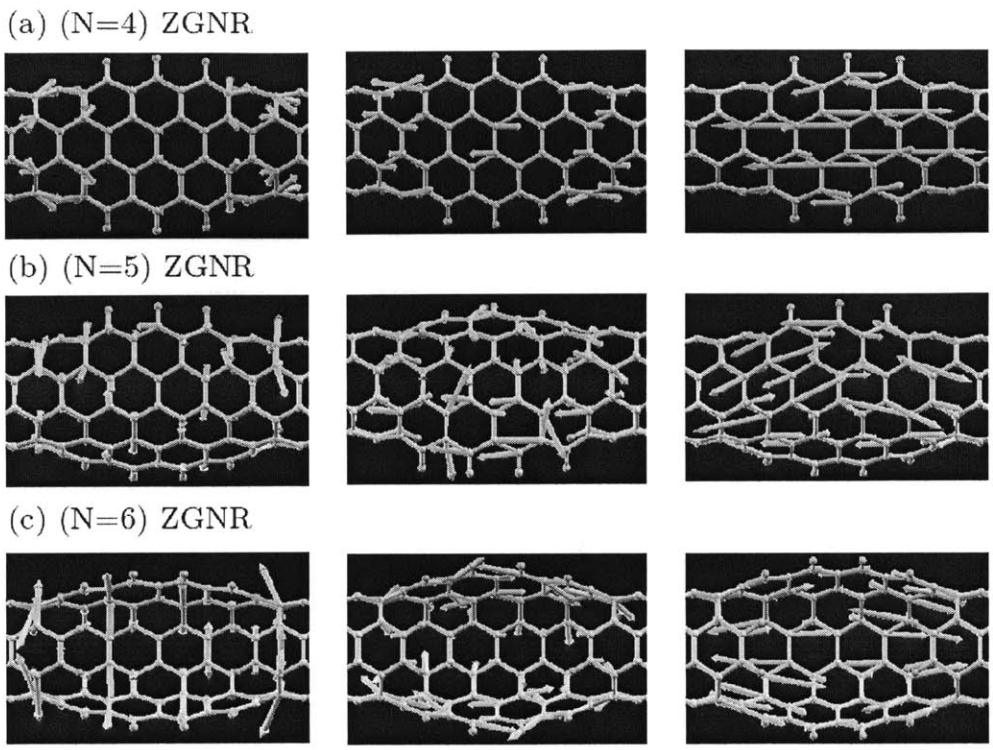

Figure 9-11: The examples of the vibrational modes for the (N=4) to (N=6) ZGNR junctions. The left, center, and right panels correspond to regions indicated by the red, blue, and green dashed lines in Fig. 9-10.

of vibrations in the surface layer and the central region. This change in vibrational configurations resembles that of the polyacene junction.

9.3.2 Local distribution of inelastic current

Although the ZGNR-CNT junctions show similar trends in IETS, the local distributions of inelastic currents are not totally similar. We have found that the local inelastic current patterns for the ZGNR-CNT junctions in our study can be categorized as two sub-groups. First, the local distributions of the inelastic current for the (N=1) to (N=4) ZGNR junctions are the same as that of the elastic current (Compare Fig. 9-3 and Fig. 9-12), apart from the current direction. Therefore the inelastic current for the (N=1) to (N=4) ZGNR junctions just enhances or diminishes the elastic current. The only difference is that one edge current is larger than

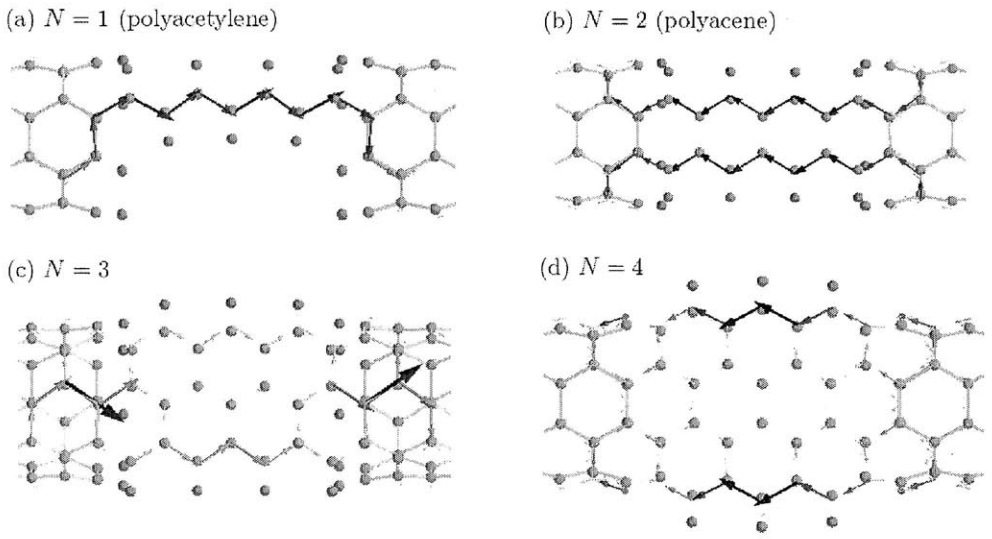

Figure 9-12: The local distributions of the inelastic current for the (N=1) to (N=4) ZGNR junctions.

the other for the (N=1) ZGNR junction, which has asymmetric edges.

In contrast to the *uni-directional* current distribution of the (N=1) to (N=4) ZGNR junctions, the inelastic currents for the (N=5) to (N=7) ZGNR junctions exhibit more complex local current patterns. The representative feature of their inelastic currents is a formation of loop currents, as seen in Fig. 9-13. The loop currents are generated inside the nanoribbon, at the CNT surface layers, or at the CNT electrodes. Moreover, the inelastic current can flow not just along edges but also through the inside of the nanoribbons. For example, the inelastic current for the (N=6) ZGNR junction flows not along the edges, but along inner carbon chains next to the edges, as indicated by black boxes in Fig. 9-13-(b).

One might guess that this sharp distinction between two sub-groups comes from a difference in the curvature of the nanoribbons (the wider nanoribbon is more bent since it has more carbon chemical bonds with the CNT electrodes). Figure 9-14 shows how much each nanoribbon junction is bent. As an indirect check on this speculation, we have performed the same current calculation on ZGNR-(3, 3) CNT junctions whose cross sections are illustrated in Fig. 9-15. First, the elastic current distributions for the ZGNR-(3, 3) CNT junctions have the same features that

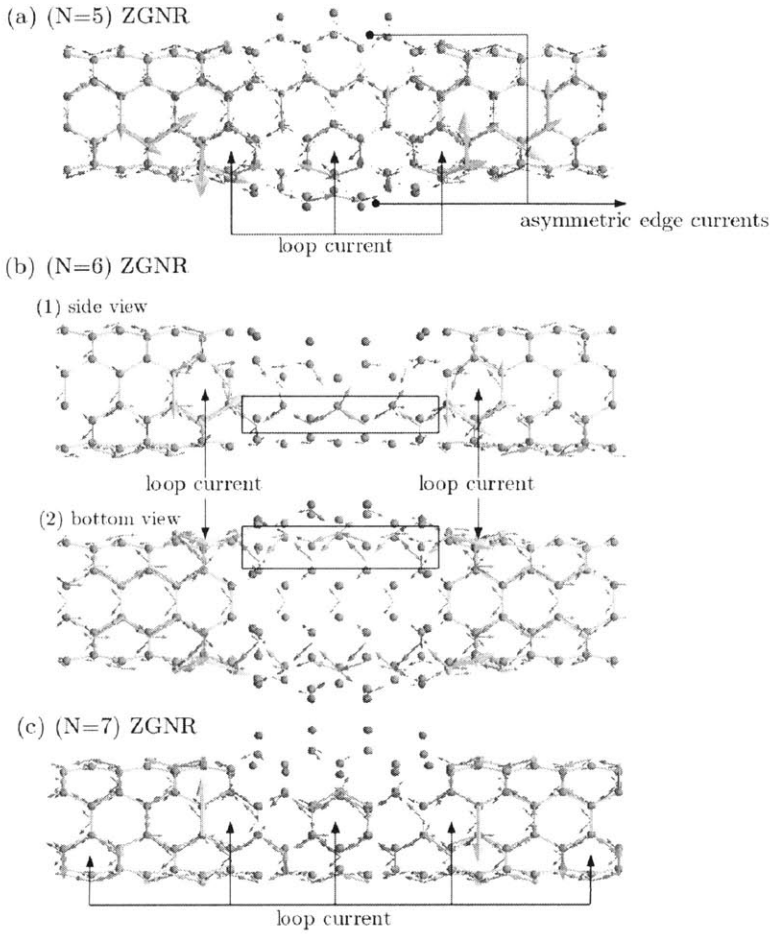

Figure 9-13: The local distributions of the inelastic current for the (N=5) to (N=7) ZGNR junctions.

we observed in the ZGNR-$(4,4)$ CNT junctions: (1) edge currents are formed at the outmost carbon chains and (2) currents first converge to the center, and are distributed to the edges (See Fig. 9-16). However, we could not find the same trend on the inelastic current distribution observed in the $(4,4)$ CNT/ZGNR/$(4,4)$ CNT junctions, and especially the curvature effect. It is true that there is a simiarity in the inelastic current distribution in comparison with the $(4,4)$ CNT/ZGNR/$(4,4)$ CNT junctions: for example, one edge carries larger inelastic current than the other for for the (N=3) and (N=5) ZGNR junctions, as illustrated in Fig. 9-17. In addition, although the loop current formation is not observed, *non-unidirectional* current is

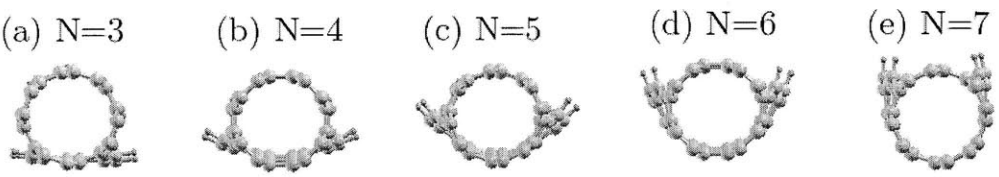

Figure 9-14: Cross sections for the (N=3) to (N=7) ZGNR connected to $(4,4)$ CNT.

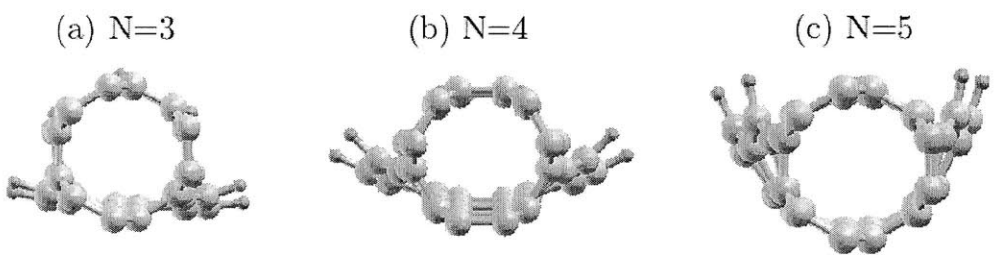

Figure 9-15: Cross sections for the (N=3) to (N=5) ZGNR connected to $(3,3)$ CNT.

locally formed in the (N=3) and (N=5) ZGNR junctions, as indicated in Fig. 9-17. The $(3,3)$ CNT/(N=4) ZGNR/$(3,3)$ CNT CNT junction, in contrast, does not possess those features, but its inelastic current distribution simply resembles that of the elastic current. This observation implies that it might not be true that the curvature effect leads to two sub-groups in the inelastic current distributions for the $(4,4)$ CNT/ZGNR/$(4,4)$ CNT junctions. It might be system-specific, but not generic. Nevertheless we have confirmed that the electron-vibration interaction can lead to more complex inelastic current distributions than elastic ones, leading, for example, to locally reversed current directions, or to the formation of loop currents observed in $(4,4)$ CNT/ZGNR/$(4,4)$ CNT junctions.

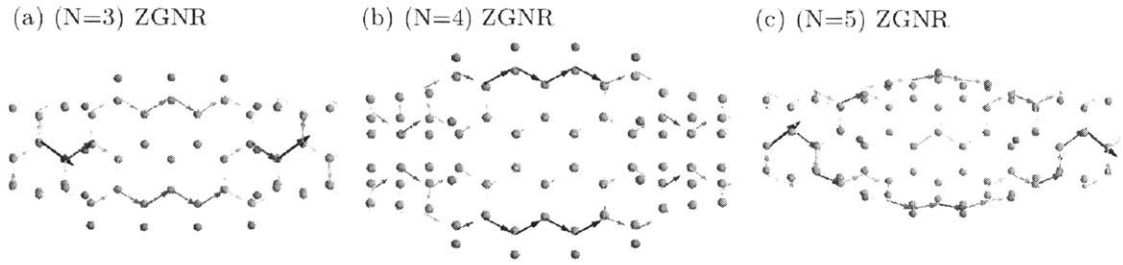

Figure 9-16: The local distribution of elastic currents through the ZGNR-$(3,3)$ CNT junctions.

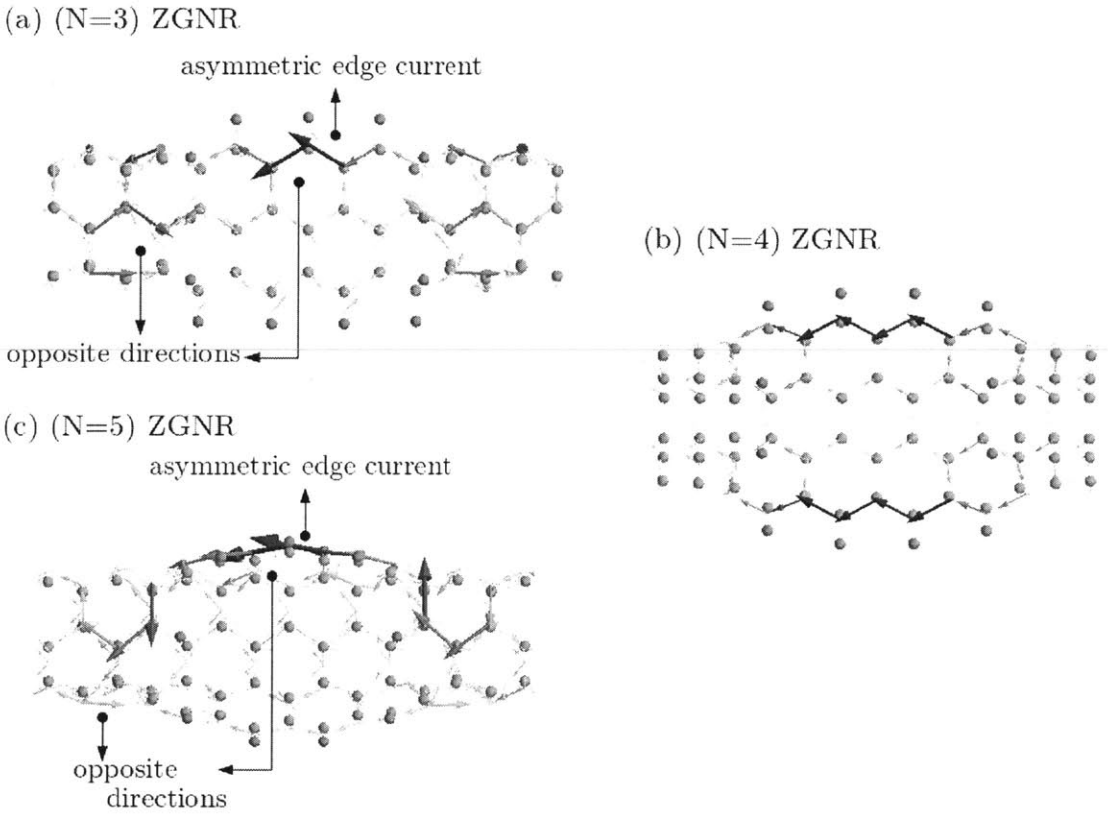

Figure 9-17: The local distribution of inelastic currents through the $(3,3)$ CNT/(N=4) ZGNR/$(3,3)$ CNT junctions.

Chapter 10

Summary

In this work we develop an *ab-initio* approach to study vibration-induced inelastic transport properties of molecular and nanoscale systems. Our method is based on planewave-based DFT calculations and the Meir-Wingreen transport formalism with non-equilibrium Green's functions. We use maximally localized Wannier functions as a localized basis set, as required for Green's function methods. Due to the exact unitary transformation between eigenstates and maximally localized Wannier functions, the accuracy of planewave-based DFT calculations can be preserved throughout the process. The electron-vibration self-energy, which captures the physics of inelastic transport, is calculated using both the lowest-order perturbative expansion and a self-consistent approach. We confirm that these two approximations can guarantee the current conservation. Furthermore, we also calculate non-equilibrium vibrational populations induced by conducting electrons, with vibrational absorption and emission rates, and decay rates to bulk phonons. These rates can be calculated within Green's function methods.

In order to test our implementation, we investigate inelastic transport properties, such as a differential conductance and its derivative with respect to a bias voltage, and nonequilibrium populations for benzene molecular junctions connected to monoatomic carbon chain (cumulene) and $(3,3)$ CNT electrodes. We observe steps in the differential conductance at the threshold bias voltage corresponding to the vibrational energies. These steps imply that new conducting channels open up by accompanying

a real emission of vibrational energy. From these signals we identify active vibrational modes that participate in opening the inelastic conduction channels. For the cumulene-benzene junction, there are five active vibrational modes, among which two out-of-plane vibrations and three in-plane ones lead to upward and downward conductance steps respectively. Using standard scattering theory, it is shown that the polarity of these conductance steps is the result of a competition between two elastic conducting channels. This multichannel effect is generic, so it is possible that upward and downward steps can be observed in any other system. By replacing the cumulene chain by the $(3,3)$ CNT electrode, we calculate the nonequilibrium vibrational populations of the benzene molecule. The decay rates of the molecular vibrations are calculated within harmonic coupling theory to bulk phonons of the CNT electrodes. It is found that some of the vibrational modes have small decaying rates. This can be qualitatively explained, considering that these modes are located outside the CNT phononic band, and are localized inside the molecule. Furthermore, some high-energy vibrational modes are found to cool down in a certain range of bias voltages, which is understood in terms of a resonant structure in the density of states around the Fermi energy. These findings are in a good agreement with other theoretical and computational works.

Next we focus on the local distribution of inelastic currents inside a molecular conductor. While the local elastic current has been theoretically studied in many nanoscale systems, it has rarely been attempted to understand how local current distributions are changed under the electron-vibration interaction. In order to answer this question, we derive an analytic expression for a correction to the local current distribution due to electron-vibration interactions using non-equilibrium field theory. By revisiting the cumulene-benzene junction, we find that out-of-plane active vibrational modes can induce a non-trivial local current distribution, different from the elastic current distributions. Unlike elastic currents flowing through π-orbitals, σ-orbitals can contribute to inelastic current paths, as well as π-orbitals. Furthermore, it is observed that the inelastic current direction is locally inverted inside the molecule and loop currents between π and σ orbitals are formed. These features differ from

the uni-directional elastic current.

Motivated by recent experimental advancements to produce narrow GNRs by unzipping CNTs, we study transport properties of CNT/ZGNR/CNT junctions using the approach we developed. In particular we focus on the local current distribution in the junctions and inelastic transport properties. First, we calculate the local distribution of the elastic current to visualize the current injection pattern from the CNT electrodes to ZGNRs and the current path inside ZGNRs. Regarding inelastic transport properties, we find that CNT/ZGNR/CNT junctions with different widths show major peaks in inelastic tunneling spectroscopy signals, at three similar bias voltages. The corresponding vibrational configurations are also qualitatively similar. When it comes to the local current distribution, it is observed that the electron-vibration interaction can lead to a complex current network such as the locally inverted current direction and the formation of loop currents, as shown in the cumulene-benzene junction.

The relevance of the method developed throughout this work can be seen from several viewpoints. First, our approach is the first attempt to combine planewave-based DFT calculation and inelastic quantum transport theory. Considering the fact that the planewave-based DFT calculation can describe electronic properties more accurately than those based on a localized orbital basis, we believe that our approach can provide accurate and reliable descriptions on transport properties of nanoscale systems. Furthermore, because it can be generalized to other types of interactions, it can act a starting point to extend the existing Wannier-based transport formalism to study various transport phenomena in the presence of other interactions.

Appendix A

Vibrational Decaying Rates

A.1 The Hamiltonian of system in the presence of a heat bath

Let us define a classical, harmonic Hamiltonian

$$\mathcal{H}_S = \sum_{i=1}^{3n} \frac{1}{2} m_i \dot{q}_i^2 + \sum_{ij} \frac{1}{2} v_{ij} q_i q_j \tag{A.1}$$

$$= \sum_{i=1}^{3n} \frac{1}{2} \dot{Q}_i \delta_{ij} \dot{Q}_j + \sum_{ij} \frac{1}{2} Q_i V_{ij} Q_j, \tag{A.2}$$

where $Q_i \equiv \sqrt{m_i} q_i$ and $V_{ij} \equiv v_{ij}/\sqrt{m_i m_j}$. The normal modes and its eigen-frequencies are determined by solving the eigenvalue equation

$$V \vec{X}_i = \omega_i^2 \vec{X}_i. \tag{A.3}$$

In the normal mode representation, the Hamiltonian becomes

$$\mathcal{H}_S = \frac{1}{2} \dot{Q}^T X X^T \dot{Q} + \frac{1}{2} Q^T X \left[\omega_i^2 \delta_{ij}\right] X^T Q \tag{A.4}$$

$$= \frac{1}{2} \dot{\tilde{Q}}^T \dot{\tilde{Q}} + \frac{1}{2} \tilde{Q}^T \left[\omega_i^2 \delta_{ij}\right] \tilde{Q}, \tag{A.5}$$

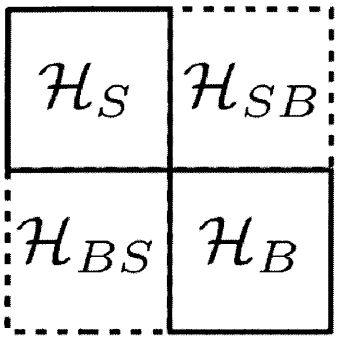

Figure A-1: Schematic diagram of system and heat bath Hamiltonians. Two parts are coupled via $\mathcal{H}_{BS} = \mathcal{H}_{SB}^{\dagger}$.

where

$$Q = \begin{bmatrix} Q_1 \\ Q_2 \\ \vdots \\ Q_{3n} \end{bmatrix} \tag{A.6}$$

$$X = \begin{bmatrix} | & | & & | \\ \vec{X}_1 & \vec{X}_2 & \cdots & \vec{X}_{3n} \\ | & | & & | \end{bmatrix} \tag{A.7}$$

$$\tilde{Q} = X^T Q. \tag{A.8}$$

By defining the annihilation and creation operators as

$$b_i = \sqrt{\frac{\omega_i}{2\hbar}}\tilde{Q}_i + i\sqrt{\frac{1}{2\hbar\omega_i}}\tilde{P}_i \tag{A.9}$$

$$b_i^{\dagger} = \sqrt{\frac{\omega_i}{2\hbar}}\tilde{Q}_i - i\sqrt{\frac{1}{2\hbar\omega_i}}\tilde{P}_i, \tag{A.10}$$

where $\tilde{P}_i = \dot{\tilde{P}}_i$, the system Hamiltonian is written in terms of harmonic oscillators:

$$\mathcal{H}_S = \sum_{i=1}^{3n} \hbar\omega_i \left(b_i^{\dagger} b_i + \frac{1}{2} \right). \tag{A.11}$$

Likewise, the heat-bath Hamiltonian reads

$$\mathcal{H}_B = \sum_{j=1}^{3N} \hbar\bar{\omega}_k \left(c_j^\dagger c_j + \frac{1}{2} \right). \tag{A.12}$$

Note that the bar is used to distinguish quantities for the heat bath and those for the system. The coupling Hamiltonian can also be written in the second-quantized normal mode representation,

$$\begin{aligned}
\mathcal{H}_{BS} + \mathcal{H}_{SB} &= \sum_{i}^{3n} \sum_{j}^{3N} u_{ij} q_i \bar{q}_j && \text{(A.13)} \\
&= \sum_{i}^{3n} \sum_{j}^{3N} U_{ij} Q_i \bar{Q}_j && \text{(A.14)} \\
&= \sum_{k} \sum_{m} \left(\sum_{i,j} U_{ij} X_{ik} \bar{X}_{jm} \right) \tilde{Q}_k \tilde{\bar{Q}}_m && \text{(A.15)} \\
&= \sum_{k} \sum_{m} \left(\sum_{i,j} U_{ij} X_{ik} \bar{X}_{jm} \right) \sqrt{\frac{\hbar}{2\omega_k}} \sqrt{\frac{\hbar}{2\omega_m}} \left(b_k + b_k^\dagger \right) \left(c_m + c_m^\dagger \right), && \text{(A.16)}
\end{aligned}$$

where $U_{ij} \equiv u_{ij}/\sqrt{m_i \bar{m}_j}$ is the mass-renormalized interatomic force constant between the system and the heat bath.

A.2 Decay rates

The decay rates of the kth local vibration in the system into the heat reservoir may be calculated using Fermi golden rule:

$$\Gamma_{k \to \text{bath}} = \frac{2\pi}{\hbar} \sum_{m \in \text{bath}} |{}_B\langle m | \mathcal{H}_C | k \rangle_S|^2 \, \delta \left(\hbar\bar{\omega}_m - \hbar\omega_k \right), \tag{A.17}$$

Using Eq.(A.16), it becomes

$$\Gamma_{k\to\text{bath}} = \frac{2\pi}{4}\sum_{m\in\text{bath}}\left(\sum_{i,j}U_{ij}X_{ik}\bar{X}_{jm}\sum_{l,n}U_{ln}X_{lk}\bar{X}_{nm}\right)\frac{1}{\omega_k^2}\delta\left(\bar{\omega}_m-\omega_k\right) \quad \text{(A.18)}$$

$$= \frac{2\pi}{4}\sum_{i,l}X_{ik}\left(\sum_{j,n}U_{ij}U_{ln}\sum_{m\in\text{bath}}\bar{X}_{jm}\bar{X}_{nm}\right)X_{lk}\frac{1}{\omega_k^2}\delta\left(\bar{\omega}_m-\omega_k\right) \quad \text{(A.19)}$$

Here the following relation holds:

$$\sum_m\frac{1}{\omega_k}\bar{X}_{jm}\delta(\omega_k-\bar{\omega}_m)\bar{X}_{nm} = -\frac{2}{\pi}\text{Im}\left[\frac{1}{(\omega_k+i0^+)^2-\mathcal{H}_B}\right]_{jn}. \quad \text{(A.20)}$$

This can be proved by diagonalizing the heat-bath Green's function $1/\left[(\omega_k+i0^+)^2-\mathcal{H}_B\right]$:

$$\text{Im}\left[\frac{1}{(\omega_k+i0^+)^2-\mathcal{H}_B}\right]_{jn} = \text{Im}\sum_m\bar{X}_{jm}\frac{1}{(\omega_k+i0^+)^2-\bar{\omega}_m^2}\bar{X}^T_{mn} \quad \text{(A.21)}$$

$$= \text{Im}\sum_m\frac{1}{2\bar{\omega}_m}\bar{X}_{jm}\left(\frac{1}{\omega_k+i0^+-\bar{\omega}_m}-\frac{1}{\omega_k+i0^+-\bar{\omega}_m}\right)\bar{X}^T_{mn} \quad \text{(A.22)}$$

$$= -\frac{\pi}{2}\sum_m\bar{X}_{jm}\bar{X}_{nm}\frac{1}{\bar{\omega}_m}\delta(\omega_k-\bar{\omega}_m) \quad \text{(A.23)}$$

Therefore the decaying rate is

$$\Gamma_{k\to\text{bath}} = -\frac{1}{\omega_k}\vec{X}_k^T\left[U\text{Im}G_B^r(\omega_k)U^\dagger\right]\vec{X}_k, \quad \text{(A.24)}$$

where $G_B^r = \frac{1}{(\omega_k+i0^+)^2-\mathcal{H}_B}$.

Appendix B

Derivation of Eq.(8.17)

The lesser Green's function in the vibronic contribution I^{vib}_{mn},

$$\frac{i}{\hbar}\left\langle \left(b_\lambda + b^\dagger_\lambda\right) c^\dagger_j c_i \right\rangle (\tau) = \lim_{\tau\to\tau'} G^<_{i,\lambda j}(\tau,\tau') \tag{B.1}$$

is calculated up to the first order of the electron-vibration interaction $\mathcal{M}^\lambda$. This can be obtained in two ways: (1) the $\mathcal{S}$-matrix expansion and (2) the equation of motion technique.

B.1 $\mathcal{S}$-matrix expansion

When the operators in $G_{i,\lambda j}(\tau,\tau')$ are written in the interaction picture with respect to the free-particle Hamiltonian $\mathcal{H}_0 = \sum_i \varepsilon_i c^\dagger_i c_i + \sum_{i\neq j} V_{ij} c^\dagger_i c_j$, $G_{i,\lambda j}(\tau,\tau')$ becomes

$$\begin{aligned} G_{i,\lambda j}(\tau,\tau') &= -\frac{i}{\hbar}\left\langle \mathcal{T}_c \left\{ c_i(\tau)\left(b_\lambda + b^\dagger_\lambda\right)(\tau') c^\dagger_j(\tau') \right\} \right\rangle \\ &= -\frac{i}{\hbar}\left\langle \mathcal{T}_c \left\{ \mathcal{S}\bar{c}_i(\tau)\left(\bar{b}_\lambda + \bar{b}^\dagger_\lambda\right)(\tau') \bar{c}^\dagger_j(\tau') \right\} \right\rangle, \end{aligned} \tag{B.2}$$

where

$$\mathcal{S} = e^{-\frac{i}{\hbar}\int_c dt \bar{\mathcal{H}}'(t)} e^{-\frac{i}{\hbar}\int_c dt \bar{\mathcal{H}}^i(t)} \tag{B.3}$$

$$\approx e^{-\frac{i}{\hbar}\int_c dt \bar{\mathcal{H}}'(t)} \left(1 - \frac{i}{\hbar}\int_c dt \bar{\mathcal{H}}^i(t) + \mathcal{O}(\mathcal{M}^2)\right), \tag{B.4}$$

where the bar on the operators indicates that the operators are written in the interaction picture with respect to $\mathcal{H}_0$. Here $\bar{\mathcal{H}}^i(t)$ is the electron-vibration interaction, and $\bar{\mathcal{H}}'$ is the coupling Hamiltonian to the electrodes, which drives the device out of equilibrium.

The zeroth order term is

$$G^{(0)}_{i,\lambda j}(\tau,\tau') = -\frac{i}{\hbar}\left\langle \mathcal{T}_c\left\{c_i(\tau)\left(b_\lambda + b^\dagger_\lambda\right)(\tau')c^\dagger_j(\tau')\right\}\right\rangle_0 \tag{B.5}$$

$$= -\frac{i}{\hbar}\left\langle \mathcal{T}_c\left\{c_i(\tau)c^\dagger_j(\tau')\right\}\right\rangle_0 \left\langle\left(b_\lambda + b^\dagger_\lambda\right)\right\rangle_0, \tag{B.6}$$

where the subscript 0 indicates that the operators are written in the Heisenberg picture with respect to the non-interacting Hamiltonian $\mathcal{H}_0 + \mathcal{H}'$. In the last line the fact that electrons and vibrations are decoupled in the zeroth order is used. Since $\left\langle\left(b_\lambda + b^\dagger_\lambda\right)\right\rangle_0 = 0$, $G^{(0)}_{i,\lambda j}(\tau,\tau')$ vanishes. Thus nontrivial terms start at the next order:

$$\begin{aligned} G_{i,\lambda j}(\tau,\tau') \approx & \left(-\frac{i}{\hbar}\right)^2 \int_c dt \sum_{\lambda'}\sum_{mn} \mathcal{M}^{\lambda'}_{mn} \\ & \times \left\langle \mathcal{T}_c\left\{\left(b_{\lambda'} + b^\dagger_{\lambda'}\right)(t)c^\dagger_m(t)c_n(t)\right.\right. \\ & \left.\left.\times\, c_i(\tau)\left(b_\lambda + b^\dagger_\lambda\right)(\tau')c^\dagger_j(\tau')\right\}\right\rangle_0 \end{aligned} \tag{B.7}$$

$$\begin{aligned} = & \left(-\frac{i}{\hbar}\right)^2 \int_c dt \sum_{\lambda'}\sum_{mn} \mathcal{M}^{\lambda'}_{mn} \\ & \times \left\langle \mathcal{T}_c\left\{c^\dagger_m(t)c_n(t)c_i(\tau)c^\dagger_j(\tau')\right\}\right\rangle_0 \\ & \times \left\langle \mathcal{T}_c\left\{\left(b_{\lambda'} + b^\dagger_{\lambda'}\right)(t)\left(b_\lambda + b^\dagger_\lambda\right)(\tau')\right\}\right\rangle_0. \end{aligned} \tag{B.8}$$

Using Wick's theorem[77], the four-point function is expanded in terms of two-point propagators:

$$\begin{aligned} \left\langle \mathcal{T}_c\left\{c^\dagger_m(t)c_n(t)c_i(\tau)c^\dagger_j(\tau')\right\}\right\rangle_0 = & (i\hbar)^2 G_{0,im}(\tau,t)\,G_{0,nj}(t,\tau') \\ & -(i\hbar)^2 G_{0,nm}(t,t)\,G_{0,ij}(\tau,\tau'), \end{aligned} \tag{B.9}$$

where $G_{0,ij}(\tau,\tau') = -\frac{i}{\hbar}\left\langle \mathcal{T}_c\left\{c_i(\tau)c_j^\dagger(\tau')\right\}\right\rangle_0$

Therefore it is concluded that

$$\begin{aligned} G_{i,\lambda j}(\tau,\tau') &\approx i\hbar\int_c dt\sum_{mn}\mathcal{M}^{\lambda}_{mn}\left[G_{0,im}(\tau,t)\,G_{0,nj}(t,\tau')\right. \\ &\quad \left. -2G_{0,nm}(t,t)\,G_{0,ij}(\tau,\tau')\right]D_\lambda(t,\tau'), \end{aligned} \tag{B.10}$$

where

$$D_\lambda(t,\tau') = -\frac{i}{\hbar}\left\langle \mathcal{T}_c\left\{\left(b_{\lambda'}+b_{\lambda'}^\dagger\right)(t)\left(b_\lambda+b_\lambda^\dagger\right)(\tau')\right\}\right\rangle_0. \tag{B.11}$$

Note that the factor two accounts for the spin degree of freedom. By applying Langreth's rule for analytic continuation to the contour-ordered Green's function[33, 77], one can obtain Eq.(8.17).

B.2 Equation-of-motion technique

Equation (8.17) can be obtained alternatively by using the equation-of-motion[77]. Taking a time derivative with respect to τ on $G_{i,\lambda j}(\tau,\tau')$, one might obtain the equation of motion for τ on $G_{i,\lambda j}(\tau,\tau')$:

$$\begin{aligned} \sum_l\left(i\frac{\partial}{\partial\tau}\delta_{il}-V_{il}\right)G_{l,\lambda j} &= \delta_c(\tau-\tau')\,\delta_{ij}\left\langle b_\lambda+b_\lambda^\dagger\right\rangle \\ &\quad +\sum_l\int_c d\tau_1\Sigma_{il}(\tau,\tau_1)\,G_{l,\lambda j}(\tau_1,\tau') \\ &\quad +\sum_{l,\lambda'}\mathcal{M}^{\lambda'}_{il}G_{l\lambda',\lambda j}(\tau,\tau') \end{aligned} \tag{B.12}$$

where $\delta_c(\tau-\tau')$ is defined as

$$\delta_c(\tau-\tau') = \begin{cases} \delta(\tau-\tau') & \tau,\tau'\in\text{forward time branch} \\ -\delta(\tau-\tau') & \tau,\tau'\in\text{backward time branch} \\ 0 & \text{otherwise.} \end{cases} \tag{B.13}$$

In energy space, the equations of motion for the retarded and lesser parts are

$$\begin{aligned}\sum_l \left(\varepsilon\delta_{il} - V_{il}\right) G^r_{l,\lambda j} &= \left\langle b_\lambda + b^\dagger_\lambda \right\rangle \delta_{ij} \\ &\quad + \sum_l \Sigma^r_{il} G^r_{l,\lambda j} + \sum_{l,\lambda'} \mathcal{M}^{\lambda'}_{il} G^r_{l\lambda',\lambda j},\end{aligned} \tag{B.14}$$

and

$$\sum_l \left(\varepsilon\delta_{il} - V_{il} - \Sigma^r_{il}\right) G^<_{l,\lambda j} = \sum_l \Sigma^<_{il} G^a_{l,\lambda j} + \sum_{l,\lambda'} \mathcal{M}^{\lambda'}_{il} G^<_{l\lambda',\lambda j}. \tag{B.15}$$

Using Eq.(B.14), Eq.(B.15) is further shown to be

$$\begin{aligned}G^<_{i,\lambda j} &= \left\langle b_\lambda + b^\dagger_\lambda \right\rangle G^<_{0,ij} \\ &\quad + \sum_{\lambda'} \sum_{m,n} G^<_{0,im} \mathcal{M}^{\lambda'}_{mn} G^a_{n\lambda',\lambda j} \\ &\quad + \sum_{\lambda'} \sum_{m,n} G^r_{0,im} \mathcal{M}^{\lambda'}_{mn} G^<_{n\lambda',\lambda j}.\end{aligned} \tag{B.16}$$

$G^{a,<}_{n\lambda',\lambda j}$ and $\left\langle b_\lambda + b^\dagger_\lambda \right\rangle$ are calculated to the zeroth and first order of $\mathcal{M}^\lambda$ respectively First, since $i\hbar\frac{d}{dt}\langle b_\lambda(t)\rangle = 0$ for the steady state, one finds

$$\left\langle b_\lambda + b^\dagger_\lambda \right\rangle = \frac{i2}{\hbar\omega_\lambda} \sum_{ij} \mathcal{M}^\lambda_{ij} \int \frac{d\varepsilon}{2\pi} G^<_{0,ij}(\varepsilon) \tag{B.17}$$

$$= -i \sum_{ij} \mathcal{M}^\lambda_{ij} \int \frac{d\varepsilon}{2\pi} G^<_{0,ij}(\varepsilon) D^a_\lambda(0). \tag{B.18}$$

Second, Green's functions can be calculated as follows:

$$\begin{aligned} G^{<}_{i\lambda',\lambda j}(\varepsilon) &= \int_{-\infty}^{\infty} dt e^{i\varepsilon t/\hbar} i \left\langle Q_\lambda c_j^\dagger Q_{\lambda'}(t) c_i(t) \right\rangle \\ &\approx \int_{-\infty}^{\infty} dt e^{i\omega t/\hbar} i \left\langle Q_\lambda Q_{\lambda'}(t) \right\rangle \left\langle c_j^\dagger c_i(t) \right\rangle \\ &= \delta_{\lambda,\lambda'} \left[G^{<}_{0,ij}\left(\varepsilon - \hbar\omega_\lambda\right) n_\lambda + G^{<}_{0,ij}\left(\varepsilon + \hbar\omega_\lambda\right)\left(n_\lambda + 1\right) \right] \\ &= \delta_{\lambda,\lambda'} i \int_{-\infty}^{\infty} \frac{d\varepsilon'}{2\pi} D^{<}_{\lambda}(\varepsilon') G^{<}_{0,ij}(\varepsilon - \varepsilon'), \end{aligned} \tag{B.19}$$

where $Q_\lambda \equiv b_\lambda + b_\lambda^\dagger$.

$$\begin{aligned} G^{a}_{i\lambda',\lambda j}(\varepsilon) &= \int_{-\infty}^{\infty} dt e^{i\varepsilon t/\hbar} \theta(-t) \left[G^{<}_{i\lambda',\lambda j}(t) - G^{>}_{i\lambda',\lambda j}(t) \right] \\ &\approx i \int_{-\infty}^{0} dt e^{i\varepsilon t/\hbar} \Big[\left\langle Q_\lambda Q_{\lambda'}(t) \right\rangle \left\langle c_j^\dagger c_i(t) \right\rangle \\ &\quad + \left\langle Q_{\lambda'}(t) Q_\lambda \right\rangle \left\langle c_i(t) c_j^\dagger \right\rangle \Big] \end{aligned} \tag{B.20}$$

$$\begin{aligned} &= \delta_{\lambda,\lambda'} \int_{-\infty}^{0} dt e^{i\varepsilon t/\hbar} \left(e^{i\omega_\lambda t} - e^{-i\omega_\lambda t} \right) G^{<}_{0,ij}(t) \\ &\quad + e^{i(\varepsilon+\omega_\lambda)t} n_\lambda G^{a}_{0,ij}(t) + e^{i(\varepsilon-\omega_\lambda)t} \left(n_\lambda + 1\right) G^{a}_{0,ij}(t) \end{aligned} \tag{B.21}$$

$$\begin{aligned} &= \delta_{\lambda,\lambda'} \int_{-\infty}^{\infty} i \frac{d\varepsilon'}{2\pi} G^{<}_{0,ij}(\varepsilon - \varepsilon') D^{a}_{\lambda}(\varepsilon') \\ &\quad + G^{a}_{0,ij}(\varepsilon - \varepsilon') D^{>}_{\lambda}(\varepsilon') \end{aligned} \tag{B.22}$$

Inserting Eq.(B.18), (B.19), and (B.22) into Eq.(B.16), one can recover Eq.(8.17).

Bibliography

[1] N. Agrait, A. L. Yeyati, and J. M. vanRuitenbeek. *Phys. Rep.*, 377:81, 2003.

[2] Elise Y. Li and. *ACS Nano, to be published.*

[3] A. Aviram and M. A. Ratner. *Chem. Phys. Lett.*, 29:277, 1974.

[4] S. Baroni, S. de Gironcoli, A. Dal Corso, and P. Giannozzi. *Rev. Mod. Phys.*, 73:515, 2001.

[5] C. Berge, Z. Song, X. Li, X. Wu, N. Brown, C. Naud, D. Mayou, T. Li, J. Hass, A. N. Marchenkov, E. H. Conrad, P. N. First, and W. A. de Heer. *Science*, 312:1191, 2006.

[6] M. Born and J. R. Oppenheimer. *Ann. Physik*, 84:457, 1927.

[7] F. Börrnert, C. Börrnert, S. Gorantla, X. Liu, A. Bachmatiuk, J.-O. Joswig, F. R. Wagner, F. Schäffel, J. H. Warner, R. Schönfelder, B. Rellinghaus, T. Gemming, J. Thomas, M. Knupfer, B. Büchner, and M. H. Rümmeli. *Phys. Rev. B*, 81:085439, 2010.

[8] M. Brandbyge, J.-L. Mozos, P. Ordejón, J. Taylor, and K. Stokbro. *Phys. Rev. B*, 65:165401, 2002.

[9] H. Bruus and K. Flensberg. *Many-Body Quantum Theory in Condensed Matter Physics.* Oxford University Press, New York, 2004.

[10] L. C. Campos, V. R. Manfrinato, J. D. Sanchez-Yamagishi, J. Kong, and P. Jarillo-Herrero. *Nano Lett.*, 9:2600, 2009.

[11] J. Campos-Delgado, J. M. Romo-Herrera, X. Jia, D. A. Cullen, H. Muramatsu, Y.-A. Kim, T. Hayashi, Z. Ren, D. J. Smith, Y. Okuno, T. Ohba, H. Kanoh, K. Kaneko, M. Endo, H. Terrones, M. S. Dresselhaus, and M. Terrones. *Nano Lett.*, 8:2773, 2008.

[12] A. G. Cano-Marquez, F. J. Rodrguez-Macias, J. Campos-Delgado, C. G. Espinosa-Gonzalez, F. Tristan-Lopez, D. Ramrez-Gonzalez, D. A. Cullen, D. J. Smith, M. Terrones, and Y. I. Vega-Cantu. *Nano Lett.*, 9:1527, 2009.

[13] D. M. Ceperley and B. J. Alder. *Phys. Rev. Lett.*, 45:566, 1980.

[14] J. Chen, M. A. Reed, A. M. Rawlett, and J. M. Tour. *Science*, 286:1550, 1999.

[15] Y. C. Chen, M. Zwolack, and M. Di Ventra. *Nano Lett.*, 3:1691, 2003.

[16] Y. C. Chen, M. Zwolack, and M. Di Ventra. *Nano Lett.*, 4:1709, 2004.

[17] Y. C. Chen, M. Zwolack, and M. Di Ventra. *Nano Lett.*, 5:621, 2005.

[18] L. Ci, Z. Xu, L. Wang, W. Gao, F. Ding, K. F. Kelly, B. I. Yakobson, and P. M. Ajayan. *Nano Res.*, 1:116, 2008.

[19] P. S. Cornaglia, H. Ness, and D. R. Grempel. *Phys. Rev. Lett.*, 93:147201, 2004.

[20] A. Cresti, R. Farchioni, G. Grosso, and G. P. Parravicini. *Phys. Rev. B*, 68:075306, 2003.

[21] A. Cresti, G. Grosso, and G. P. Parravicini. *Phys. Rev. B*, 69:233313, 2004.

[22] S. Datta. chapter 3.2. Cambridge University Press, Cambridge University Press, 1995.

[23] S. S. Datta, D. R. Strachan, S. M. Khamis, and A. T. C.e Johnson. *Nano Lett.*, 8:1912, 2008.

[24] John H. Davies, Selman Hershfield, Per Hyldgaard, and John W. Wilkins. *Phys. Rev. B*, 47:4603, 1993.

[25] D. Djukic, K. S. Thygesen, C. Untiedt, R. H. M. Smit, K. W. Jacobsen, and J. M. van Ruitenbeek. *Phys. Rev. B*, 71:161402(R), 2005.

[26] D. S. Fisher and P. A. Lee. *Phys. Rev. B*, 23:6851, 1981.

[27] T. Frederiksen, M. Paulsson, M. Brandbyge, and A.-P. Jauho. *Phys. Rev. B*, 75:205413, 2007.

[28] M. Galperin, A. Nitzan, and M. A. Ratner. *Phys. Rev. B*, 73:045314, 2006.

[29] M. Galperin, M. A. Ratner, and A. Nitzan. *J. Phys: Condens. Matter*, 19:103201, 2007.

[30] X. Guo, J. P. Small, J. E. Klare, Y. Wang, M. S. Purewal, I. W. Tam, B. H. Hong, R. Caldwell, L. Huang, S. O'brien, J. Yan, R. Breslow, S. J. Wind, J. Hone, P. Kim, and C. Nuckolls. *Science*, 311:356, 2006.

[31] D. R. Hamann, M. Schlüter, and c. Chiang. *Phys. Rev. Lett.*, 43:1494, 1979.

[32] M. Y. Han, B. Özyilmaz, Y. Zhang, and P. Kim. *Phys. Rev. Lett.*, 98:206805, 2007.

[33] H. Haug and A.-P. Jauho. *Quantum Kinetics in Transport and Optics of Semiconductors*. Springer, 1996.

[34] F. Haupt, T. Novotny, and W. Belzig. *Phys. Rev. B*, 82:165441, 2010.

[35] J. Hihath, C. R. Arroyo, G. Rubio-Bollinger, N. Tao, and N. Agraït. *Nano. Lett.*, 8:1673, 2008.

[36] J. Hihath, C. Bruot, and N. Tao. *ACSNano*, 4:3823, 2010.

[37] P. Hohenberg and W. Kohn. *Phys. Rev.*, 136:B864–871, 1964.

[38] K. S. Thygesen I. S. Kristensen, M. Paulsson and K. W. Jacobsen. *Phys. Rev. B*, 79:235411, 2009.

[39] Antti-Pekka Jauho, Ned S. Wingreen, and Yigal Meir. *Phys. Rev. B*, 50:5528, 1994.

[40] J. Jiang, M. Kula, W. Lu, and Y. Luo. *Nano Lett.*, 5:1551, 2005.

[41] L. Jiao, L. Zhang, L. Ding, J. Liu, and H. G. Dai. *Nano Res.*, 3:387, 2010.

[42] L. Jiao, L. Zhang, X. Wang, G. Diankov, and H. J. Dai. *Nature (London)*, 458:877, 2009.

[43] C. Jin, H. Lan, L. Peng, K. Suenaga, and S. Iijima. *Phys. Rev. Lett.*, 102:205501, 2009.

[44] L. P. Kadanoff and G. Baym. *Quantum Statistical Mechanics.* Benjamin, New York, 1962.

[45] S.-H. Ke, H. U. Baranger, and W. Yang. *Phys. Rev. Lett.*, 99:146802, 2007.

[46] L. V. Keldysh. *Zh. Eksp. Teor. Fiz.*, 47:1515, 1964.

[47] S. Kim and N. Marzari. in preparation.

[48] Y. O. Klymenko. *Eur. Phys. J. B*, 77:433, 2010.

[49] J. Koch, M. E. Raikh, and F. von Oppen. *Phys. Rev. Lett.*, 96:056803, 2006.

[50] J. Koch and F. von Oppen. *Phys. Rev. Lett.*, 94:206804, 2005.

[51] J. Koch, F. von Oppen, and A. V. Andreev. *Phys. Rev. B*, 74:205438, 2006.

[52] W. Kohn and L. J. Sham. *Phys. Rev.*, 140:A1133–1138, 1965.

[53] D. V. Kosynkin, A. L. Higginbotham, A. Sinitskii, J. R. Lomeda, A. Dimiev, B. K. Price, and J. M. Tour. *Nature (London)*, 458:872, 2009.

[54] J. G. Kushmerick, J. Lazorcik, C. H. Patterson, and R. Shashidhar. *Nano. Lett.*, 4:639–642, 2004.

[55] D. H. Lee and J. D. Joannopoulos. *Phys. Rev. B*, 23, 1981.

[56] Y.-S. Lee and N. Marzari. *Phys. Rev. Lett.*, 97:116801, 2006.

[57] Y.-S. Lee, M. B. Nardelli, and N. Marzari. *Phys. Rev. Lett.*, 95:076804, 2005.

[58] X. Li, X. Wang, L. Zhang, S. Lee, and H. J. Dai. *Science*, 319:1229, 2008.

[59] M. R. Sorensen M. Brandbyge and K. W. Jacobsen. *Phys. Rev. B*, 56:14956, 1997.

[60] T. N. Todorov M. J. Montgomery, J. Hoekstra and A. P. Sutton. *J. Phys: Condens. Matter*, 15:731, 2003.

[61] K. L. Ma, X. H. Yan, Y. D. Guo, and Y. Xiao. *Eur. Phys. J. B*, 83:487, 2011.

[62] P. C. Martin and J. Schwinger. *Phys. Rev.*, 115:1342, 1959.

[63] T. B. Martins, A. Fazzio, and A. J. R. da Silva. *Phys. Rev. B*, 79:115413, 2009.

[64] N. Marzari and D. Vanderbilt. *Phys. Rev. B*, 56:12847, 1997.

[65] Yigal Meir and Ned S. Wingreen. *Phys. Rev. Lett*, 68:2512, 1992.

[66] M. J. Montgomery and T. N. Todorov. *J. Phys: Condens. Matter*, 15:8781, 2003.

[67] S. Nakanishi and M. Tsukada. *Phys. Rev. Lett.*, 87:126801, 2001.

[68] A. H. Castro Neto, F. Guinea, N. M. R. Peres, K. S. Novoselov, and A. K. Geim. *Rev. Mod. Phys.*, 81:109–162, 2009.

[69] K. S. Novoselov, A. K. Geim, S. V. Morozov, D. Jiang, M. I. Katsnelson, I. V. Grigorieva, S. V. Dubonos, and A. A. Firsov. *Nature (London)*, 438:197, 2005.

[70] K. S. Novoselov, A. K. Geim, S. V. Morozov, D. Jiang, Y. Zhang, S. V. Dubonos, I. V. Grigorieva, and A. A. Firsov. *Science*, 306:666, 2004.

[71] M. Paulsson and M. Brandbyge. *Phys. Rev. B*, 76:115117, 2007.

[72] M. Paulsson, T. Frederiksen, and M. Bradbyge. *Phys. Rev. B*, 72:201101(R), 2005.

[73] M. C. Payne, M. P. Teter, D. C. Allan, T. A. Arias, and J. D. Joannopoulos. *Rev. Mod. Phys.*, 64:1045, 1992.

[74] J. P. Perdew, K. Burke, and M. Ernzerhof. *Phys. Rev. Lett.*, 77:3865, 1996.

[75] J. P. Perdew and A. Zunger. *Phys. Rev. B*, 23:5048, 1981.

[76] M. E. Peskin and D. V. Schroeder. *An Introduction To Quantum Field Theory.* Westview Press, 1995.

[77] J. Rammer. *Quantum Field Theory of Non-equilibrium States.* Cambridge University Press, New York, 2007.

[78] J. Rammer and H. Smith. *Rev. Mod. Phys.*, 58:323, 1986.

[79] J. Rammer and H. Smith. *Rev. Mod. Phys.*, 58:323, 1986.

[80] M. A. Reed, C. Zhou, C. J. Muller, T. P. Burgin, and J. M. Tour. *Science*, 278:252, 1997.

[81] G. Romano, A. Gagliardi, A. Pecchia, and A. Di Carlo. *Phys. Rev. B*, 81:115438, 2010.

[82] D. A. Ryndyk, M. Hartung, and G. Cuniberti. *Phys. Rev. B*, 73:045420, 2006.

[83] M. P. L. Sancho, J. M. L. Sancho, and J. Rubio. *J. Phys. F: Met. Phys.*, 14:1205, 1984.

[84] M. P. L. Sancho, J. M. L. Sancho, and J. Rubio. *J. Phys. F: Met. Phys.*, 15:851, 1985.

[85] M. P. L. Sancho, J. M. L. Sancho, and J. Rubio. *J. Phys. C*, 18:1803, 1985.

[86] H. Santos, L. Chico, and L. Brey. *Phys. Rev. Lett.*, 103:086801, 2009.

[87] R. H. M. Smit, Y. Noat, C. Untiedt, N. D. Lang, M. C. van Hemert, and J. M. van Ruitenbeek. *Nature*, 419:906, 2002.

[88] G. C. Solomon, C. Herrmann, T. Hansen, V. Mujica, and M. A. Ratner. *Nat. Chem.*, 2:223, 2010.

[89] H. Song, Y. Kim, Y. H. Jang, H. Jeong, M. A. Reed, and T. Lee. *Nature*, 462:1039, 2009.

[90] I. Souza, N. Marzari, and D. Vanderbilt. *Phys. Rev. B*, 65:035109, 2002.

[91] B. C. Stipe, M. A. Rezaei, and W. Ho. *Science*, 280:1732, 1998.

[92] L. Tapasztó, G. Dobrik, P. Lambin, and L. P. Biró. *Nat. Nanotechnol.*, 3:2083, 2008.

[93] J. Taylor, H. Guo, and J. Wang. *Phys. Rev. B*, 63:245407, 2001.

[94] M. A. Topinka, B. J. LeRoy, S. E. J. Shaw, R. M. Westervelt, R. Fleischmann, E. J. Heller, K. D. Maranowski, and A. C. Gossard. *Nature (London)*, 410:183, 2001.

[95] N. Troullier and J. L. Martins. *Phys. Rev. B*, 43:1993, 1991.

[96] D. Vanderbilt. *Phys. Rev. B*, 41:7892, 1990.

[97] J. K. Viljas, J. C. Cuevas, F. Pauly, and M. Hafner. *Phys. Rev. B*, 72:245415, 2005.

[98] B. Wang and J. Wang. *Phys. Rev. B*, 81:045425, 2010.

[99] W. Wang, T. Lee, I. Kretzschmar, and M. A. Reed. *Nano. Lett.*, 4:643–646, 2004.

[100] G. H. Wannier. *Phys. Rev.*, 52:191, 1937.

[101] Y. Yoon and S. Salahuddin. *Appl. Phys. Lett.*, 97:033102, 2010.

[102] Yuanbo Zhang, Yan-Wen Tan, Horst L. Stormer, and Philip Kim. *Nature (London)*, 438:201, 2005.